الجمهورية الجزائرية الديمقراطية الشعبية
République Algérienne Démocratique et Populaire
وزارة التعليم العالي والبحث العلمي
Ministère de l'enseignement supérieur et la recherche scientifique

Université 20 Août 1955
- Skikda -
Faculté de Technologie
Département de Génie Electrique
Réf : D012126006D

جامعة 20 أوت 1955
- سكيكدة -
كلية التكنولوجيا
قسم الهندسة الكهربائية

THÈSE DE DOCTORAT

En vue de l'obtention du diplôme de doctorat de 3ième cycle (D-LMD)

Option : Electrotechnique

Specialité: Réseaux Electriques

Laboratoire LES

Stratégie de commande d'un système d'énergie renouvelable connecté au réseau

Présentée par

Noussaiba MENNAI

Soutenue le 04/02/2026 devant le jury composé de :

Comité du jury:

Nom et Prénom :	Grade	Établissement d'affiliation	Désignation
Pr. Boukadoum Ahcene	Professeur	Université 20 Août 1955 -Skikda	Président
Pr. Medoued Ammar	Professeur	Université 20 Août 1955 -Skikda	Rapporteur
Pr. Soufi Youcef	Professeur	Université Larbi Tebessi -Tébessa	Co-Rapporteur
Pr. Lalalou Rachid	Professeur	Université 20 Août 1955 -Skikda	Examinateur
Pr. Mehasni Rabia	Professeur	Université Frères Mentouri -Constantine 1	Examinateur
Pr. Labar Hocine	Professeur	Université Badji Mokhtar -Annaba	Examinateur

Université de Skikda, FT – 2026

الجمهورية الجزائرية الديمقراطية الشعبية
People's Democratic Republic of Algeria
وزارة التعليم العالي والبحث العلمي
Ministry of Higher Education and Scientific Research

University of 20 August 1955

- Skikda -

Faculty of Technology

Electrical Engineering Department

Ref : D012126006D

جامعة 20 أوت 1955
- سكيكدة -
كلية التكنولوجيا
قسم الهندسة الكهربائية

DOCTORAL THESIS

With a view to obtaining the 3rd cycle doctoral degree (D- LMD)

Option : Electrical Engineering

Speciality: Electrical Networks

LES Laboratory

Control Strategy of a Grid-Connected Renewable Energy System

Presented by

Noussaiba MENNAI

Defended on 04/02/2026 before the jury composed of:

Committee of Jury:

First and Last Name :	Grade	Institution of Affiliation	Designation
Pr. Boukadoum Ahcene	Professor	University of 20 August 1955 -Skikda	President
Pr. Medoued Ammar	Professor	University of 20 August 1955 -Skikda	Supervisor
Pr. Soufi Youcef	Professor	Larbi Tebessi University -Tebessa	Co-Supervisor
Pr. Lalalou Rachid	Professor	University of 20 August 1955 -Skikda	Examiner
Pr. Mehasni Rabia	Professor	Frères Mentouri University -Constantine 1	Examiner
Pr. Labar Hocine	Professor	Badji Mokhtar University -Annaba	Examiner

Skikda University, FT – 2026

Acknowledgments

First and foremost, all deepest thanks are due to the Almighty ALLAH, the merciful and compassionate for uncountable gifts given to me. I thank God for helping me complete this work and reach this stage of life and for giving me the patience to get through all the hardships, obstacles, and challenges for this year.

I would like to express my heartfelt thanks to my supervisor, Pr. Medoued Ammar, and my co-supervisor, Pr. Soufi Youcef from Larbi Tebessi University – Tebessa, for their invaluable guidance, continuous encouragement, and constructive advice throughout the course of this thesis. Their patience, expertise, and constant support have been essential to the completion of this work. I would also like to warmly acknowledge the responsible individuals at the Algerian National Company for Electricity and Gas (SONELGAZ) and the OKP PV Plant director, Mr. Dib Ilyas, for providing us with the solar and electrical data used in this work. Their collaboration and assistance were greatly appreciated and important for the progress of this research.

I would also like to thank the president of the jury, Pr. Boukadoum Ahcene from the University of Skikda, for honoring me with his presence and valuable remarks. My sincere thanks also go to the examiners: Pr. Lalalou Rachid from the University of Skikda, Pr. Mehasni Rabia from the University of Constantine 1, and Pr. Labar Hocine from the University of Annaba, for their time, efforts, and insightful comments that have enriched this work.

My deepest gratitude goes to my mother for her patience and endless support. I thank her for constant love and prayers for me. I know I can never come close to returning her favor upon me. I thank all my sisters as well: Hadia, Amina, and Asma for their continuous encouragement throughout my life.

A very special mention goes to my two lovely nieces, Yousr and Janna, whose smiles and innocent presence have been a source of pure joy and comfort to me during this journey. Even at just 2 years old and 6 months, you have filled my heart with happiness and reminded me of the simple beauty in life. For that, I am deeply thankful.

Dedications

To the cherished memory of my beloved grandfather, “El Hadj Mohamed Zehouani”, and my dear little sister,” Youssra”.

May this work be a humble tribute to your everlasting memory.

الملخص

يواجه قطاع الطاقة العالمي تحديات كبيرة بسبب الطلب المتزايد على الكهرباء والتأثيرات البيئية للوقود الأحفوري، مما يدفع إلى اعتماد مصادر الطاقة المتجددة مثل الأنظمة الكهروضوئية (PV) المتصلة بالشبكة. ومع ذلك، تُدخل هذه الأنظمة تعقيدات مثل التشوه التوافقي وعدم الاستقرار الناتج عن الإلكترونيات القوية، خاصة في ظل الظروف البيئية المتغيرة. لذلك، غالبًا ما يكون إجراء الاختبارات العملية على هذه الأنظمة صعبًا أو مستحيلًا بسبب الطبيعة التدميرية للعديد من السيناريوهات. ونتيجة لذلك، تعتمد الدراسات الحالية غالبًا على نماذج مبسطة أو عامة تهمل ليس فقط النمذجة التفصيلية للنظام، بل أيضًا التحقق من استراتيجيات التحكم في ظل ظروف العالم الحقيقي، بما في ذلك التحقق من الامتثال لمعايير الشبكة مثل IEEE 929-2000 و IEEE 519-1992 و EN 50160. تعالج هذه الأطروحة هذه الفجوات من خلال تطوير نموذج شامل واستراتيجية تحكم لنظام كهروضوئي متصل بالشبكة بقدرة 1 ميغاواط، استنادًا إلى بيانات حقيقية من محطة أويد الكبريت الكهروضوئية بقدرة 15 ميغاواط في سوق أهراس، الجزائر. يعتمد النموذج المقترح على طوبولوجيا من مرحلتين تشمل مصفوفة كهروضوئية— يتم تمثيلها باستخدام نموذج الدايود الواحد مع تقدير تكراري للمعاملات—ومحول DC-DC معزز مع تتبع نقطة القدرة القصوى (MPPT) القائم على التوصيل المتزايد، وعاكس مصدر جهد ثلاثي الطور (VSI) يستخدم تعديل عرض النبضة الجيبية (SPWM). يتم تسهيل التكامل مع الشبكة من خلال مرشح LCL مخمد بشكل سلبي وحلقة قفل طور بإطار مرجعي متزامن (SRF-PLL)، بينما يتم ضمان استقرار النظام من خلال وحدات تحكم PI مزدوجة الحلقات تم تهيئتها باستخدام طريقة التماثل الأمثل. تم اشتقاق معاملات خط النقل تحليليًا لتكرار ظروف المحطة. تم اختبار النموذج، الذي تم تنفيذه في MATLAB/Simulink، تحت ظروف الاختبار القياسية (STC)، والتغيرات المفاجئة في الإشعاع، وسيناريوهات التشغيل الحقيقية. تُظهر النتائج أداءً قويًا، حيث تحقق كفاءة تحويل إجمالية تتجاوز 96%، وعامل قدرة موحد، ومستويات تشوه توافقي ($THD_i < 1.5\%$; $TDD < 1.2\%$) ضمن الحدود الموصوفة. أكدت التحقق من البيانات المقاسة من محطة تشغيلية في 2 مايو 2024 دقة النموذج، حيث بلغت الكفاءة المحاكاة 97.01%، وهي تتطابق بشكل وثيق مع القيمة التجريبية البالغة 95.89%. تُقدم هذه الدراسة أول نموذج مدقق على نطاق واسع في الجزائر، ولا يوفر فقط تمثيلًا دقيقًا للمحطة الفعلية، بل يُعد أيضًا أداة قوية للتصميم والتحليل لأبحاث الأنظمة الكهروضوئية واسعة النطاق في المستقبل.

الكلمات المفتاحية: الطاقة المتجددة، الكهروضوئية المتصلة بالشبكة، استراتيجية التحكم، عاكس مصدر جهد ثنائي المستوى، التشوه التوافقي، تتبع نقطة القدرة القصوى، قفل الطور

Abstract

The global energy sector faces significant challenges due to increasing electricity demand and the environmental impacts of fossil fuels, driving the adoption of renewable sources such as solar photovoltaic (PV) systems. Grid-connected PV systems, however, introduce complexities like harmonic distortion and instability from power electronics, particularly under varying environmental conditions. Therefore, conducting practical testing on these systems can be difficult and often impossible due to the destructive nature of many scenarios. Consequently, existing studies often rely on simplified or generic models that overlook not only detailed system modeling but also the validation of control strategies under real-world conditions, including verification of compliance with grid standards such as IEEE 929-2000, IEEE 519-1992, and EN 50160. This thesis addresses these gaps by developing a comprehensive model and control strategy for a 1 MW grid-connected PV system, based on real data from the 15 MW_p Oued El Kebrit PV plant in Souk Ahras, Algeria. The proposed model adopts a two-stage topology comprising a photovoltaic (PV) array—represented using the single-diode model with iterative parameter estimation—a DC–DC boost converter with incremental conductance-based maximum power point tracking (MPPT), and a three-phase voltage source inverter (VSI) employing sinusoidal pulse width modulation (SPWM). Grid integration is facilitated through a passive-damped LCL filter and a synchronous reference frame phase-locked loop (SRF-PLL), while system stability is ensured via dual-loop PI controllers tuned using the symmetrical optimum method. Transmission line parameters are analytically derived to replicate plant conditions. The model, implemented in MATLAB/Simulink, was tested under standard test conditions (STC), sudden irradiance variations, and real operating scenarios. The results demonstrate robust performance, achieving an overall conversion efficiency exceeding 96%, unity power factor, and harmonic distortion levels ($THD_i < 1.5\%$, $TDD < 1.2\%$) well within prescribed limits. Validation against measured data from an operational plant on May 2, 2024, confirmed the model's accuracy, with simulated efficiency of 97.01% closely matching the experimental value of 95.89%. This study presents the first validated utility-scale PV model for Algeria and not only provides an accurate representation of the actual plant but also serves as a powerful design and analysis tool for future research in utility-scale PV systems.

Keywords : Renewable Energy, Grid-Connected PV, Control Strategy, 2L-VSI, Harmonic Distortion, MPPT, PLL

Résumé

Le secteur énergétique mondial est confronté à des défis majeurs en raison de la demande croissante en électricité et des impacts environnementaux des combustibles fossiles, ce qui accélère l'adoption de sources renouvelables telles que les systèmes photovoltaïques (PV) connectés au réseau. Cependant, ces systèmes introduisent des complexités telles que la distorsion harmonique et l'instabilité des électroniques de puissance, en particulier dans des conditions environnementales variables. Ainsi, les tests pratiques sur ces systèmes sont souvent difficiles, voire impossibles, en raison de la nature destructrice de nombreux scénarios. Par conséquent, les études existantes reposent fréquemment sur des modèles simplifiés ou génériques qui négligent non seulement une modélisation détaillée du système, mais aussi la validation des stratégies de commande dans des conditions réelles, y compris la vérification de la conformité aux normes de réseau telles que IEEE 929-2000, IEEE 519-1992 et EN 50160. Cette thèse comble ces lacunes en développant un modèle complet et une stratégie de commande pour un système PV connecté au réseau de 1 MW, basé sur des données réelles provenant de la centrale PV de 15 MWc d'Oued El Kebrit à Souk Ahras, Algérie. Le modèle proposé adopte une topologie à deux étages comprenant un réseau photovoltaïque — représenté par le modèle à diode unique avec estimation itérative des paramètres —, un convertisseur DC-DC de type boost avec suivi du point de puissance maximale (MPPT) basé sur la conductance incrémentale, et un onduleur triphasé à source de tension (VSI) utilisant la modulation de largeur d'impulsion sinusoïdale (SPWM). L'intégration au réseau est facilitée par un filtre LCL à amortissement passif et une boucle à verrouillage de phase en référentiel synchrone (SRF-PLL), tandis que la stabilité du système est assurée par des contrôleurs PI à double boucle réglés selon la méthode de l'optimum symétrique. Les paramètres de la ligne de transmission sont dérivés analytiquement pour reproduire les conditions de la centrale. Le modèle, implémenté dans MATLAB/Simulink, a été testé dans des conditions d'essai standard (STC), sous des variations soudaines d'irradiance et dans des scénarios d'exploitation réels. Les résultats démontrent des performances robustes, avec un rendement global de conversion dépassant 96 %, un facteur de puissance unitaire et des niveaux de distorsion harmonique (THD_i < 1,5 %, TDD < 1,2 %) largement conformes aux limites prescrites. La validation par rapport aux données mesurées dans une centrale opérationnelle le 2 mai 2024 a confirmé la précision du modèle, avec un rendement simulé de 97,01 % correspondant étroitement à la valeur expérimentale de 95,89 %. Cette étude présente le premier modèle validé de système PV à grande échelle pour l'Algérie et offre non seulement une représentation précise de la centrale réelle, mais également un outil puissant de conception et d'analyse pour les recherches futures sur les systèmes PV à grande échelle.

Mots-clés: Énergie renouvelable, PV connecté au réseau, Stratégie de commande, VSI à deux niveaux, Distorsion harmonique, MPPT, PLL

Scientific Contributions

Journal Publications

N. Mennai, A. Medoued, and Y. Soufi, 'A detailed model and control strategy for a three-phase grid-connected PV system: a case study of Oued El Kebrit 15 MW_p PV plant', *Electrical Engineering*, vol. 107, no. 3, pp. 3197–3216, 2025. https://doi.org/10.1007/s00202-024-02657-5

N. Mennai, A. Medoued, and Y. Soufi, 'Comparative analysis of dynamic and steady State performances of Hill climbing and incremental conductance MPPT controllers for PV systems', *Journal of Renewable Energy and Environment*, vol. 11, no. 3, pp. 35–41, 2024. https://doi.org/10.30501/jree.2024.432251.1788

International Conferences

N. Mennai, A. Medoued, Y. Soufi, and A. Faleh, "Intelligent Control for Enhanced Phase-Locked Loop Performance in Grid-Connected Inverters," presented at *the 6th International Hybrid Conference On Informatics And Applied Mathematics, CEUR Workshop Proceedings*, 2023, pp. 136–142.

N. Mennai, Y. Soufi, A. Medoued, and A. Faleh, 'Grid synchronization techniques analysis of dg systems under grid fault conditions', in *2022 19th International Multi-Conference on Systems, Signals & Devices (SSD)*, 2022, pp. 917–922. https://doi.org/10.1109/SSD54932.2022.9955866

National Conferences

N. Mennai, A. Medoued, Y. Soufi, A. Kechida, K. Chebli, and K. Fettah, "Systematic Design of a Passive Damped LCL Filter for Grid-Tied Voltage Source Inverters," presented at *the 1st National Conference on Mechatronic Engineering (NCME'2025)*, 2025.

N. Mennai, A. Medoued, and Y. Soufi, "Identification of PV Module Parameters Through an Iterative Method," presented at *the First National Conference on Advances in Telecommunications, Electronics and Computer Engineering (ATECE'24)*, 2024.

Table of Contents

Chapter IV : **Results, Analysis, and Discussion**

List of Figures

Chapter I

Chapter II

Chapter III

Chapter IV

List of tables

List of Abbreviations

GHG	Greenhouse gas
MPPT	Maximum Power Point Tracking
THD	Total Harmonic Distortion
TDD	Total Demand Distortion
2L-VSI	Two-level Voltage Source Inverter
NRM	Newton-Raphson method
PWM	Pulse Width Modulation
STC	Standard Test Conditions
MPP	Maximum Power Point
SPWM	Sinusoidal Pulse Width Modulation
PLL	Phase Locked Loop
IEEE	Institute of Electrical and Electronics Engineers
EN	European standard
EIA	Energy Information Administration
IEA	International Energy Agency
SPWM	Sinusoidal Pulse Width Modulation
RMS	Root Mean Square
PCC	Point of Common Coupling
SRF	Synchronous Reference Frame
GSCF	Grid-Side Current Feedback
PI	Proportional Integral
AAAC	All Aluminum Alloy Conductors

General Introduction

General Introduction

The global energy sector is currently facing unprecedented challenges, primarily due to the rising demand for electricity driven by both population growth and increasing per-capita consumption. According to recent projections, global electricity needs are expected to grow by an average of 3.3% in 2025 and 3.7% in 2026 [1]. However, the traditional reliance on fossil fuels—such as coal, oil, and natural gas—has led to considerable environmental consequences. In particular, the sector is responsible for significant greenhouse gas (GHG) emissions that exacerbate climate change. For instance, atmospheric CO_2 concentrations have surpassed 426 ppm in 2025, with power generation alone accounting for more than 40% of fossil fuel-related emissions [2, 3]. In response to these challenges, renewable energy sources have gained increasing prominence as sustainable alternatives. Among these, solar photovoltaic (PV) systems have emerged as a key solution, owing to their low maintenance requirements, silent operation, and absence of harmful emissions [4, 5]. PV technology operates by converting solar radiation into electrical energy through semiconductor materials, and its deployment has been expanding rapidly in both distributed generation and microgrid applications.

Grid-connected PV systems, in particular, often employ a double-stage architecture. This typically involves a DC-DC boost converter to regulate voltage and implement maximum power point tracking (MPPT), followed by a DC-AC inverter to achieve grid synchronization through pulse width modulation (PWM) techniques [6]. Nevertheless, such configurations introduce new challenges for grid integration. Harmonic distortions from power electronic devices and power fluctuations caused by variable irradiance or temperature can compromise grid stability [7]. Consequently, strict compliance with international standards—such as IEEE 929-2000, IEEE 519-1992, and EN 50160—is essential to ensure that PV-generated electricity maintains acceptable power quality.

Within this global context, Algeria presents a particularly promising case for solar PV adoption. Owing to its exceptional solar potential, especially in the Sahara region, the country has identified renewables as a strategic pathway to diversify its energy mix, reduce reliance on fossil fuels, and meet growing domestic electricity demand while sustaining gas exports [8, 9]. National targets aim to achieve 15,000 MW of renewable capacity by 2035, with solar PV forming the backbone of this strategy [10, 11]. A notable example is the 15 MW_p Oued El Kebrit (OKP) PV plant in Souk Ahras, which serves as a representative case study of large-scale solar deployment in Algeria. Despite these developments, a review of the existing literature on grid-

connected PV systems reveals several persistent gaps. Many prior studies rely on simplified or generic models that are not validated by real operating data. Others lack complete parameter identification or only partially address compliance with grid codes [12-14]. To date, no comprehensive study has developed and validated a large-scale Algerian PV system model based on field measurements.

To bridge these gaps, this thesis develops a detailed model and control strategy for a 1 MW grid-connected PV system using the OKP plant as a case study. The specific objectives are fivefold: (1) to model the PV array using iterative parameter estimation; (2) to evaluate the performance of MPPT algorithms under dynamic conditions; (3) to design inverter components, including the LCL filter and SRF-PLL; (4) to assess overall system performance in terms of efficiency and power quality; and (5) to validate the proposed model against real operating data while ensuring compliance with international standards.

The main contributions of this thesis, which are presented in Chapter 1, include the development of a realistic model and control strategy that achieves over 96% conversion efficiency with low harmonic distortion. This work represents the first validated utility-scale PV system model for Algeria, offering both technical insights and practical relevance. The remainder of the thesis is structured as follows: Chapter II focuses on DC-side modeling, Chapter III addresses AC-side components, Chapter IV evaluates the integrated system, and the concluding chapter summarizes the key findings while highlighting directions for future research.

Chapter I

Introduction and Literature Review

1.1 Introduction

This chapter provides an overview of solar photovoltaic (PV) systems within the context of the global energy transition. It begins by discussing the growing demand for electricity, the environmental impacts of fossil fuels, and the increasing role of renewable energy, particularly solar power. The chapter then highlights Algeria's renewable energy strategy and its exceptional solar potential, with a focus on the Oued El Kebrit PV plant as a case study. Fundamentals of solar energy conversion, PV technologies, and system classifications are reviewed, followed by the control requirements of grid-connected PV systems. Finally, a literature review identifies the research gaps that motivate this study and frames the contributions of the thesis.

1.2 Global renewable energy transition and role of PV

As global electricity demand continues to accelerate with population growth and increasing per-capita consumption as seen in Fig. 1., new power generation sources are essential to satisfy that rise. This growth is projected to be significant, with global demand forecast to increase by an average of 3.3% in 2025 and by 3.7% in 2026 [1].

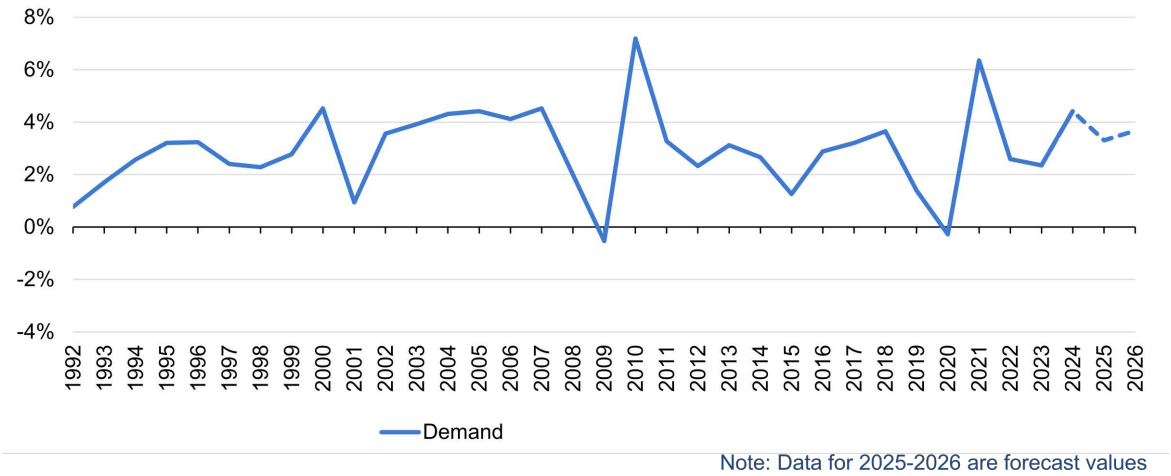

Figure 1.1 Annual global growth rate of electricity demand, 1992–2026.

To cover that power demand, power plants rely on multiple fossil fuels, namely oil, coal, and natural gas [15]. Among these fuels, coal is the largest used one due to its low price and abundance across various regions of the world. The main drawback associated with fossil fuels is their high carbon dioxide gas emissions and other gases such as Sulphur, nitrogen, and carbon oxides, which present a threat to the overall ecosystem and environment. Not only the emissions that give rise to concerns, but also their effect on climate change and global warming, which are

primarily brought on by CO_2 other gases known as greenhouse gases (GHG). These gases traps solar heat from escaping into space, preventing a rise in global temperatures over time [16].

By studying ice samples collected from extremely deep Antarctic regions, researchers examined the changes of CO_2 concentration in the atmosphere. The JRC Science for Policy Report on GHG revealed that in 2024, nearly 78% of atmospheric CO_2 is due to the combustion of fossil fuels with electric power generation accounting for over 40% of this share (see Fig. 1.2(a)) [3, 17].

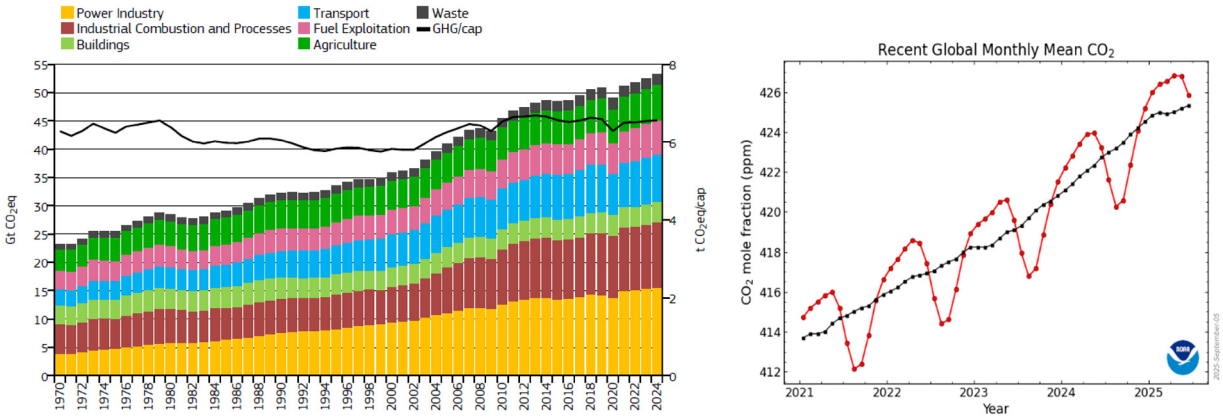

(a) (b)

Figure 1.2 Global greenhouse gas trends: (a) GHG emissions by sector and per capita1970–2024, (b) Monthly average atmospheric CO_2 concentrations, 2021–2025.

The continuous rise in atmospheric CO_2 levels further emphasizes the urgent need to transition away from fossil fuels. As illustrated in Fig. 1.2(b), global monthly mean CO_2 concentrations have steadily increased from 2021 to 2025, reaching values above 426 ppm [2]. This trend strongly highlights why international efforts such as the Kyoto Protocol and subsequent climate agreements aim to mitigate greenhouse gas emissions through greater adoption of renewable and low-carbon energy technologies. On the other hand, it is said that the energy source is renewable if its consumption never influences its quantity, nor limit its use in the future. Nevertheless, this is not the case for fossil fuels, which exist with limited quantity and likely to run out of soon if this trend continues.

In this context, according to the U.S. Energy Information Administration's International Energy Outlook 2023 (IEO2023), global electricity generation is projected to increase by 30 % to 76 % in 2050 relative to 2022, depending on the case/scenario [18]. The primary driver of this growth will be zero-carbon technologies, predominantly with solar, wind and nuclear power, which will account for the vast majority (between 54% and 67%) of new capacity. While the overall capacity will grow, the share of coal, natural gas, and petroleum liquids in the global capacity mix is expected to decrease between 27 % and 38 % [18].

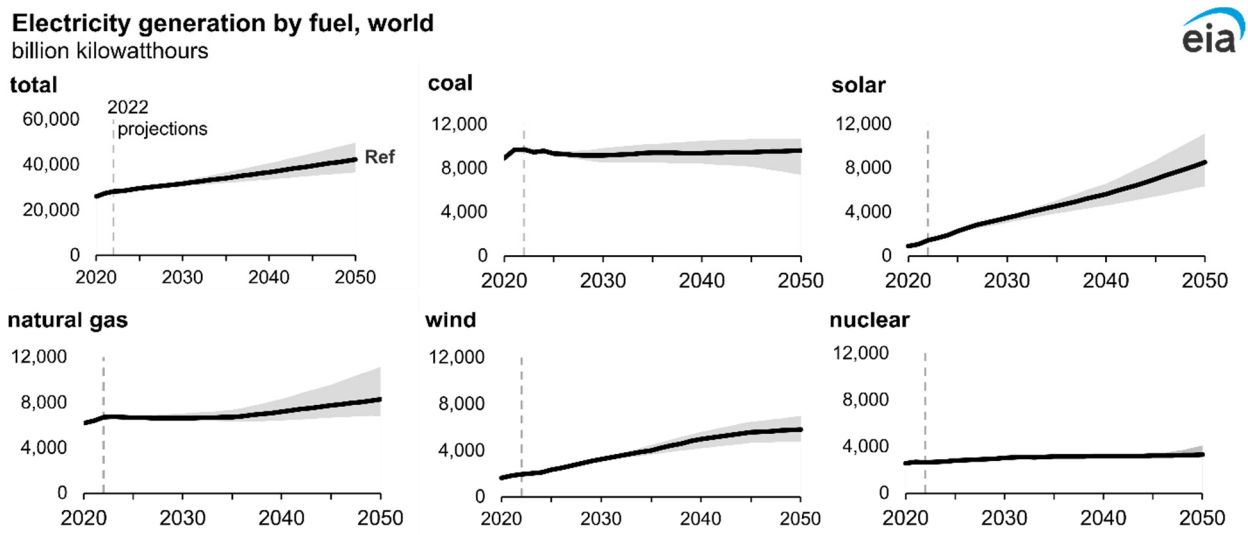

Figure 1.3 Global electricity generation by fuel type, projections from 2022 to 2050

As of 2025, solar power is no longer more expensive than fossil fuels for new generation: the levelized cost of electricity (LCOE) for utility-scale solar PV has fallen sharply and is often competitive with or cheaper than coal and natural gas. The U.S. EIA and IEA project that by 2050, solar will provide a major share of global electricity due to continued cost declines, policy support, and rapid deployment, making it one of the dominant sources of new power generation [1, 18].

1.2.1 Renewable energy goals and policies in algeria

Algeria, endowed with the world's tenth-largest proven natural gas reserves, ranking seventh in gas exports, significant shale gas potential, and a position among the top twenty in oil reserves, is increasingly prioritizing renewable energy to diversify its mix and preserve gas for export. This shift is driven by rapidly rising domestic electricity demand, which grew by 5% in 2024 compared to 2023, and the government's strategy to expand renewable generation in order to free up natural gas for international markets, a vital source of national revenue [8]. Conversely, Algeria's geographical position places it in a strategically advantageous location to play a major role in advancing renewable energy (RE) technologies across North Africa. This position not only allows the country to cover its domestic energy demand but also to potentially export such resources to European markets. The Sahara region, located in southern Algeria, extends over 2,048,297 km², accounting for nearly 86% of the nation's total land area [19]. Based on satellite assessments, the German Aerospace Center (Deutsches Zentrum für Luft- und Raumfahrt e.V, DLR) identified Algeria as having the highest solar energy potential in the Mediterranean region. Their evaluation estimated an annual output of 169,000 TWh from solar thermal (TS) technology

and about 13.9 TWh from photovoltaic (PV) systems. To put this into perspective, Algeria's solar capacity is comparable to ten large-scale natural gas fields such as those found at Hassi R'Mel [9]. Table 1.1 illustrates the regional variation in solar potential, measured by annual sunshine duration.

Regions	**Coastal regions**	**Highlands**	**Sahara**
Share of area (%)	4	10	86
Area (km^2)	95.27	238.174	2.048.297
Average daily sunshine duration (h)	7.26	8.22	9.59
Average duration of sunshine (h/an)	2650	3000	3500
Average energy received ($kWh/m^2/an$)	1700	1900	2650
Daily solar energy density (kWh/m^2)	4.66	5.21	7.26

Table 1.1 Solar radiation levels in various algerian regions [20].

The Algerian Sahara is among the sunniest regions in the world, with an average of about 3,500 hours of sunshine per year, and daily sunshine often exceeding 10 to 12 hours during summer months, making it one of the most favorable areas globally for solar energy development [19].

As shown in Fig. 1.4, the annual global irradiation (Gh) received on a horizontal surface across Algeria is provided according to the Algerian Atlas GEE [16].

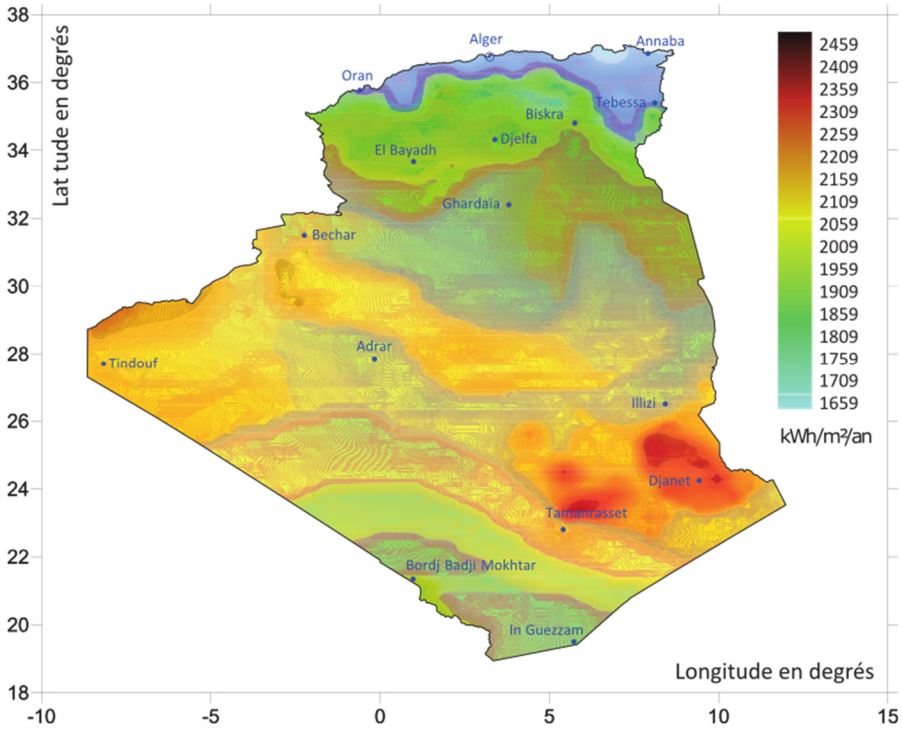

Figure 1.4 Annual global irradiation (Gh) on a horizontal surface in Algeria

To harness its solar potential, Algeria launched an ambitious renewable energy (RE) program adopted by the government on February 3, 2011 [10, 11]. The key targets were as follows:

- A strategy to produce 22,000 MW of electricity from renewable sources by 2030, with 93.5% expected to come from solar and wind, predominantly solar PV.
- In 2020, this target was revised to 15,000 MW, with the deadline extended to 2035.

As part of this national program, several solar PV plants have already been implemented, totaling 501 MW_p as illustrated in Fig. 1.5, while additional projects are in the pipeline. Recent actions further underline this commitment. In 2024, Algeria launched large-scale solar initiatives aiming to deliver 3,200 MW by 2026. This capacity is divided into 20 grid-connected solar plants providing 2,000 MW, five additional plants supplying 1,000 MW, and a stand-alone facility with 200 MW of battery-backed storage dedicated to the Gara Djebilet mining project in Tindouf. These projects mark a decisive shift from planning to concrete implementation, positioning Algeria as an emerging regional leader in solar power.

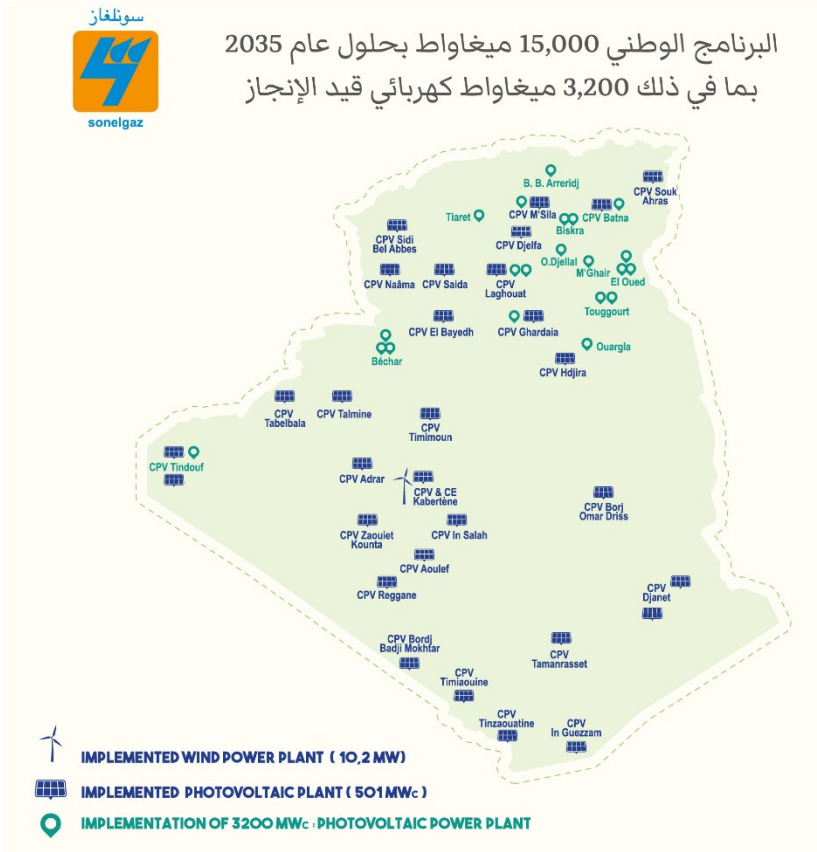

Figure 1.5 Algeria's RE national program: 15,000 MW by 2035, with 3,200 MW in progress.

1.2.2 Oued El Kebrit (OKP) PV plant, Souk Ahras

One of the PV power plants established in Algeria is situated in Oued El Kebrit (OKP), within the Souk Ahras Province, at approximately 35.9182° N, 7.8744° E in northeastern Algeria. The

site lies about 65 km south of Souk Ahras city, the provincial capital, and around 7–10 km north of El Aouinet in neighboring Tebessa Province. The plant, which is operated by Sharikat Kahraba wa Takat Moutajadida (SKTM)—a subsidiary of the Algerian national electricity and gas provider (SONELGAZ)—was commissioned on April 24, 2016, with a nominal capacity of 15 MW_p over an estimated area of 30 hectares. It is equipped with 60,048 YL250P-29b solar PV modules mounted on fixed structures [9], as shown in Fig. 1.6(a). The facility is divided into two loops: the first consists of eight subfields and the second of seven subfields, as illustrated in Fig. 1.6(b). Each subfield comprises 4,004 modules (91 arrays) with a capacity of 1.001 MW_p and is equipped with two 500 kW centralized inverters. Each inverter delivers an AC output voltage of 315 V, which is then stepped up by a transformer to 31.5 kV. The generated power is injected into the 30 kV busbar of the 220/90/30 kV substation in El Aouinet, Tébessa, via a 6.3 km Almelec transmission line with a cross-sectional area of 93.3 mm² [21], as shown in Fig. 1.7.

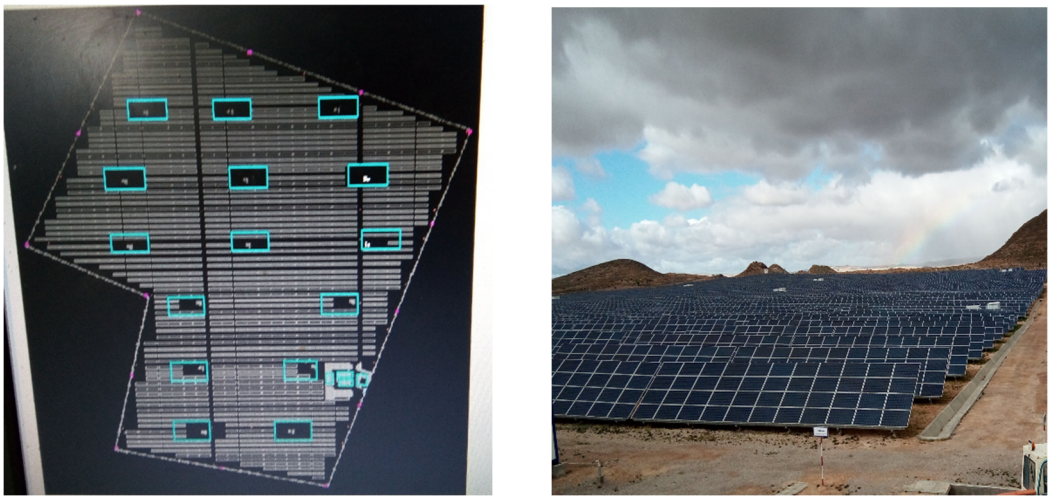

(a) (b)

Figure 1.6 (a) Oued El Kebrit PV Plant with 15 subfields and 15 inverters; (b) Fixed-structure PV module installation (photos by author).

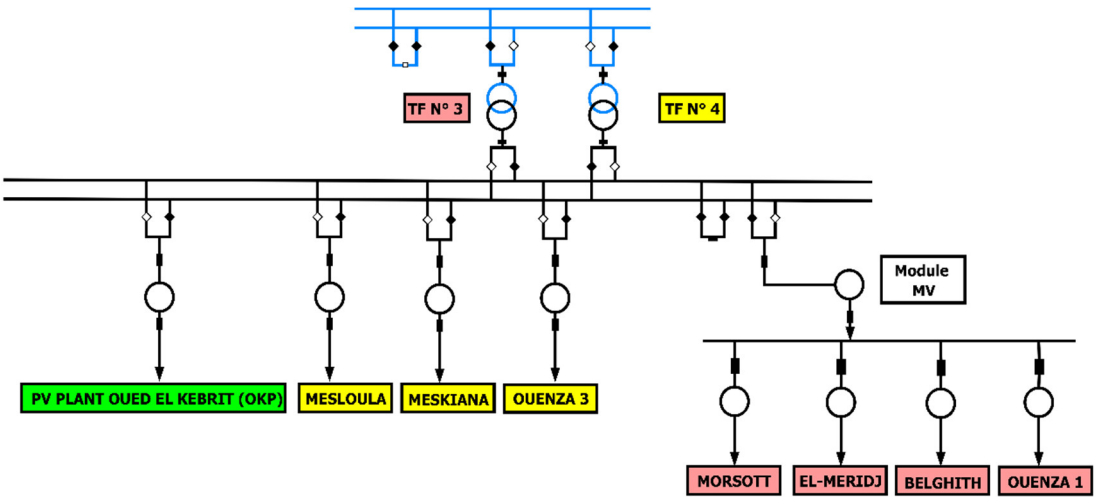

Figure 1.7 30 kV busbar layout of the El Aouinet substation.

The OKP plant is equipped with weather stations to measure the meteorological conditions in real-time. It also includes several instruments: an anemometer (wind speed), a rain gauge (rainfall amount), a hygrometer (air humidity), and a pyranometer (solar irradiance) as shown in Fig. 1.8.

Figure 1.8 Weather station at the 15 MW_p OKP PV plant, Souk Ahras.

1.3 Fundamentals of solar PV energy

Solar energy is the primary source of almost all energy on Earth, providing the heat and light necessary for life. The sun delivers an immense, renewable, and practically limitless supply of energy, with the annual solar radiation reaching Earth's surface estimated to be more than 8,000 times greater than global energy consumption. At peak sunlight, the average solar irradiance on the Earth's surface is about 1 kilowatt per square meter, spread across the spectrum from ultraviolet to infrared [22]. Two main technologies are used to capture this energy: solar thermal systems, which convert sunlight into heat using collectors, and solar photovoltaic (PV) systems, which convert sunlight directly into electricity using solar cells. In addition, concentrating solar power (CSP) technology generates electricity by concentrating sunlight to produce heat that drives turbines. Together, these technologies support three major applications: solar thermal for heating, solar PV for electricity generation, and CSP for large-scale electricity production [23].

To understand how this energy reaches the surface, it is important to consider the role of the atmosphere. Composed mainly of nitrogen (78%) and oxygen (21%), with smaller amounts of argon, CO_2, water vapor, and ozone, the atmosphere filters and scatters solar radiation [20]. The intensity of incoming sunlight depends on the air mass (AM), defined as $AM=1/\cos\theta_z$, where θ_z

is the sun's zenith angle. Standard testing for photovoltaic devices is based on AM1.5 conditions, corresponding to 1000 W/m² of global radiation at a cell temperature of 25 °C, as specified by the IEC-60904 standard [24].

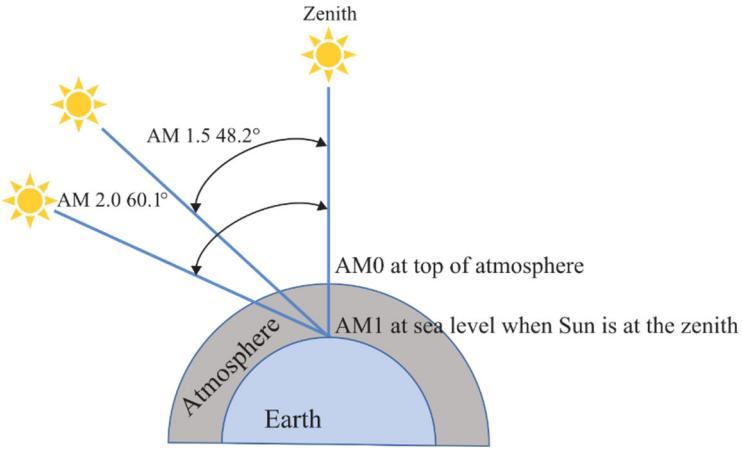

Figure 1.9 The air mass concept.

Solar radiation covers a broad spectrum: about 7% ultraviolet (<0.4 µm), 47% visible (0.4–0.7 µm), and 46% infrared (>0.7 µm) [24], as illustrated in Fig. 1.10. While the extraterrestrial irradiance averages 1361 W/m², atmospheric absorption and scattering reduce it to around 1000 W/m² at the surface. Local availability further varies with latitude, season, and weather conditions such as clouds and atmospheric particles [25]. On the ground, radiation is received as direct, diffuse, and reflected (albedo) components, measured respectively by pyrheliometers, pyranometers, and albedometers [20, 26].

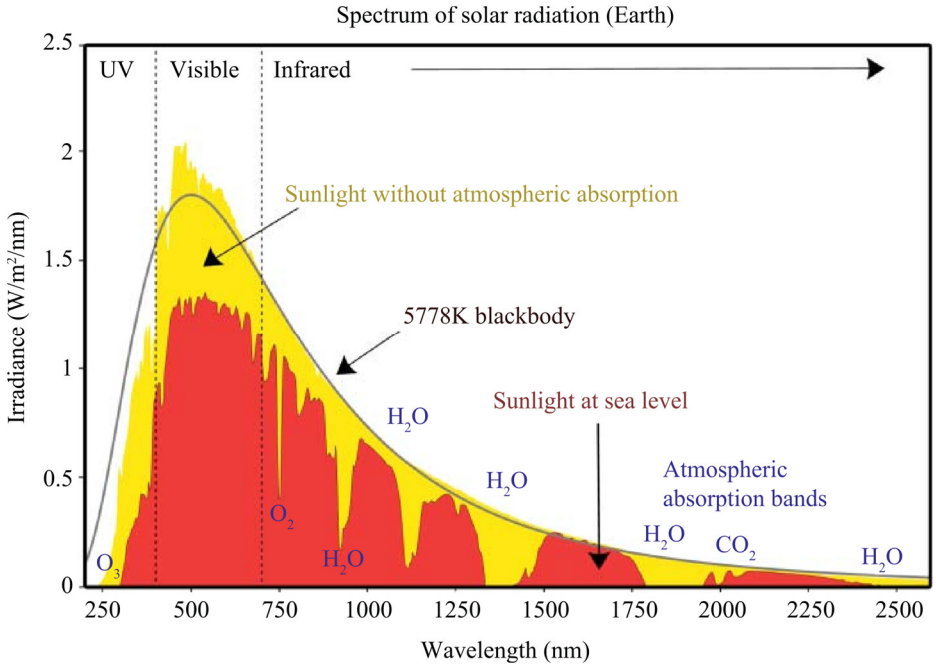

Figure 1.10 The solar spectrum above and on the Earth's surface.

1.3.1 PV technology basics

The fundamental unit of a photovoltaic (PV) system is the solar cell, which converts sunlight into direct current (DC) electricity through the photovoltaic effect first observed by Alexandre Edmond Becquerel in 1839 [27]. A PV cell is an electronic component made of semiconductor material, most commonly high-purity silicon, that absorbs photons and generates charge carriers. These cells are interconnected to form modules, which are then arranged into larger arrays for practical applications such as grid-connected power plants, solar pumping systems, solar cars, and street lighting [28].

A typical solar cell consists of a thin semiconductor layer with a band gap that allows electrons to be excited by incoming photons, an anti-reflective coating to maximize light absorption, a top conductive grid, and a bottom conductive metal contact. Recent designs also integrate reflective multilayers beneath the semiconductor to increase photon trapping and enhance efficiency [31]. To reduce material use and costs, the industry has progressively decreased silicon wafer thickness from over 300 µm in earlier generations to about 150–180 µm in recent years. Research on ultra-thin cells, sometimes only a few hundred nanometers thick, has achieved high efficiencies, but their high production costs restrict such technologies mainly to space and specialized applications [28, 29].

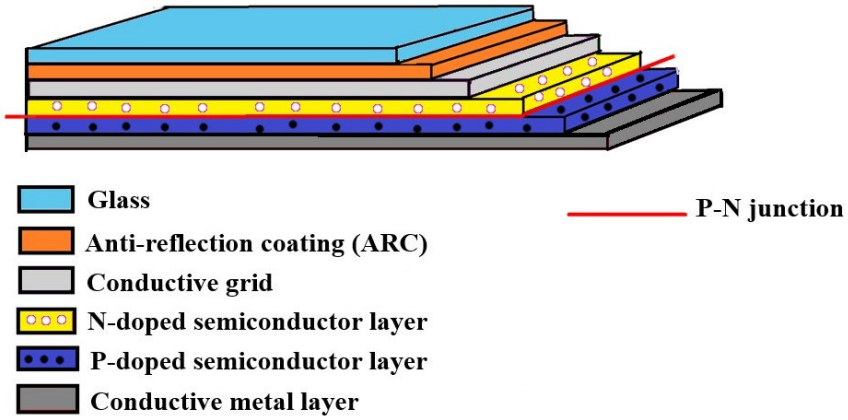

Figure 1.11 Solar cell structure.

PV cells differ mainly by the materials and manufacturing methods used, which determine their cost and efficiency. Monocrystalline silicon cells, grown from a single crystal ingot using techniques such as Czochralski or floating zone, are the most efficient silicon technology, with laboratory efficiencies near 27%, commercial cells at 21–23%, and modules at 19–21% [30]. Polycrystalline silicon cells, made by casting molten silicon into blocks of multiple crystals, are cheaper but slightly less efficient, with laboratory cells around 23% and commercial modules in

the 17–19% range [31]. Another type called Thin-film technologies use semiconductor layers only about one micron thick, reducing material use and cost. Their performance depends on the material: amorphous silicon modules achieve 6–10%, cadmium telluride (CdTe) modules about 18% with record cells above 22%, and copper indium gallium selenide (CIGS) modules 15–18% with record cells over 23%. Thin films are widely used in building integration and portable electronics and are typically fabricated by chemical vapor deposition on glass, plastic, or metal substrates [27]. The three technologies are depicted in the PV modules in Fig. 1.12.

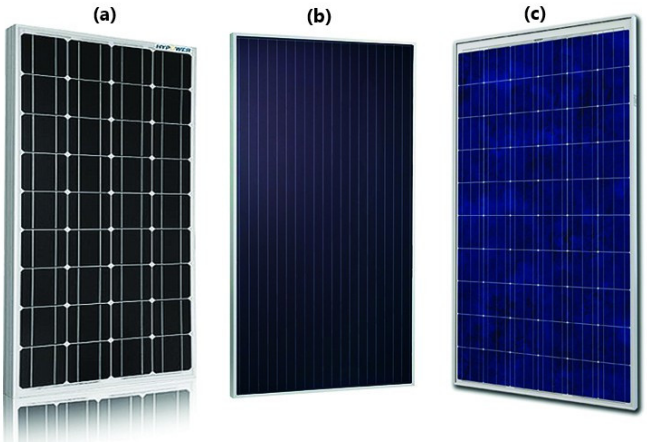

Figure 1.12 PV modules technologies: (a) monocrystalline, (b) thin-film amorphous, and (c) polycrystalline.

1.3.2 Classification of the PV systems

From a capacity perspective, photovoltaic (PV) systems can be grouped into three categories. Small-scale systems typically consist of residential rooftop installations, usually producing up to a few kilowatts. Medium-scale systems are more common in commercial settings and can reach outputs in the range of several hundred kilowatts. At the highest level, large-scale utility systems are designed to supply the grid, with capacities extending to tens of megawatts. On a global scale, these categories are generally recognized as the three main types of PV systems [8, 32], as illustrated in Fig. 1.13:

- Stand-alone alone PV systems.
- Hybrid PV systems.
- Grid-connected PV systems.

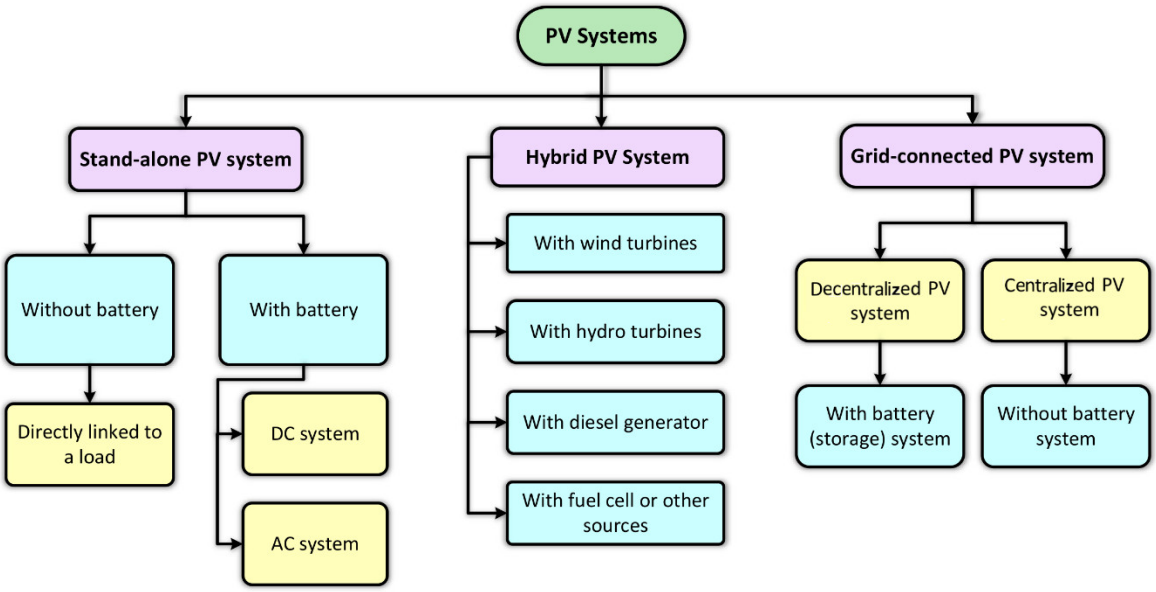

Figure 1.13 PV system classification

1.3.2.1 Stand-alone alone PV systems:

Stand-alone PV systems operate independently from the utility grid and are designed to supply DC and/or AC loads. The simplest type is the direct-coupled system, where the PV module is directly connected to a DC load, allowing operation only during sunlight hours. Such systems are commonly used in applications like water pumping, ventilation fans, and circulation pumps [30]. For continuous operation, especially during night or low sunlight, stand-alone systems are often combined with battery storage. Common storage technologies include lead-acid, nickel-cadmium, lithium-ion, sodium-sulfur, and advanced flow batteries such as vanadium redox or zinc-bromine. To ensure reliable operation, charge controllers are required to regulate charging and discharging, with shunt, series, and maximum power point tracking (MPPT) types being the most common. These systems can also incorporate inverters to power AC loads and are widely applied in home electrification, telecommunications, military operations, and water pumping [33].

1.3.2.2 Hybrid PV systems:

This type integrates PV panels with complementary energy sources—such as wind turbine, diesel/gas generators, or the utility grid—to provide a stable and continuous electricity supply. Unlike standalone PV systems, hybrids can store excess solar energy in batteries for later use and draw from backup sources during low solar generation, ensuring higher reliability, energy security, and flexibility in both on-grid and off-grid applications.

1.3.2.3 Grid-connected PV systems:

Residential and commercial buildings are increasingly adopting utility-interactive photovoltaic (PV) systems, which are expected to play a major role in electricity generation. By connecting directly to the power grid, these PV systems can supply large amounts of high-quality energy close to where it is consumed, reducing transmission and distribution losses. Operating in parallel with the existing grid, they enable the bidirectional flow of electricity—both to and from the network. As shown in Fig. 1.14 [8, 34], grid-connected PV systems are generally classified into two main types.

- **Decentralized grid-connected PV systems:** in such a system, energy storage is not required because solar irradiation gives power to the houses and if there is surplus energy it can be injected into the grid . In this case, the inverter must integrate harmoniously with the energy (voltage and frequency) offered by the grid. During the night or at instants when the PV power is insufficient, the grid can be used as a storage system and will feed the houses [33].
- **Centralized grid-connected PV systems:** these are large PV power plants that are directly connected to the utility's transmission or distribution network (the central grid). The electricity produced is not used on-site but is fed into the grid, supplying power to many consumers through the utility infrastructure [30].

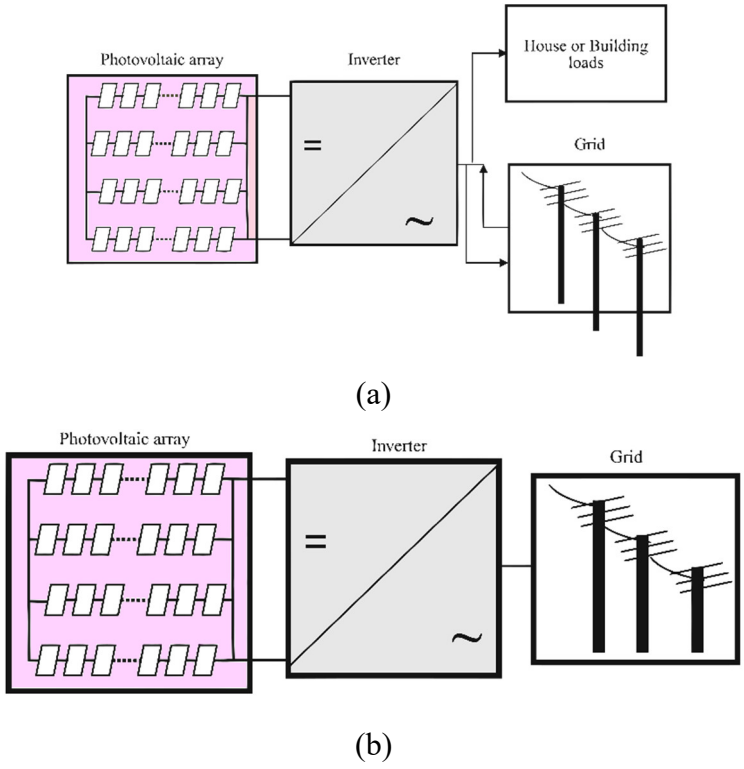

Figure 1.14 Types of grid-connected PV systems: (a) decentralized, (b) centralized

In general, grid-connected PV systems are most commonly classified based on their topology, control structure, and the position of the MPPT unit. According to this classification, they are broadly divided into two categories: single-stage and double-stage grid-connected PV systems [6]. In a single-stage configuration shown in Fig. 1.15(a), the PV array is directly interfaced with the grid through a single power conversion stage, where the inverter is responsible for both MPPT operation and grid integration. This reduces complexity and cost but increases the control burden on the inverter. On the other hand, in a double-stage configuration (see Fig. 1.15(b)), the PV system includes a DC–DC converter followed by a DC–AC inverter. The DC–DC converter typically handles MPPT and DC voltage regulation, while the inverter ensures proper grid synchronization and power quality. This separation of functions offers more flexibility and higher performance at the expense of added components and control complexity [35, 36]. In this thesis, the double-stage grid-connected PV system will be employed for modeling and the implementation of the control strategy.

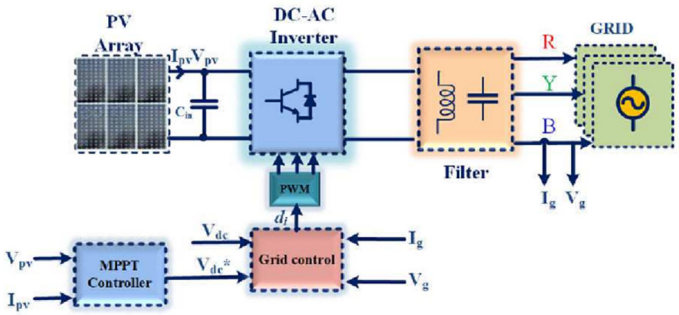

(a) single-stage

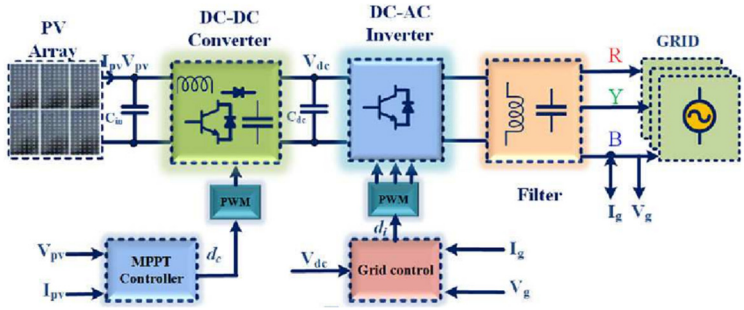

(b) two-stage

Figure 1.15 Grid-connected PV system topologies

1.4 Control requirements in grid-connected PV systems

The control of grid-connected PV systems is essential for ensuring efficient energy extraction, reliable grid interaction, and compliance with international standards. The requirements can broadly be divided into two categories: those under normal grid operating conditions and those under grid fault or disturbance conditions.

1.4.1 Control requirements under normal grid conditions

During stable grid operation, the control objectives focus on maximizing energy yield and ensuring power quality [6, 36, 37]. The main requirements are:

- **Maximum Power Point Tracking (MPPT):** the PV system must continuously operate at its maximum power point despite variations in irradiance and temperature, thereby maximizing energy conversion efficiency.
- **DC-Link Voltage Regulation (for two-stage systems):** a stable DC-link voltage must be maintained to decouple the PV array dynamics from the inverter and guarantee smooth power transfer to the grid.
- **Grid Current Control and Power Quality:** the injected grid current should be sinusoidal with low harmonic distortion and comply with international standards such as those defined by IEEE and IEC. Unity or controllable power factor operation is also required to ensure efficient power exchange.
- **Grid Synchronization:** accurate synchronization of the inverter with the grid voltage in terms of frequency, phase, and amplitude is necessary for stable operation. Phase-locked loop (PLL) techniques are commonly employed for this purpose.
- **Active and Reactive Power Control:** in compliance with modern grid codes, PV inverters must not only deliver active power but also provide reactive power support to aid in voltage regulation and enhance system stability.

1.4.2 Control requirements under grid fault or disturbance conditions

During abnormal grid events such as voltage sags, swells, or frequency deviations, additional control requirements come into play to ensure system stability and grid support [38]:

- **Fault ride-through (FRT) / Low-voltage ride-through (LVRT):** instead of disconnecting during short-term disturbances, the PV system must remain connected and ride through the fault while supporting the grid.
- **Dynamic reactive power injection:** under fault conditions, inverters are often required to supply reactive current to support grid voltage recovery, as mandated by many grid codes.
- **Current limitation and protection:** the control system must restrict inverter current during fault conditions to avoid damage to the power electronic devices while still complying with grid-support requirements.

- **System stability and safe recovery:** after fault clearance, the PV system must return smoothly to normal operation without inducing oscillations or instability in the grid or the PV array.

1.5 Literature review

Building upon the general overview of PV technologies, this section critically reviews recent contributions on grid-connected PV system modeling and control, highlighting gaps relevant to this thesis. The discussion is organized into three main themes: system design and modeling, control and synchronization strategies, and grid code compliance.

- **System design and modeling**

Several studies have examined grid-connected PV systems of varying scales, but important aspects of detailed modeling remain underexplored. In their study, A. Refaat et al. [12] developed a control and modeling strategy for a grid-connected PV installation rated at 500 kW and configured as a three-phase two-stage system, achieving a peak efficiency of 98.6% with an incremental conductance (INC)-based MPPT. However, their work did not include parameter identification of the series and shunt resistances of the PV module (R_s and R_p), inverter controller and PLL tuning methods, or detailed filter design. Similarly, N. Motan et al. [13, 39] provided more detail in the design and modeling of the DC/DC converter and the filter for a small-scale 6 kW two-stage grid-connected PV system with perturb-and-observe (P&O)-based MPPT, reaching a static inverter efficiency of 96%. Yet, they also omitted R_s/R_p identification, PLL and VSI controller tuning, and total conversion efficiency analysis.

While A. Islam [40] developed a Simulink-based PV model of cells and modules using the two-diode model, [41] proposed an easy and accurate method for modeling PV arrays based on the single-diode model. However, a key limitation in the literature is the reliance on generic PV models without extracting parameters from real panel data or incorporating manufacturer specifications for individual components at each stage. For example, S. V. Rajani and V. J. Pandya [14] compared INC and P&O MPPT techniques through MATLAB/Simulink simulations but did not include accurate PV array modeling or detailed boost converter designs. Similarly, other studies [42, 43] overlooked critical design specifications for DC-DC converter components, such as inductance and capacitance values. At the AC stage, resonance mitigation of a grid-connected LCL filter using different damping techniques has been examined in [44], highlighting the importance of detailed filter modeling and appropriate selection of damping

methods—an aspect often underrepresented in PV system studies. These simplifications reduce performance accuracy and limit the applicability of results to real-world systems. To the best of the author's knowledge, no study has yet modeled or validated a large-scale PV system in Algeria using real plant data, further emphasizing the need for research grounded in actual field measurements.

- **Control and synchronization strategies**

Beyond hardware modeling, several contributions have focused on advanced control methods. E. M. Khawla et al. [45] proposed a low-voltage ride-through (LVRT) strategy for a 100 kW PV system, while B. S. Mahdi et al. [46] investigated a larger 250 kW three-phase three-level NPC inverter model. Both studies, however, were constrained by generic assumptions, limited depth in modeling the DC and AC stage components, and incomplete consideration of grid code requirements.

M. P. Thakre et al. [47] presented an overview of both basic and advanced PLL methods, such as the synchronous reference frame PLL (SRF-PLL), also known as dq-PLL, the stationary reference frame PLL (αβ-PLL), and the dual second-order generalized integrator PLL (DSOGI-PLL), under various grid conditions. This comparative analysis provided insights into synchronization techniques but did not address the tuning process of these methods.

Optimization-based approaches have also emerged. M. Gupta et al. [48] introduced a bio-inspired Grey Wolf Optimization (GWO) approach for real-time PID tuning in a 5 kW inverter system, partially addressing the recurring gap in systematic controller tuning. However, their validation against IEEE 519-1992 was not rigorous, as they evaluated current total harmonic distortion (THD) rather than total demand distortion (TDD). More recently, M. H. Mohamed Hariri et al. [49] proposed a cascaded delay signal cancellation (CDSC)-based synchronization mechanism combined with a Cuckoo Search (CS) MPPT method and explicit filter design steps, reporting an MPPT efficiency of 96%. Despite these advances, the R_s/R_p identification method remained unspecified, the overall efficiency breakdown of the model was not provided, and comprehensive grid code validation was still not fully addressed.

- **Grid code compliance**

While progress has been made in PV system modeling and control, validation against international grid standards remains partial. While some works confirmed compliance with the

IEEE 929-2000 unity power factor clause 4.5 only [12, 13, 39, 45, 46, 48, 49], the requirements of IEEE 519-1992 and EN 50160 were either overlooked or misapplied. In particular, many studies reported current total harmonic distortion (THDi) as the sole quality metric, even though IEEE 519-1992 specifies current total demand distortion (TDD). Moreover, none of the reviewed studies verified synchronism within the ±1% frequency tolerance mandated by EN 50160 [50].

This indicates that integration of grid codes into PV system modeling and testing is still not systematically achieved, despite broader reviews addressing stability and converter control in renewable-based grids [51, 52]. Comprehensive compliance assessment therefore remains an open issue, especially for large-scale systems intended for real grid operation.

1.6 Thesis contribution

This thesis develops, implements and validates a detailed, component-level model and control strategy for a 1 MW grid-connected photovoltaic (PV) system based on real specifications and operational data from the Oued El Kebrit (OKP) 15 MW_p PV plant (Souk Ahras, Algeria). The main contributions of this theis can be summarized as follows:

- Unlike many existing studies that rely on generic assumptions, this work incorporates manufacturer parameters and real field measurements to enhance model accuracy and realism. In this respect, to the best of the author's knowledge, this constitutes the first validated large-scale PV system model based on an Algerian solar plant.
- A further contribution is the rigorous design and modeling of both the DC and AC stages of the system. At the DC side, a PV array model is established using the single-diode representation, with series and shunt resistances extracted through an iterative identification procedure. The DC/DC boost converter is then designed to optimize energy transfer, and a comparative study of maximum power point tracking (MPPT) techniques is made to choose a suitable method among the hill climbing and the Incremental Conductance algorithm under dynamic operating conditions. At the AC side, the system design encompasses the SPWM-based two-level voltage source inverter, an LCL filter with passive damping for harmonic mitigation, and a synchronous reference frame phase-locked loop (SRF-PLL) for grid synchronization. The dual-loop inverter controllers are tuned using the symmetrical optimum method, ensuring stable operation and precise current injection into the grid.

- In addition, this thesis explicitly addresses grid code compliance. The system's performance is evaluated with respect to IEEE 929-2000, IEEE 519-1992, and EN 50160 standards, with particular emphasis on total demand distortion (TDD) rather than total harmonic distortion (THD) alone. The objective is to verify whether the proposed control and filtering strategies ensure compliance with international harmonic standards under both steady-state and transient conditions, while also maintaining synchronism within the tolerance limits defined by EN 50160. Furthermore, carrying out a detailed efficiency analysis to assess the consistency of the simulated model with the performance expected from utility-scale PV systems.
- Subjecting the integrated system to extensive dynamic testing under standard test conditions, sudden irradiance variations, and real plant operating data, and then analyzing the robustness of the control strategies, the reliability of the synchronization mechanism, and the validity of the proposed modeling methodology.

Beyond the immediate case study, this thesis contributes by establishing a transferable framework for the design, modeling, and validation of grid-connected PV plants. The proposed model outlines a systematic procedure—ranging from parameter identification and converter/filter sizing to controller tuning and grid code verification—that can be adapted to large-scale PV installations worldwide, thereby ensuring both academic significance and industrial applicability.

In the following chapters, the developed model and control strategy are founded on a double-stage system configuration illustrated in Fig. 1.16 and its associated components.

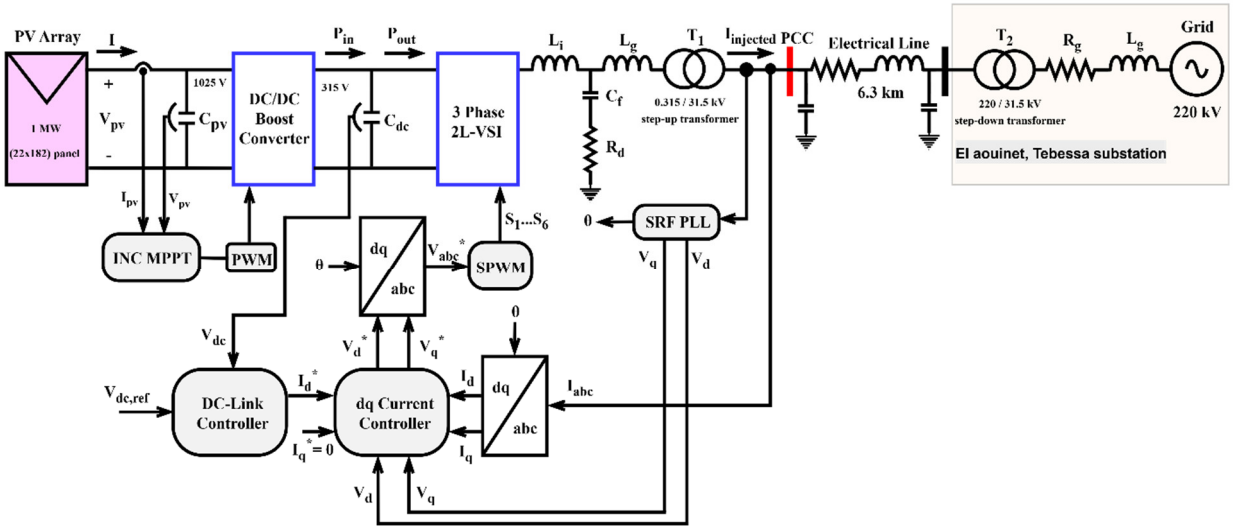

Figure 1.16 Layout of the grid-connected PV system under study

1.7 Thesis outline

The present doctoral thesis has been structured as follows:

- Chapter I introduces the context of the global energy transition and the role of photovoltaics in sustainable electricity generation. It outlines Algeria's renewable energy objectives, highlights its solar potential and the Oued El Kebrit PV plant as a case study, and reviews the fundamentals of PV technology. The chapter also discusses PV system classifications, control requirements for grid-connected PVs, and identifies the research gaps addressed by this work.
- Chapter II addresses the DC stage of the grid-connected PV system. It begins with the principles of PV cell operation and array formation, followed by the adoption of the one-diode model for mathematical representation. Series and shunt resistances are iteratively estimated for the Yingli Solar YL250P-29b module and validated in MATLAB/Simulink. A boost converter is then designed to match PV array output with inverter requirements. Maximum Power Point Tracking (MPPT) methods, namely Hill Climbing and Incremental Conductance, are evaluated under dynamic conditions such as cloud cover. Simulation results help in choosing one of them as the MPPT technique.
- Chapter III examines the AC stage of the grid-connected PV system, with emphasis on inverter operation, harmonic mitigation, synchronization, and control. It begins with DC-link voltage selection and the modeling of a two-level voltage source inverter (2L-VSI) using SPWM. A passive damped-LCL filter is designed to meet international power quality standards. Grid synchronization is achieved via an SRF-PLL, while inverter current injection is regulated by a dual-loop control strategy tuned with the Symmetrical Optimum method. Transmission line parameters of the Oued El Kebrit PV plant are analytically derived to replicate real operating conditions. All models are validated in MATLAB/Simulink using actual plant data.
- Chapter IV presents the complete 1 MW grid-connected PV system model and its performance evaluation. Both steady-state and dynamic scenarios are examined, with analysis of efficiency, stability, and power quality indices. Benchmarking against the literature and validation with real plant data to analyze the accuracy and reliability of the proposed model and control strategy.

Chapter II

DC-Side Control Strategy for Grid-Connected PV Systems

2.1 Introduction

As discussed in the previous chapter, a grid-connected photovoltaic (PV) system operates as a unit for producing electrical energy, injecting the generated power directly into the grid. Such systems typically have a nominal power rating greater than 100 kW. The main components of a two-stage grid-connected system, including the PV array, the DC-DC boost converter, the maximum power point tracking (MPPT) controller, the voltage source inverter (VSI), the LCL filter, the phase-locked loop (PLL), the DC-link voltage controller, and the current controller, were reviewed in the literature.

In this chapter, the focus is placed on the DC stage of the system. Specifically, the mathematical modeling and design of the one-megawatt PV array from the Oued El Kebrit PV plant, the DC-DC boost converter, and the MPPT controller are developed. The operating principles of these components are presented, and their corresponding mathematical models are established. For the PV array, the one-diode model is selected due to its ability to accurately represent the static behavior of the module while maintaining simplicity. The effect of irradiance and temperature on the model parameters is considered, and an iterative method is applied to determine the series and parallel resistances of the selected PV module.

Furthermore, the design of a boost converter for the 1 MW PV array is carried out to ensure maximum power extraction. In order to select a suitable MPPT controller, two commonly used algorithms—Hill Climbing and Incremental Conductance—are investigated under operating scenarios that reflect real-life conditions in PV plants. The comparative analysis highlights the strengths and limitations of each method and provides the basis for choosing the most appropriate controller.

Finally, at the end of the presentation of each component, a simulation is performed using the MATLAB/Simulink environment to verify the validity of the developed models and to evaluate the performance of the designed system.

2.2 Photovoltaic generator

2.2.1 Working principle of PV cell

The working principle of a photovoltaic (PV) cell is based on the ability of semiconductor materials to absorb light energy. Therefore, the selection of materials for PV cells depends on their physical properties, specifically how their electrons behave. When photons from sunlight, which carry energy corresponding to their wavelength, strike the material, they can excite these electrons and free them from their atoms [53].

As sunlight hits the cell, photons pass into the semiconductor layers and transfer their energy to electrons through collisions. This energy transfer creates electron-hole pairs within the cell's depletion region. The internal electric field present at the PN junction then drives these charges toward the respective P and N type metallic contacts, with electrons being drawn toward the N region and holes toward the P region. This movement of charges generates a voltage, typically between 0.5 and 0.6 volts, across the cell's electrodes [54]. This entire process of converting light into electricity involves the following key mechanisms [55]:

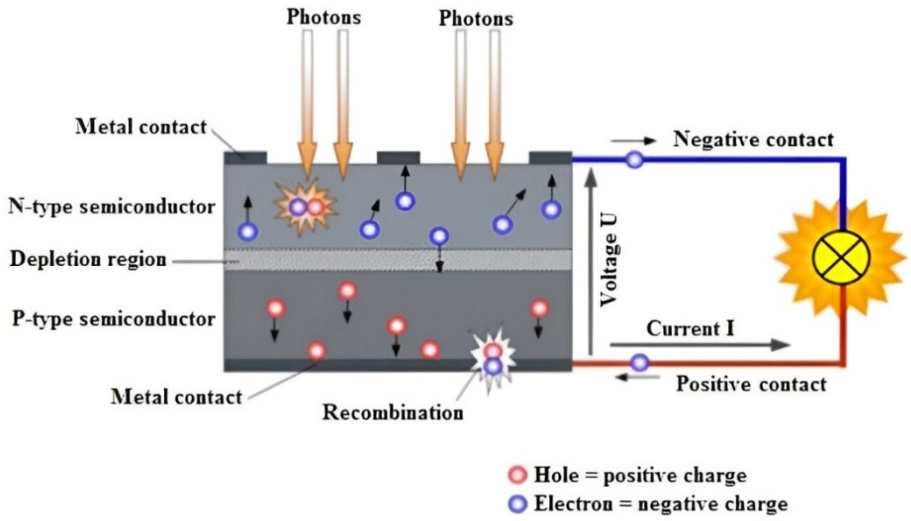

Figure 2.1 Operational mechanism of a photovoltaic cell.

- The semiconductor material absorbs photons whose energies are higher than its band gap.
- The absorbed photon energy creates electron–hole pairs by exciting electrons inside the semiconductor.
- The internal electric field separates and directs these charge carriers, allowing electrons and holes to move and generate current through the external circuit.

2.2.2 Creating PV array

A photovoltaic (PV) array is formed by connecting multiple modules in series and parallel configurations to achieve the specific voltage and current levels required for a given application as depicted in Fig. 2.3. Each module is itself composed of numerous interconnected PV cells. A series connection of modules, known as a string, increases the overall voltage; the total string voltage is the sum of the individual module voltages, while the string's current is limited to that of the module with the lowest output. Conversely, connecting modules in parallel increases the

total current, which becomes the sum of the currents from each module, while the voltage remains equivalent to that of a single module [27].

The electrical characteristics of PV modules are provided by the manufacturer in publicly available datasheets. These specifications are essential for the proper design of a PV array, as illustrated in Fig. 2.2. It is critical for designers to verify that all modules used are identical by confirming the datasheet details with the manufacturer. This practice helps to prevent performance losses caused by electrical mismatch between non-identical modules [56].

The mismatch effect occurs when dissimilar modules are connected in series, causing their voltages to add together (see Fig. 2.2(a)), but the overall current is constrained to the lowest current produced by any module in the string (e.g., 4A). Similarly, when non-identical modules are connected in parallel as seen in Fig. 2.2(b), their currents add together, but the resulting voltage is equal to the lowest voltage among the modules. The total power output of the modules is calculated using the formula $P = I \times V$ [57].

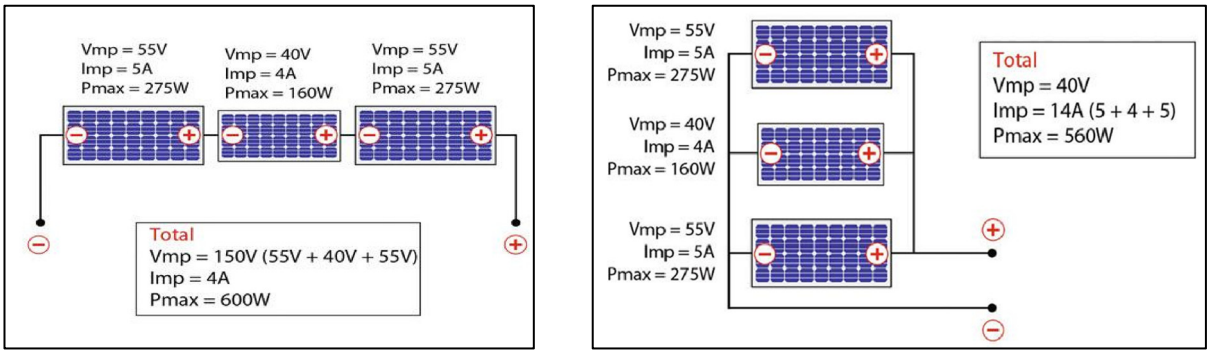

(a) (b)

Figure 2.2 Mismatching Losses [57].

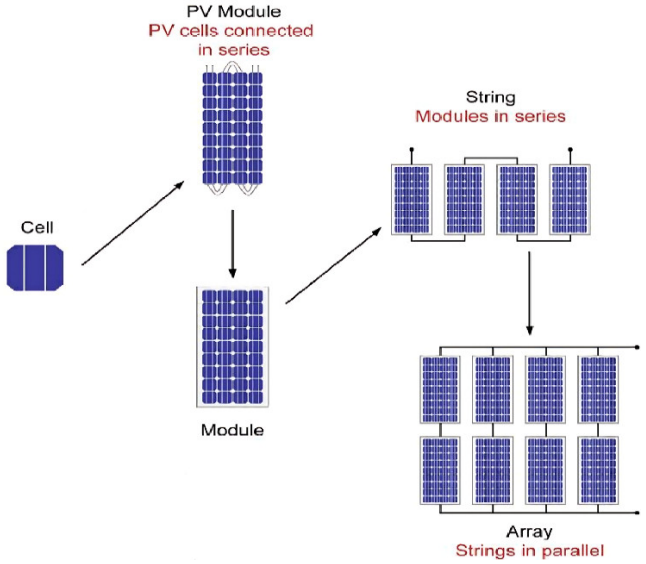

Figure 2.3 PV array creation process [57].

2.2.3 PV cell models

The electrical modeling of a PV cell aims to approximate its current–voltage (I–V) characteristic, defined by key parameters such as the open-circuit voltage (V_{oc}), the short-circuit current (I_{sc}), and the maximum power point values (I_{mp} and V_{mp}). To develop a mathematical model, the equivalent electrical circuit of the PV cell must first be identified [41]. Because of the highly non-linear behavior of the semiconductor junction, several mathematical models have been proposed to represent PV cells, such as single-, double-, and triple-diode designs. According to [58], single-diode and double-diode models are commonly used.

- **Two-diode model (**Double exponential**):**

As shown in Fig. 2.4, the two-diode model is based on the physical behavior of p–n junctions. In this representation, a PV cell is modeled as a direct current (DC) source connected in parallel with two diodes [58]. These diodes account for the current losses caused by diffusion and charge recombination mechanisms. Additionally, two resistances are included in the model: the series resistance (R_s), which represents contact and wiring losses, and the parallel resistance (R_p), which represents the internal leakage resistance of the PV cell [59].

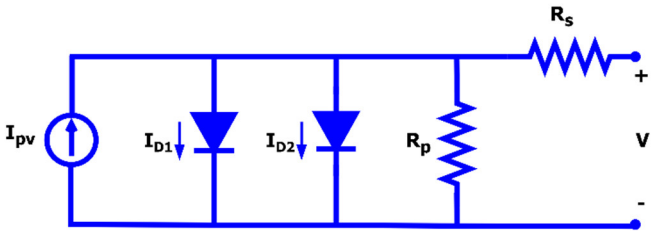

Figure 2.4 Two-exponential PV cell model.

The characteristic equation of this model is featured with the presence of a second term in exponential [60, 61]:

$$\begin{cases} I = I_{PV} - I_{D1} - I_{D2} - \dfrac{V + IR_s}{R_p} \\ I = I_{PV} - I_{01}\left[exp\left(\dfrac{q(V + IR_s)}{\alpha kT}\right) - 1\right] - I_{02}\left[exp\left(\dfrac{q(V + IR_s)}{\beta kT}\right) - 1\right] - \dfrac{V + IR_s}{R_p} \end{cases} \quad (2.1)$$

Where:

- I_{PV} is the photocurrent generated internally by the PV cell,
- I_{D1} and I_{D2} are the currents flowing through diodes D_1 and D_2 (in amperes),
- α and β are the diode ideality factors, typically ranging between 1 and 2,
- k is the Boltzmann constant (1.3806503×10^{-23} J/K)
- T is the cell temperature (in Kelvin),
- q is the electron charge (1.60217646×10^{-19} C)

- I_{01} and I_{02} are the reverse saturation currents of diodes D_1 and D_2, respectively, which vary with the junction temperature.

- **R_s** represents the series resistances of the metallic contacts and connections. It is typically very low (on the order of a few milliohms), but when abnormally high, it can significantly decrease the short-circuit current.
- **R_p** characterizes the leakage currents due to the diode and the edge effects of the junction. It is typically very high (on the order of megaohms). A low shunt resistance reduces the open-circuit voltage; moreover, if R_p is too low, the cell will no longer produce voltage under low illumination.

- **One-diode model (**Single exponential**):**

A simplified and widely adopted model for the photovoltaic cell is shown in Fig. 2.5. This model is derived by neglecting the minimal current passing through diode D_2, which represents charge recombination losses. It offers a suitable balance between accuracy and computational simplicity, and it has been widely employed in several previous studies [41].

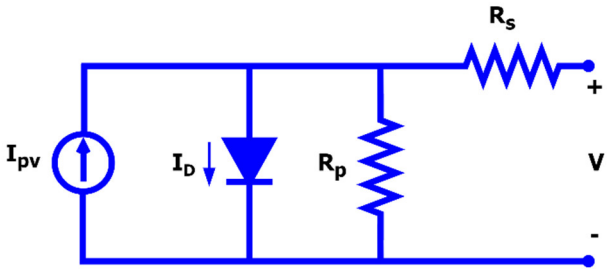

Figure 2.5 One-diode PV cell model.

In this case, the current I_{D2} is omitted from Eq. (2.1), and the relationship reduces to:

$$I = I_{PV} - I_0\left[exp\left(\frac{q(V+IR_s)}{akT}\right)-1\right]-\frac{V+IR_s}{R_p} \tag{2.2}$$

A PV panel consisting of N_s cells connected in series can be represented by the following mathematical model [27]:

$$I = I_{PV} - I_0\left[exp\left(\frac{q(V+IR_s)}{akTN_s}\right)-1\right]-\frac{V+IR_s}{R_p} \tag{2.3}$$

It is possible to find the series (R_s) and shunt (R_p) resistance values by taking direct measurements or by using iterative methods that fit a curve to the panel's I-V characteristic. As an example, the authors of [41] employed these curve fitting techniques to calculate approximations for R_s and R_p.

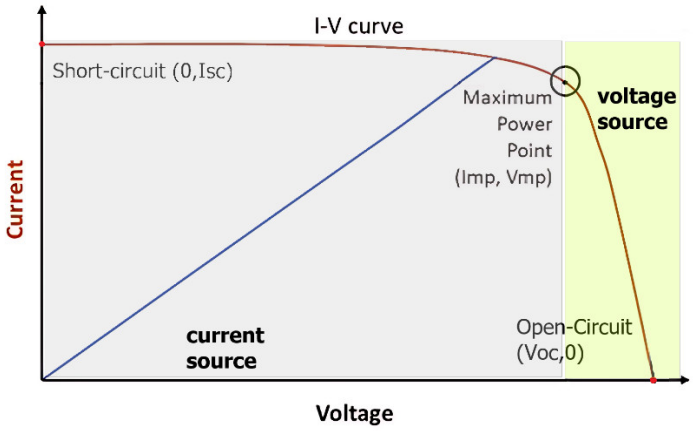

Figure 2.6 Typical I-V curve showing the three critical points.

The voltage at the terminals of a photovoltaic (PV) cell and its resulting current have a nonlinear relationship [62]. This is due to the exponential function found in Eqs. (2.1) and (2.2), which originates from the properties of the p-n semiconductor junction within the cell. Consequently, the cell's current-voltage (I-V) characteristic curve is unique and can be separated into three distinct regions, as shown in Fig. 2.6.

2.3 Modeling PV array

2.3.1 Mathematical equations

The electrical model of the PV array was simulated in MATLAB/Simulink using the equivalent circuit model shown in Fig. 2.7. In this model, the single-diode parameters (I_{PV}, I_0, R_s, R_p) are determined through mathematical relationships based on meteorological data, specifically solar irradiation and temperature.

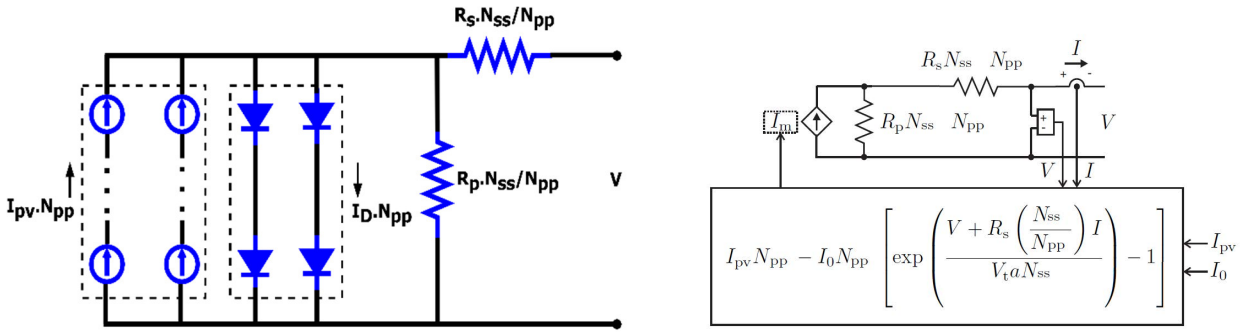

(a) equivalent circuit (b) model

Figure 2.7 Equivalent circuit and model of a PV array with N_{ss} x N_{pp} modules.

For an array composed of $N_{ss}\times N_{pp}$ identical modules, the equivalent I–V relationship can be expressed as follows [63]:

$$I = I_{PV}N_{pp} - I_0 N_{pp}\left[exp\left(\frac{V + IR_s\left(\frac{N_{ss}}{N_{pp}}\right)}{aV_t N_{ss}}\right) - 1\right] - \frac{V + IR_s\left(\frac{N_{ss}}{N_{pp}}\right)}{R_p\left(\frac{N_{ss}}{N_{pp}}\right)} \tag{2.4}$$

Here, I_{PV} and I_0 represent the light-generated current and the saturation current of the array, respectively. V_t denotes the thermal voltage of the array with N_s cells connected in series. N_{ss} refers to the number of modules connected in series, while N_{pp} represents the number of parallel strings. To generate the input supply, or model current (I_m), for the equivalent PV circuit, the saturation current (I_0) must first be determined [64]. This is calculated using Eqs. (2.5) and (2.6).

$$I_0 = \frac{I_{sc,n} + K_i\Delta T}{\exp\left(\frac{V_{oc,n} + K_v\Delta T}{aV_t}\right) - 1} \tag{2.5}$$

$$V_t = \frac{N_s kT}{q} \tag{2.6}$$

Here, the current and voltage coefficients are represented by K_v in volts per kelvin (V/K) and K_i in amperes per kelvin (A/K). The light-generated current (I_{PV}) is then calculated using Eq. (2.7).

$$I_{PV} = (I_{pv,n} + K_i\Delta T)\frac{G}{G_n} \tag{2.7}$$

$I_{pv,n}$ (A) represents the current generated by light under nominal conditions, typically set at 25 °C and 1000 W/m². The term $\Delta T = T - T_n$ denotes the difference between the actual temperature (T) and the nominal temperature (T_n), both expressed in Kelvin. G (W/m²) refers to the solar irradiation on the device surface, while G_n indicates the nominal irradiation level.

Finally, both parameters, I_0 and I_{PV}, are substituted into Eq. (2.8) to determine the input supply current (I_m) [63].

$$I_m = I_{pv}N_{pp} - I_0 N_{pp}\left[\exp\left(\frac{V + IR_s\left(\frac{N_{ss}}{N_{pp}}\right)}{aV_t N_{ss}}\right) - 1\right] \tag{2.8}$$

2.3.2 Estimation of series and parallel resistances

In Eq. (2.4), two parameters remain unknown: R_s and R_p of the PV module. In [65], an iterative method was proposed to estimate these values. The objective is to determine R_s (and consequently R_p) such that the maximum power point of the mathematical model ($P_{max,m}$) coincides with the experimental maximum power ($P_{max,e}$) at the coordinates (V_{mpp},I_{mpp}). This

process requires multiple iterations until the condition $P_{max,m}=P_{max,e}$ is satisfied. It is assumed that there exists a unique pair $\{R_s,R_p\}$ that ensures this condition at the MPP.

In this work, the Newton-Raphson method (NRM) is applied to solve Eq. (2.3) and the convergence criterion is defined by Eq. (2.13). Where ε is the tolerance.

$$P_{\max,m} = V_{mp}\left\{I_{PV} - I_0\left[\exp\left(\frac{q}{kT}\frac{V_{mp}+R_s\,\mathrm{I}_{mp}}{aN_s}\right)-1\right]-\frac{V_{mp}+R_s\,\mathrm{I}_{mp}}{R_p}\right\} = P_{\max,e} \tag{2.9}$$

$$R_p = \frac{V_{mp}\left(V_{mp}+\mathrm{I}_{mp}\,R_s\right)}{\left\{V_{mp}I_{PV} - V_{mp}I_0\exp\left[\frac{q}{kT}\frac{\left(V_{mp}+R_s\,\mathrm{I}_{mp}\right)}{aN_s}\right]+V_{mp}I_0 - P_{\max,e}\right\}} \tag{2.10}$$

$$R_{p,\min} = \frac{V_{mp}}{I_{sc,n}-\mathrm{I}_{mp}} - \frac{V_{oc,n}-V_{mp}}{\mathrm{I}_{mp}} \tag{2.11}$$

$$I_{pv,n} = \frac{\left(R_p+R_s\right)}{R_p} I_{sc,n} \tag{2.12}$$

$$\left|P_{\max,m} - P_{\max,e}\right| < \varepsilon \tag{2.13}$$

This iterative process involves expressing the current I_{pv} as a function of V_{pv}. Throughout this process, R_s is gradually increased from zero, while the initial value of R_p is determined using Eq. (2.11). Fig. 2.8 depicts the flowchart for this algorithm.

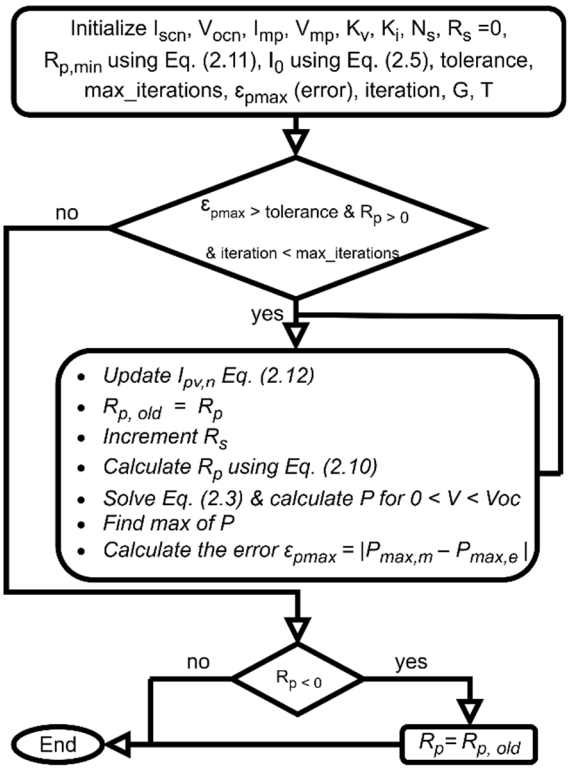

Figure 2.8 Flowchart of the iterative approach for determining R_s and R_p.

2.3.3 Simulation of PV array

A MATLAB script was created to estimate the values of R_s and R_p for the Yingli Solar YL250P-29b PV panel installed in Oued El Kebrit PV plant (see Appendix A), using the previously described algorithm. Based on the obtained values of R_s and R_p (presented in Table 2.1), along with Eqs. (2.4)-(2.7), and the manufacturer's datasheet seen in Table 2.1, the Simulink model of the 1 MW PV array was subsequently designed.

$\mathbf{I_{mp}}$	8.39 A
$\mathbf{V_{mp}}$	29.8 V
$\mathbf{P_{max,e}}$	250.022 W
$\mathbf{I_{sc,n}}$	8.92 A
$\mathbf{V_{oc,n}}$	37.6 V
$\mathbf{K_v}$	-0.1203 V/K
$\mathbf{K_i}$	0.0045 A/K
$\mathbf{N_s}$	60

Table 2.1 Datasheet parameters of YL250P-29b module at 25°C, 1000 W/m^2 [66].

$\mathbf{I_{mp}}$	8.39 A
$\mathbf{V_{mp}}$	29.8 V
$\mathbf{P_{max,m}}$	250.144 W
$\mathbf{I_0}$	$6.339.10^{-8}$ A
$\mathbf{I_{PV}}$	8.92 A
a	1.3
$\mathbf{R_s}$	0.256 Ω
$\mathbf{R_p}$	32248.31 Ω

Table 2.2 YL250P-29b panel parameters obtained from with the iterative algorithm

Fig. 2.9 illustrates the I–V and P–V characteristics obtained from the simulation of the PV module model under standard test conditions (STC), with solar irradiation G=1000 W/m^2 and temperature T=25°C. The simulated results are consistent with the manufacturer's datasheet values at STC.

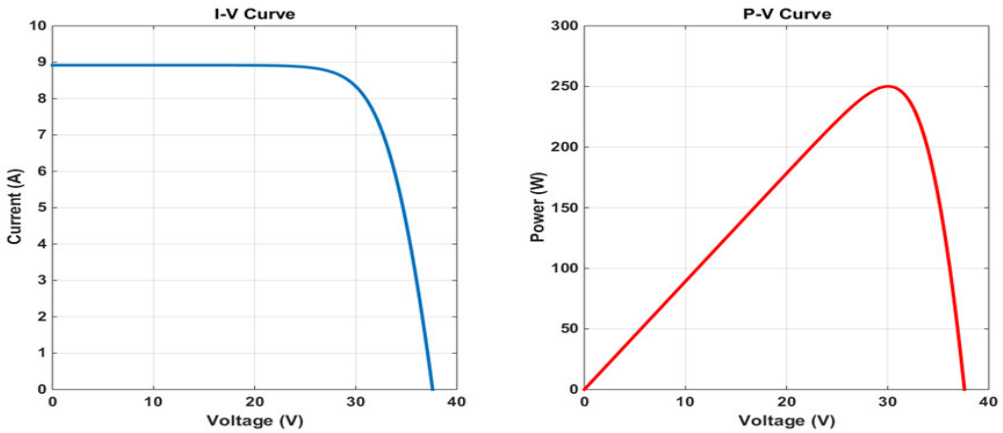

Figure 2.9 I-V and P-V of PV module characteristics for G = 1000W/m^2 and T = 25 °C.

The one-megawatt PV array utilized in this study consists of $N_{ss} = 22$ modules connected in series within each string, with $N_{pp} = 182$ strings arranged in parallel. To generate the I-V and P-V characteristics from the Simulink model, a controlled voltage source, ranging from 0 to $N_{ss}V_{oc} = 827.2$ V, is connected to the array's terminals, as illustrated in Fig. 2.10.

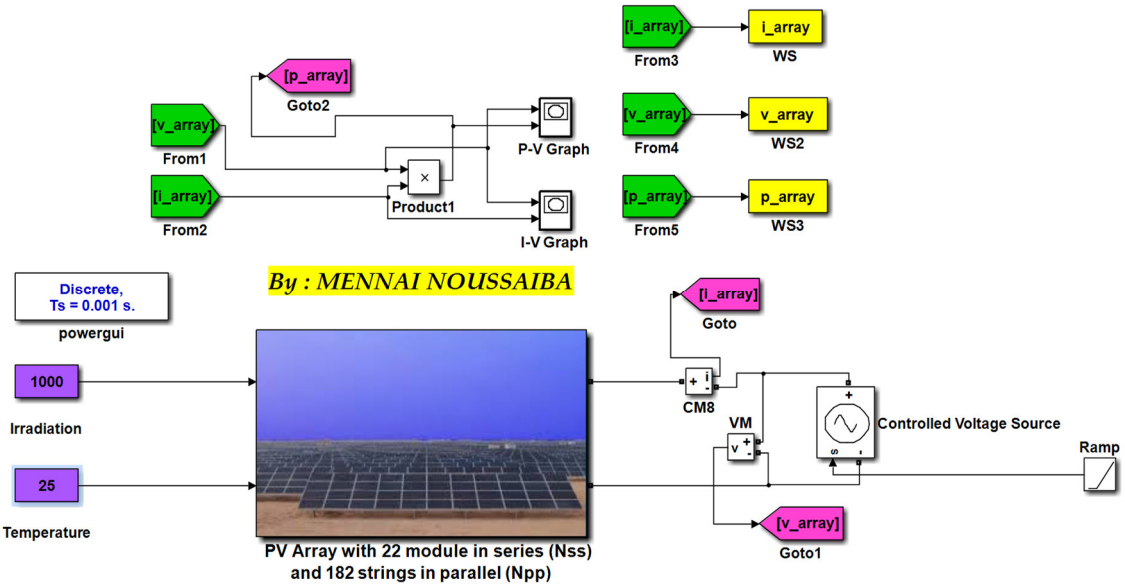

Figure 2.10 Simulation of the PV array with controlled voltage source.

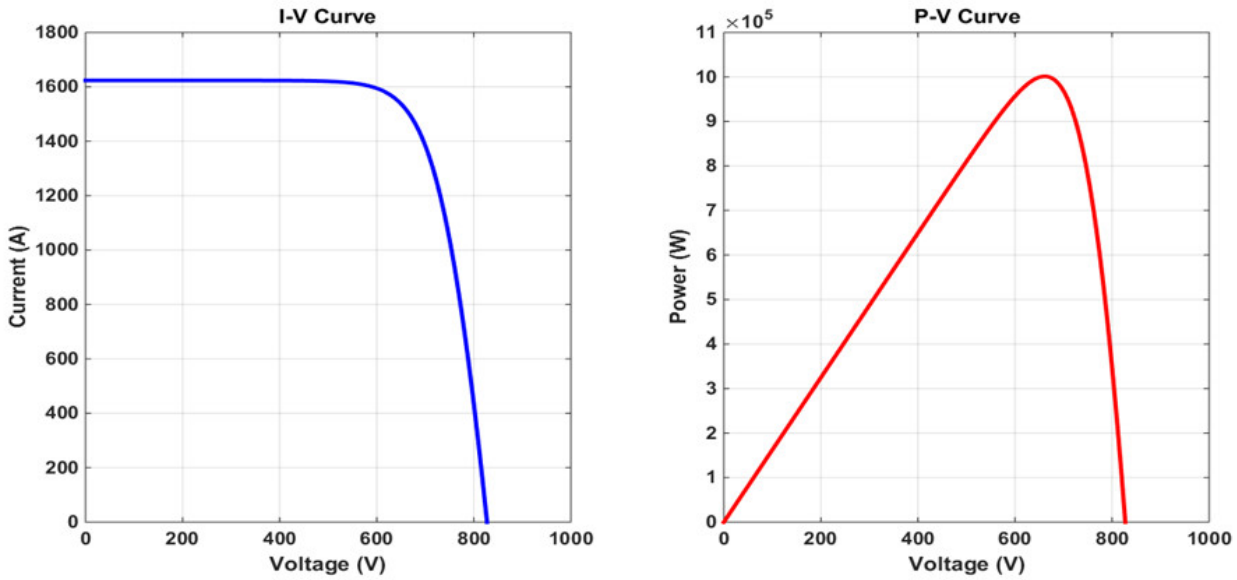

Figure 2.11 I-V and P-V curves of PV array at STC.

To study the effect of solar irradiation on the array, the temperature was fixed at 25 °C, and I–V and P–V curves were plotted for irradiation levels of 500, 800, and 1000 W/m² as indicated in Fig. 2.12(a) . The results show that the output current is directly proportional to irradiation, as

predicted by the model. Consequently, the output power of the array decreases from about 1 MW at 1000 W/m² to nearly 500 kW at 500 W/m², while the voltage shows only a small increase..

The effect of temperature was then examined at a constant irradiation of 1000 W/m², with module temperature varying between 25, 60, and 80 °C as indicated in Fig. 2.12(b). The results reveal that increasing temperature reduces both voltage and maximum output power, while slightly increasing the current.

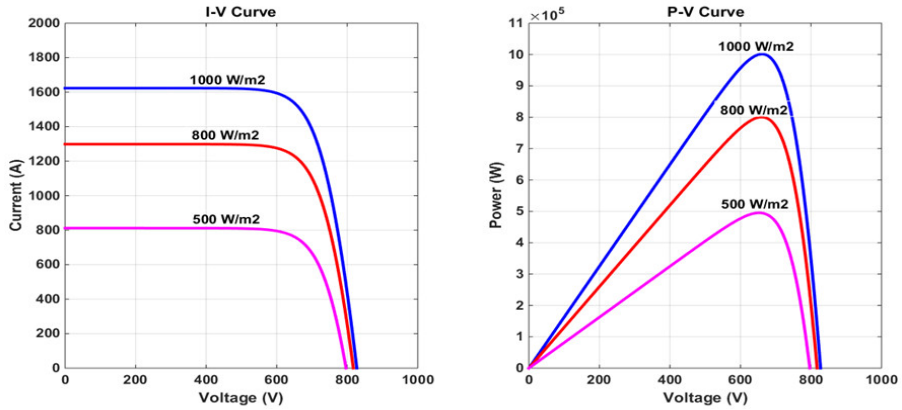

(a) I-V and P-V at various solar irradiations

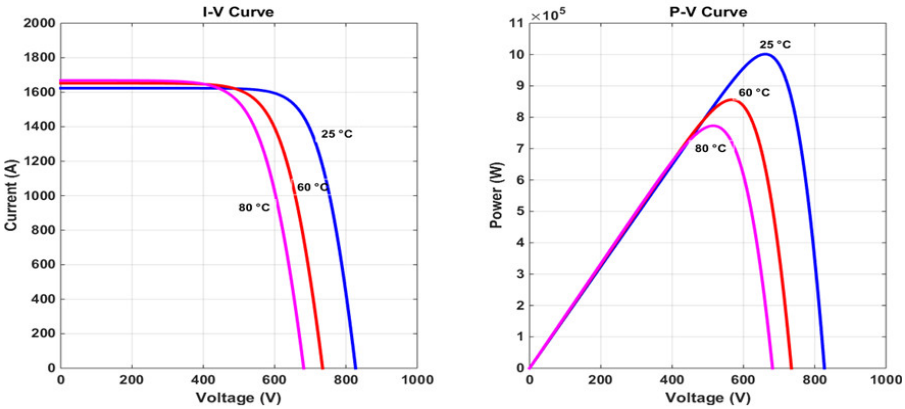

(b) I-V and P-V at various temperatures

Figure 2.12 I-V and P-V curves of the PV array at different condition.

2.4 DC/DC converter

2.4.1 Boost converter

A Boost converter is a circuit that increases a given input voltage to a higher output voltage. Its design is based on four essential parts: an inductor, a semiconductor switch like an IGBT, a diode, and a capacitor. The operation of this converter is managed by a Pulse Width Modulation (PWM) technique. This control method functions by rapidly switching the semiconductor component on and off at a high frequency, known as the switching frequency [67].

In the boost converter of Fig. 2.13, when switch Q is turned on, the input source energizes the inductor while the diode is reverse-biased, preventing current flow to the output. Once the switch is opened, the inductor releases its stored energy, which, together with the input supply, is transferred to the load. The relationship between the input voltage and the output voltage is expressed as follow [30]:

$$V_{dc} = \frac{V_{pv}}{(1-D)} \tag{2.14}$$

Where V_{dc} represents the output voltage of the boost converter, V_{pv} is the output voltage of the PV array, and D denotes the duty cycle, defined as the fraction of time the switch remains ON, with values ranging from 0 to 1.

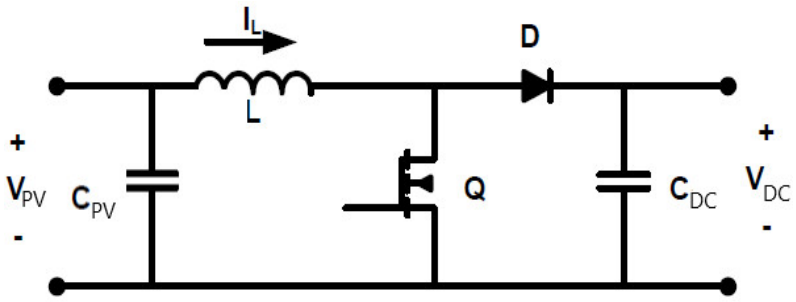

Figure 2.13 The boost converter circuit.

In this research, a DC/DC converter serves as a load adapter to increase the output voltage of the PV array to match the inverter's requirements and to enable maximum power point tracking (MPPT) under different irradiance conditions, as shown in Fig. 2.14. The converter is managed using pulse width modulation (PWM), which functions by switching at a high frequency. The input signals for the PWM are produced by the MPPT technique.

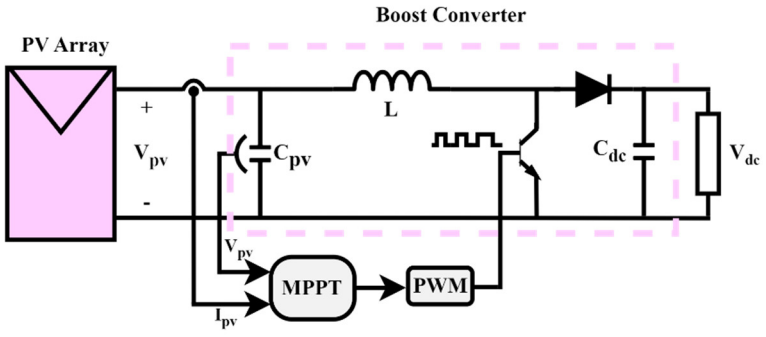

Figure 2.14 Boost Converter in PV System.

2.4.2 Boost converter design

Under continuous current conduction, the following equations are applied to determine the boost converter parameters: the inductance (L), the input capacitor (C_{pv}), and the DC-link capacitor (C_{dc}) [13]:

- The duty cycle D is obtained from Eq. (2.15) :

$$D = 1 - \frac{V_{pv}}{V_{dc}} \tag{2.15}$$

- By assuming that the resistive load R introduces no losses, the PV input power (P_{pv}) is considered equal to the output power (P_{dc}) :

$$R = \frac{{V_{dc}}^2}{P_{dc}} \tag{2.16}$$

- Inductor current is given by :

$$P_{pv} = P_{dc} = \frac{{V_{dc}}^2}{R} \rightarrow I_L = \frac{{V_{dc}}^2}{RV_{pv}} = \frac{V_{dc}}{R(1-D)} \tag{2.17}$$

- The inductance L is calculated based on the allowable current ripple (ΔI_L) flowing through it [68]:

$$\Delta I_L = \frac{DV_{pv}}{f_{sw-boost}L} = \frac{D(1-D)V_{dc}}{f_{sw-boost}L} \leftrightarrow L = \frac{DV_{pv}}{f_{sw-boost}\Delta I_L} \tag{2.18}$$

- For the input capacitor C_{pv} the relation is :

$$C_{pv} = \frac{DV_{dc}}{Rf_{sw-boost}\Delta V_{dc}} \tag{2.19}$$

- The DC-link capacitor (C_{dc}) or decoupling capacitor must be appropriately sized to minimize DC voltage ripple, prevent overvoltages on the DC bus, and mitigate power oscillations that impact the grid current. Its value is calculated using Eq. (2.20), based on the assumption of 100% converter efficiency (i.e., PV power equals the power delivered to the grid) while disregarding converter losses [69]. The procedure for selecting the value of V_{dc} will be discussed in detail in the following chapter.

$$P_{ac} \approx P_{pv} \rightarrow C_{dc} = \frac{P_{ac}}{2\omega V_{dc}\Delta V_{dc}} \tag{2.20}$$

Here, P_{ac} represents the power delivered to the grid, ω denotes the line angular frequency measured in radians per second, and ΔV_{dc} corresponds to the ripple in the DC-link voltage.

$\mathbf{V_{pv}}$	655.6 V	**D**	0.36
$\mathbf{V_{dc}}$	1025 V	**R**	1.050 Ω
$\mathbf{P_{pv}}$	1 MW	$\mathbf{I_L}$	1524 A
$\mathbf{f_{sw\text{-}boost}}$	20 kHz	**L**	78 µH
$\mathbf{\Delta I_L/I_L}$	10%	$\mathbf{C_{pv}}$	343 µF
$\mathbf{\Delta V_{dc}/V_{dc}}$	5%	$\mathbf{C_{dc}}$	30298 µF

Table 2.3 Parameters of the designed boost converter.

2.5 Maximum power point tracking (MPPT) techniques

The I–V and P–V characteristics of a PV array contain a unique maximum power point (MPP), represented by V_{mpp} and I_{mpp}, at which the array generates its maximum power P_{mpp} and operates with the highest efficiency. Due to the nonlinear nature of the I–V curve and its dependence on irradiation and temperature, the MPP changes and must be tracked continuously [30]. A wide range of MPPT techniques have been proposed, differing in terms of complexity, sensor requirements, accuracy, cost, convergence speed, and hardware implementation. Broadly, these methods are classified into three main categories: offline, online, and other MPPT methods [70].

2.5.1 Offline MPPT methods

Offline MPPT control techniques use pre-existing data, such as the I-V and P-V curves of a PV panel, to calculate the MPP voltage and/or current. These methods rely on either mathematical models or lookup tables that are built from empirical data on PV panel characteristics under various environmental conditions (e.g., temperature and solar irradiance) [38]. The MPPT techniques included in this category are as follows:

- **Fractional short-circuit current (FSCC) :** This technique operates on the principle that there is an approximately linear relationship between the short-circuit current (I_{sc}) and the current at the maximum power point (I_{mpp}) of a PV array [71].

$$I_{mpp} = k_1 I_{sc} \tag{2.21}$$

The constant k_1, which is typically between 0.8 and 0.9, is determined empirically.

- **Fractional open-circuit voltage (FOCV) :** Similarly, this technique is based on the linear formula between array voltages, V_{mpp} with its open-circuit voltage V_{oc}. The constant k_2 is between 0.73 and 0.8. Voc is measured by shortly shutting down the power converter [72].

$$V_{mpp} = k_2 V_{oc} \tag{2.22}$$

  The main drawback for both FSCC and FOCV MPPT techniques is that they require periodically interrupting the power output to the load by either disconnecting or shorting the PV array, which results in a temporary power loss and reduced overall efficiency [38].

- **Look-up table (LuT) :** This technique uses precomputed data (typically relating PV voltage, current, temperature, and irradiance to the MPP) stored in a table; the controller simply retrieves the corresponding operating point during operation. The issue with this method is that it requires extensive prior measurement/modeling and becomes inaccurate if environmental conditions deviate from the predefined data [71].

- **Curve fitting** : This offline technique approximates the PV module's I–V or P–V characteristic using a mathematical function (e.g., polynomial or exponential), then analytically determines the maximum power point from that fitted curve. Accuracy strongly depends on the chosen fitting model and parameters. Also, it requires large data storage and computational effort, which slows down tracking speed [73].

2.5.2 Online MPPT methods

In these techniques, the MPP is determined by continuously monitoring the output power of the PV system. Real-time measurements of current and voltage are used for tracking the MPP, and these methods do not rely on prior information provided by the PV panel manufacturer. Among the online algorithms, there are Perturb and observe (P&O), Hill climbing (HC), and Incremental conductance (INC) [55].

- **Perturb & observe (P&O) / Hill climbing (HC):** P&O and HC methods operate on similar principles but differ in their implementation. In Hill Climbing, the perturbation is applied to the duty cycle (D) this is known also as direct control, whereas in P&O, it is applied to the PV array voltage called also indirect control [30]. Modifying the duty ratio influences the current, which in turn affects the voltage. As depicted in Fig. 2.15(a), the P&O method measures both voltage and current, and the MPPT controller establishes a reference voltage. A proportional-integral (PI) regulator compares this reference with the actual PV voltage to generate the PWM signal for the boost converter. Conversely, in the HC algorithm (shown in Fig. 2.15(b)), the regulator is removed, and the duty ratio directly controls the converter [43].

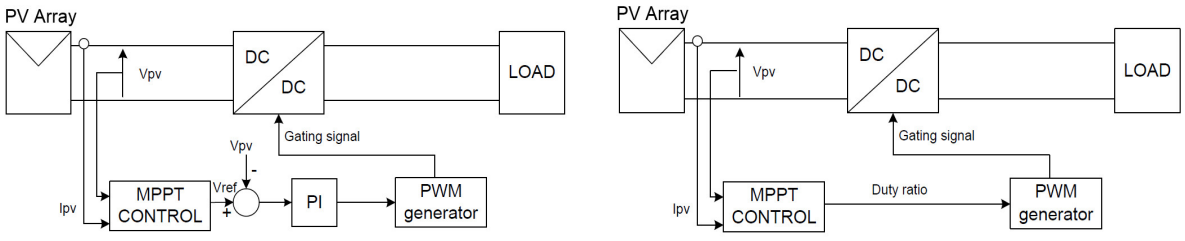

(a) (b)

Figure 2.15 PV system diagram: (a) with P&O, (b) with HC.

To reach the MPP, the operating point of the system is adjusted by introducing a small perturbation. If the perturbation increases the PV power, the same direction is maintained; otherwise, the direction is reversed to converge toward the new MPP. This iterative process continues until the MPP is reached [38].

At steady state, when the MPP is achieved and ΔP/ΔV is nearly zero in both directions, the operating point tends to fluctuate near the MPP. This oscillation can lead to a loss of available energy or potential failure during sudden changes in irradiation. Reducing the perturbation step size can minimize these oscillations, but it also extends the time needed to reach the MPP [74]. The flowcharts illustrating these algorithms are presented in Fig. 2.16.

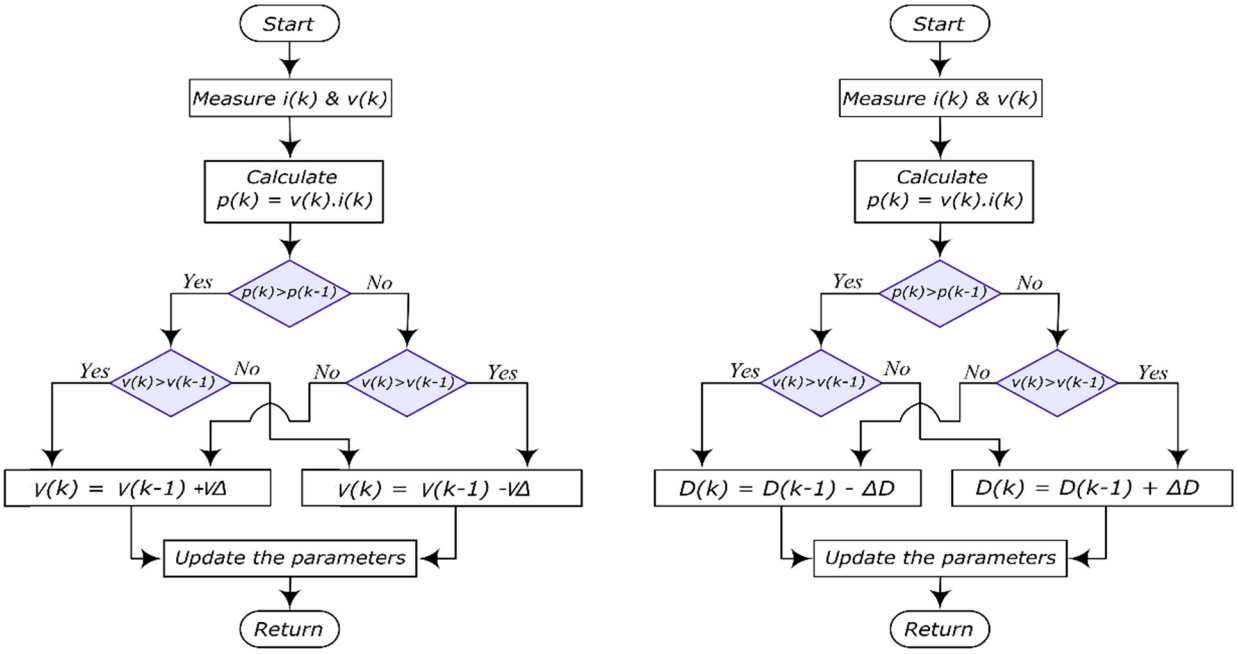

(a) P&O (b) HC

Figure 2.16 P&O and HC flowcharts.

- **Incremental conductance (INC):** This approach relies on the slope of the P–V curve to determine the direction of MPP. The slope is computed using Eq. (2.23), with various cases outlined in Eq. (2.24). By comparing the incremental conductance (di/dv) with the instantaneous conductance (i/v), the duty cycle D is adjusted according to Eq. (2.25), allowing the system to effectively track the MPP [64]. The flowchart of the Incremental Conductance (INC) algorithm is presented in Fig. 2.17.

$$\frac{dp}{dv} = \frac{d(v.i)}{dv} = i + v\frac{di}{dv} \tag{2.23}$$

$$\begin{cases} if \ \dfrac{di}{dv} = -\dfrac{i}{v} & \dfrac{dp}{dv} = 0 & at\ MPP \\ if \ \dfrac{di}{dv} < -\dfrac{i}{v} & \dfrac{dp}{dv} < 0 & right\ of\ MPP \\ if \ \dfrac{di}{dv} > -\dfrac{i}{v} & \dfrac{dp}{dv} > 0 & left\ of\ MPP \end{cases} \tag{2.24}$$

$$D(k) = D(k-1) \pm \Delta D \tag{2.25}$$

Accurate and rapid slope calculations are required, and high sampling rates are necessary to achieve better performance. The selection of a suitable increment size is also important. Larger increments enable faster tracking of the MPP, but they may cause the system to oscillate around it [64, 74].

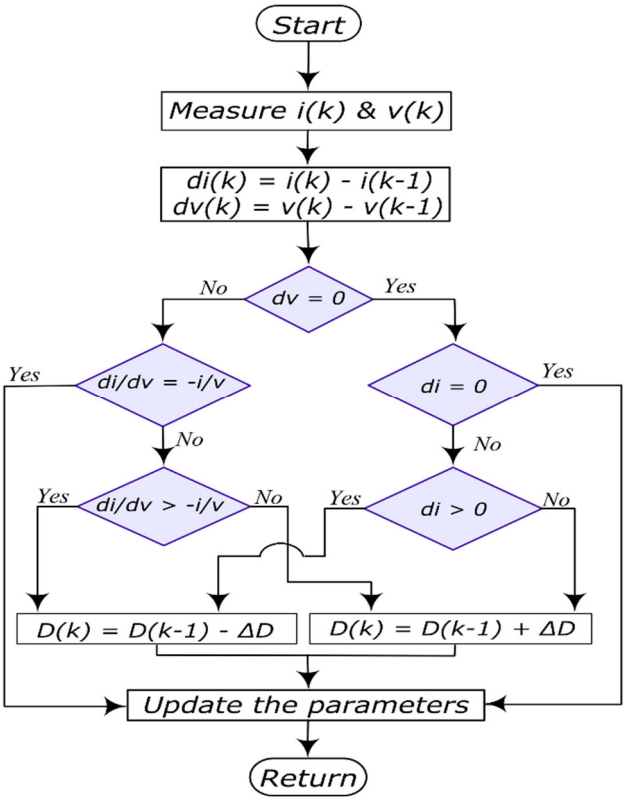

Figure 2.17 Flowchart of INC algorithm.

2.5.3 Other MPPT methods

These techniques known also as training-based MPPT combine intelligent control, optimization techniques, or hybrid strategies to overcome the limitations of offline and online methods. These approaches often rely on artificial intelligence (AI) tools such as Fuzzy Logic Control (FLC), Neural Networks (NNs), and optimization algorithms like Particle Swarm Optimization (PSO). In addition, hybrid techniques integrate the strengths of two or more algorithms, for example, combining INC with AI or P&O with fuzzy logic, to enhance accuracy and convergence speed. Such methods are particularly effective under rapidly changing environmental conditions and in complex scenarios like partial shading, where traditional algorithms may fail to track the global maximum power point. Although these approaches deliver high accuracy, adaptability, and robustness, they usually come with higher computational requirements, more complex implementation, and in the case of AI-based systems, the need for extensive training data [73, 75].

2.6 Simulation of boost converter and MPPT control

In order to evaluate the performance of the designed boost converter and to select a suitable MPPT control algorithm for the studied system among online MPPT techniques (details are given in Appendix B), a simulation test is carried out on the 1 MW PV array connected to a non-optimal load (R = 1.050 Ω).

The system is tested under two possible scenarios that replicate real-life phenomena observed in PV plants:

- **Cloud cover at t = 0.4 s** : This occurs when a cloud moves across the sun and partially or fully obscures it, causing a sudden drop in solar irradiance.

- **Cloud-edge effect at t = 0.7 s :** When the edge of a cloud passes near the sun, it can act like a lens. Scattering and reflection at the cloud boundary locally concentrate solar irradiance for a short duration. As a result, the PV array may receive irradiance levels higher than the standard peak of 1000 W/m²—often reaching 1050–1300 W/m² for a few seconds, depending on the cloud's shape and thickness [76].

In both scenarios, the PV module temperature is assumed constant because of its thermal inertia, meaning it does not change significantly over fractions of a second. Table 2.4 summarizes the conditions of the two scenarios.

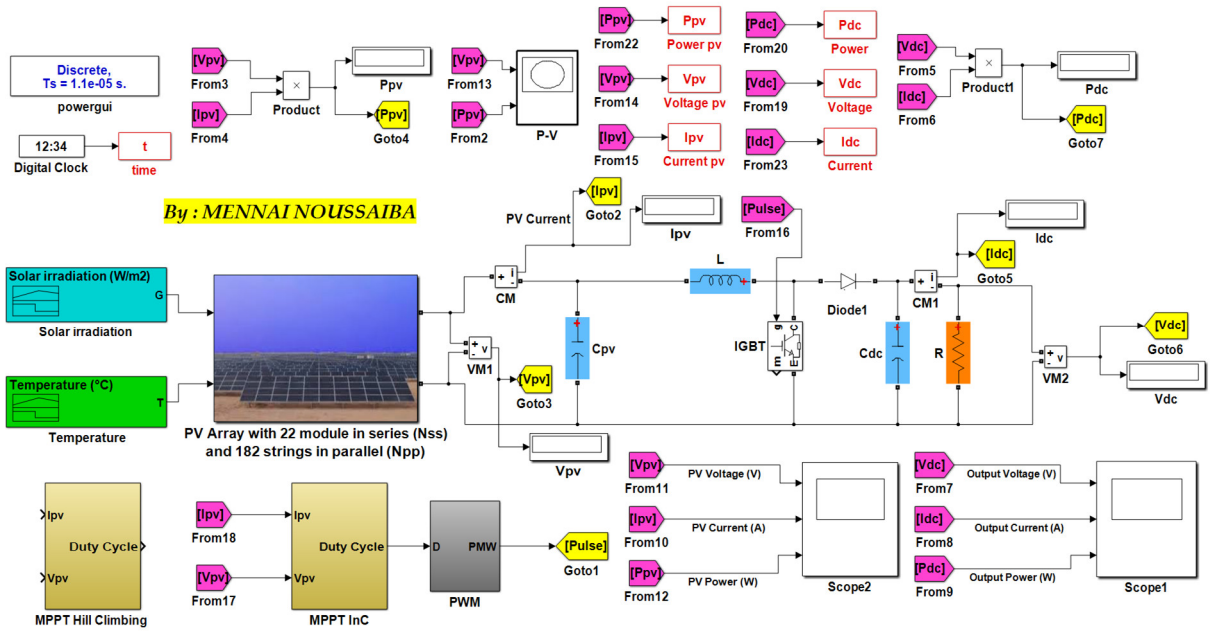

Figure 2.18 Simulink model (DC stage) to Test MPPT Algorithm.

Time (s)	G (W/m²)	T (°C)	Meaning
0.0-0.4	900	25	Clear-sky irradiance
0.4-0.7	600	25	Cloud cover : irradiance drops
0.7-1.0	1150	25	Cloud-edge enhancement: irradiance temporarily exceeds clear-sky level.
1.0-1.4	900	25	Return to clear-sky condition: Cloud passes

Table 2.4 Simulation scenarios.

Fig. 2.19 illustrates the test results of the INC-based MPPT and HC-based MPPT controllers under the cloud-cover and cloud-edge scenarios. As shown in Fig. 2.19(c), both controllers regulate the duty cycle of the DC/DC converter to continuously drive the PV array operating point toward the MPP. Furthermore, the boosting action of the converter is evident in Fig. 2.19(a): when the duty ratio D increases, the output voltage V_{dc} rises accordingly, and when D decreases, V_{dc} drops.

By comparing the power plots in Fig. 2.19(b) and the results summarized in Table 2.5, it can be observed that although both methods successfully detected the power step-down (due to cloud cover) and the step-up (due to the cloud-edge effect), and were able to track the new MPPs, the INC algorithm demonstrated a faster and more accurate response than the HC method. The HC controller reacted earlier at t = 0.4 s and t = 1 s; however, it introduced large power oscillations in steady state, ranging between 11.2 kW and 27 kW, and failed to converge within ±2% of the theoretical MPP. Consequently, its tracking efficiency was relatively low, in the range of 95.8–96.85%, compared to the 98.99–99.10% efficiency achieved by the INC controller.

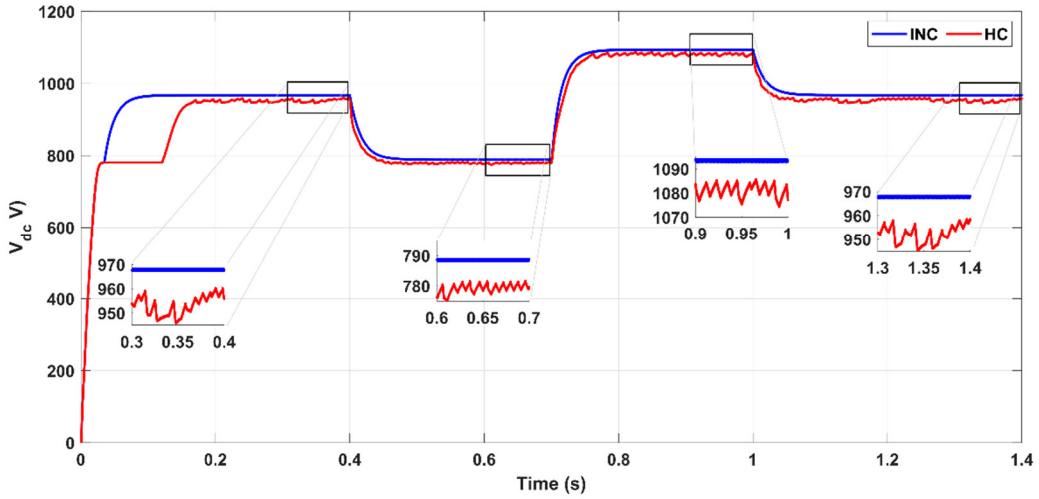

(a)

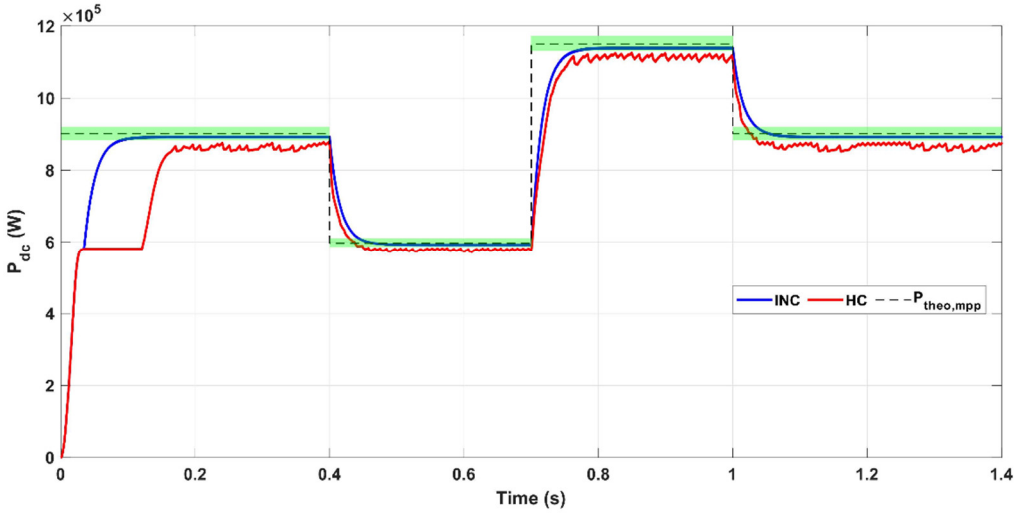

(b)

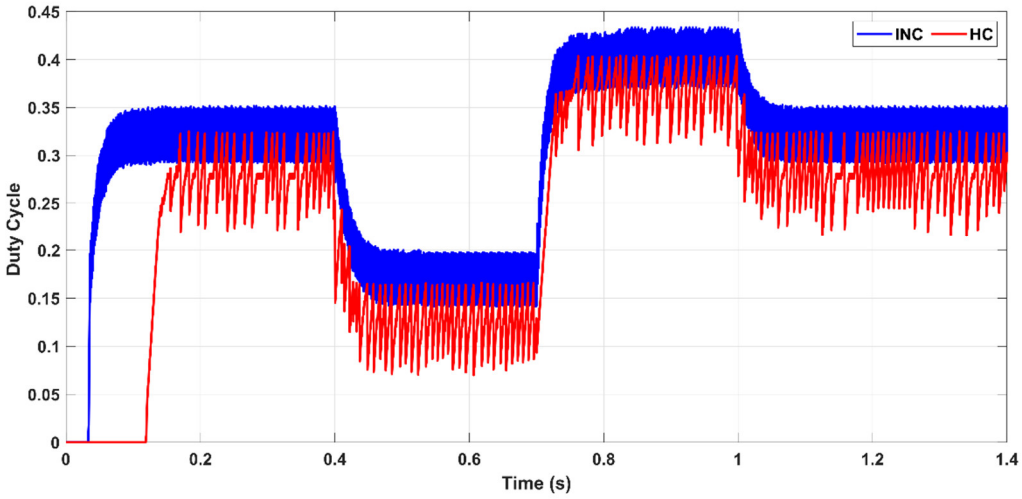

(c)

Figure 2.19 Test results of INC and HC algorithms .

MPPT		**HC**	**INC**
900 W/m^2 & 25°C	**T_s (ms)**	∞	90.37
	ΔP (kW)	26.1	1.7
	Efficiency (%)	95.8	98.99
600 W/m^2 & 25°C (Cloud cover)	**T_s (ms)**	∞	44.6
	ΔP (kW)	11.2	1
	Efficiency (%)	96.8	99.10
1150 W/m^2 & 25°C (Cloud-edge spike)	**T_s (ms)**	∞	61.4
	ΔP (kW)	27	3
	Efficiency (%)	96.85	99.01
900 W/m^2 & 25°C	**T_s (ms)**	∞	36
	ΔP (kW)	26.6	1.7
	Efficiency (%)	95.97	98.99

Table 2.5 Comparaison of HC and INC MPPT results at different scenarios.

2.7 Conclusion

In this chapter, the Simulink models of the DC stage components of the grid-connected PV system were developed and tested. After presenting the principle of the PV generator and the different mathematical models, the one-diode model was selected, as it is simple and accurately represents the static behavior of the PV module.

The mathematical equations describing the parameters of this model as a function of irradiance and temperature were introduced, enabling the simulation of the PV array in MATLAB/Simulink. An iterative method for adjusting R_s and R_p was applied to determine the resistance values of the YL250P-29b module used in the Oued El Kebrit PV plant.

To extract the maximum power from the 1 MW PV array, a boost converter was designed. For selecting the MPPT controller, two methods—Hill Climbing and Incremental Conductance—were tested under two possible scenarios that reflect real-life operating conditions of PV plants. The comparative simulation results revealed that the Incremental Conductance algorithm tracks sudden changes in irradiance more rapidly, accurately, and efficiently than the Hill Climbing method. Therefore, the Incremental Conductance (INC) MPPT technique is adopted for implementation in this study.

Chapter III

AC-Side Control Strategy for Grid-Connected PV Systems

3.1 Introduction

Under normal grid conditions, grid-connected PV systems require two primary control objectives: maximum power point tracking (MPPT) of the PV array, as discussed in Chapter II, and precise current feed-in for the inverter stage. This chapter addresses the second stage of the PV system, focusing on the inverter and its associated power conditioning elements for grid integration.

A comprehensive design methodology is presented, including DC-link voltage selection, operation of the two-level voltage source inverter (2L-VSI) under sinusoidal pulse width modulation (SPWM), LCL filter design, phase-locked loop (PLL) implementation, transmission line modeling, and the overall inverter control strategy. The adopted dual-loop control structure consists of an inner current loop and an outer DC-link voltage loop, both tuned using the symmetrical optimum method to ensure stable operation, accurate current tracking, and compliance with grid power quality standards specified by IEEE and EN regulations.

To validate the theoretical developments, each component is modeled in MATLAB/Simulink using actual parameters from the Oued El Kebrit PV plant in Algeria.

3.2 Criteria for selecting DC-link voltage

In a grid-connected photovoltaic (PV) system, the DC-link voltage is managed through an outer control loop that responds to deviations in the DC voltage. For systems that apply verctor current control (VCC), this loop generates the reference currents for the grid. Choosing appropriate values for the DC-link reference voltage and the capacitor is essential to ensure the stable operation of the voltage source inverter (VSI). The reference voltage of the DC-link must be sufficiently high to enable three-phase PWM operation, while also considering switching and filter losses that reduce the effective voltage [68, 77].

When the voltage source inverter (VSI) is connected to the grid without pulse width modulation (PWM) control, the DC-link capacitor charges naturally through the anti-parallel diodes of the switching devices. This uncontrolled DC-link voltage serves as the basis for determining the reference DC-link voltage. As noted in [78] and [79], the reference DC-link voltage should be around 10–15% higher than the naturally charged value, which is approximately twice the peak of the grid phase voltage. It is important to note that controlling the current flow is possible only when V_{dc} is higher than the combined value of the grid's peak voltage and the voltage drop between the grid and the inverter.

In the studied system, the phase RMS grid voltage is 315 V, resulting in an uncontrolled DC-link voltage of 891 V. By applying a 15% design margin, the chosen reference DC-link voltage for the sinusoidal PWM (SPWM) VSI system is: 1025 V.

An alternative approach for determining the DC-link voltage in an SPWM-based VSI is expressed as:

$$V_{dc} = \frac{2\sqrt{2}V_{LL}}{m_a\sqrt{3}} \tag{3.1}$$

Where V_{LL} represents the phase RMS grid voltage and m_a is the amplitude modulation index. For the system under consideration, ma is equal to 0.5.

3.3 DC/AC converter

The inverter plays a central role in any direct current (DC) renewable energy system, as it converts DC power into alternating current (AC) that aligns with the grid's voltage, frequency, and phase [80]. In PV systems, the DC output from the solar array must be converted before it can be delivered to the AC grid or used by most electrical devices. This conversion is carried out using the inverter's switching process, which produces AC by rapidly opening and closing the circuit. Afterward, a step-up transformer increases the voltage to the level required by the grid [57].

3.3.1 Classification of inverters

Inverters can be categorized based on their output waveform or circuit configuration [81, 82]:

a. Based on output waveform

- **Square wave inverter** – Produces a simple square-shaped AC waveform. This type is rarely used in modern applications because it causes high harmonic distortion.
- **Modified square wave (or quasi-sine wave) inverter** – Generates a stepped approximation of a sine wave, offering better compatibility with many electrical loads compared to the pure square wave.
- **Pure sine wave inverter** – Produces a sinusoidal waveform similar to that of the utility grid, making it suitable for sensitive and precision equipment.

b. Based on circuit topology

- **Voltage source inverter (VSI):**

- Operates with a fixed DC voltage source at the input.
- Provides direct control of the output AC voltage.
- Can be implemented in half-bridge or full-bridge configurations.
- Available in both two-level and multilevel designs.

- **Current source inverter (CSI):**
  - Operates with a fixed DC current source at the input.
  - Controls the AC output current waveform.
  - Maintains nearly constant input current, usually with the help of a large inductor.

- **Multilevel inverter (MLI):**
  - Developed to meet the demand for medium- and high-power applications.
  - Reduces harmonic distortion, making it well-suited for renewable energy integration.
  - Its Common configurations include: diode-clamped (neutral point clamped, NPC), flying capacitor (FC), and cascaded H-bridge (CHB).

3.3.2 PV inverters topologies

Inverters used in PV applications are power-dependent devices, with modern models achieving peak efficiencies of up to 98.5%. Grid-connected PV inverters are typically classified into four main configurations [17]:

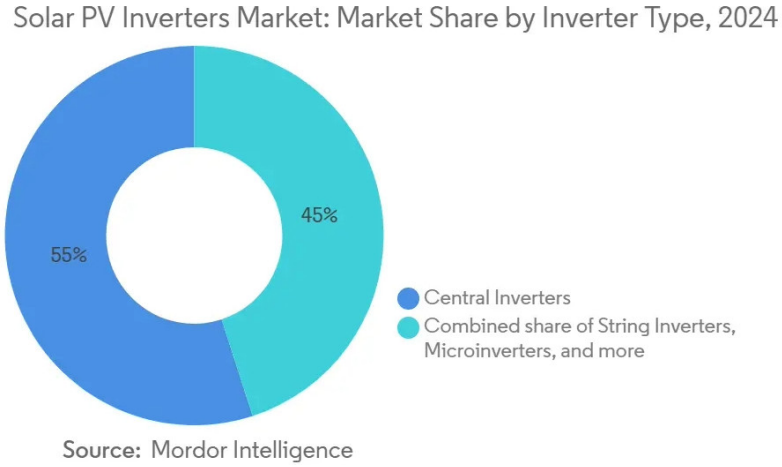

Figure 3.1 Global PV inverter market share in by type in 2023.

As shown in the recent market report in Fig. 3.1, central inverters and string inverters together represent the largest portion of the global PV inverter market, with their market shares remaining relatively similar.

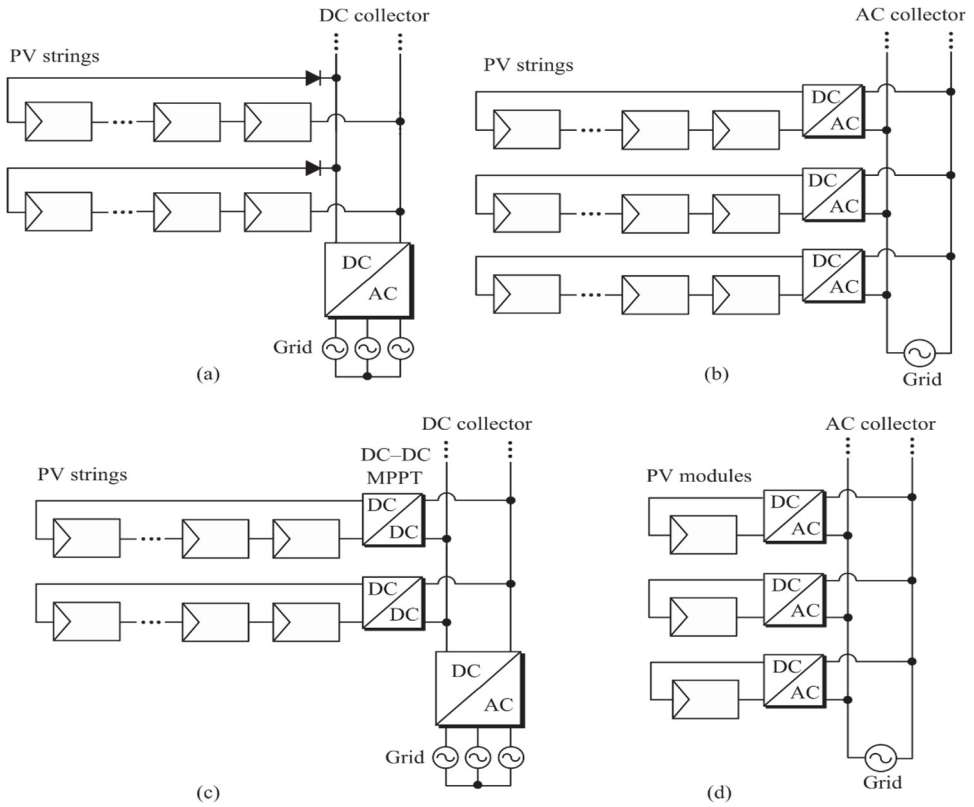

Figure 3.2 Grid-connected PV inverter topologies: (a) central inverter, (b) string inverter, (c) multi-string inverter and (d) AC-module (micro-inverter).

- **Central inverter (~0.1 – 5+ MW):** this topology uses a single three-phase voltage source inverter (VSI) to connect an entire PV plant as depicted in Fig. 3.2(a), with strings of modules in series and parallel to match inverter ratings. Its advantages include simplicity, a single transformer, and centralized control, but it suffers from reduced energy yield due to a centralized maximum power point tracker (CMPPT) and additional diode losses. Despite this, it remains the dominant choice for large-scale PV, usually operating with three-phase connections [82].
- **String inverter (~1 – 10+ kW):** it employ one inverter per string as seen in Fig. 3.2(b), eliminating the need for blocking diodes and enabling distributed maximum power point tracker (DMPPT). This improves energy yield, mitigates mismatch and shading losses at the string level, and enhances modularity, though at higher investment cost and component count compared to central inverters. It is used in small- and medium-scale PV systems [38].
- **Multi-string inverter (~2 – 350 kW):** this topology combines aspects of both systems. Each string is connected to a central inverter via its own DC/DC converter, allowing a DMPPT and higher modularity while retaining centralized grid-side control. However, this comes with added DC cabling losses [83].

- **AC-module or micro-inverter (~50 – 500 W):** it push distribution further by integrating an inverter into each module. This achieves the best MPPT performance and minimizes mismatch losses but at the cost of higher price, lower overall efficiency, and greater component distribution. They are mainly suited for small-scale and residential PV systems [84].

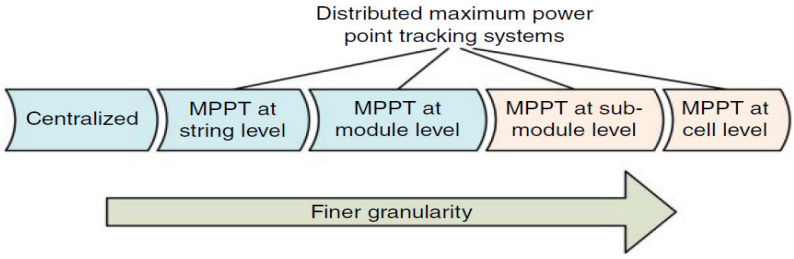

Figure 3.3 Development trend of DMPPT systems.

As indicated in Fig. 3.3, the overall industry trend is shifting from centralized MPPT to distributed MPPT, as finer-level tracking increases solar yield under mismatch or shading. While DMPPT at the string and module levels is already commercial, sub-module and cell-level solutions remain under development [85]. The industrial structure of the four configurations is shown in Fig. 3.4 [86].

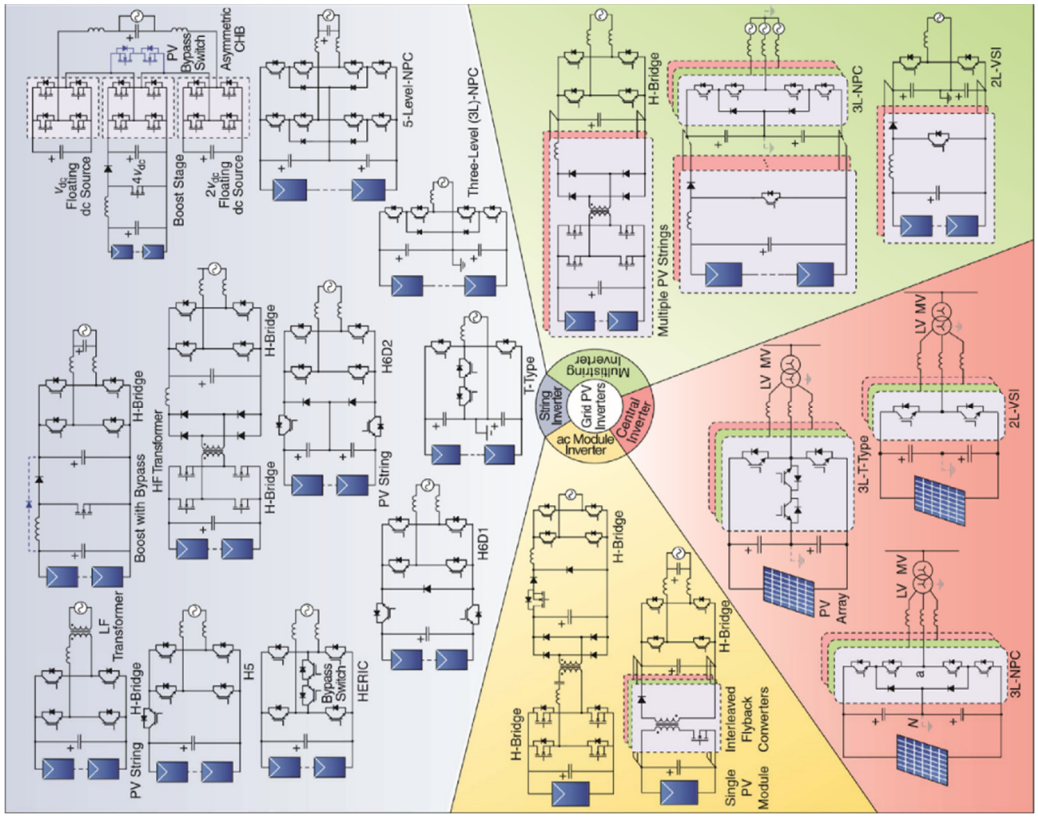

Figure 3.4 Classification of industrial inverter topologies [86].

Large-scale PV systems frequently employ central topology because of its low-frequency transformer and single control unit [6, 17]. At the Oued El Kebrit PV plant, there are 15 TBEA TC1000KS 1 MW central inverters (see Appendix C). Each inverter is an outdoor box-type unit consisting of two identical compartments, each rated at 500 kW. They also include grid connection equipment and digital devices for controlling and monitoring the array parameters, as shown in Fig. 3.5(b).

(a) outdoor box-type inverter (b) monitoring screen

Figure 3.5 TBEA TC1000KS 1MW central inverter installed in SKTM oued el kebrit PV plant (photos by author).

As classified by [86] in Fig. 3.4, central inverters may be designed as three-level T-type (3L-T-type), three-level neutral point clamped (3L-NPC), or two-level voltage source inverters (2L-VSI). In this thesis, the 2L-VSI topology is selected to model the TC1000KS.

In grid-connected PV systems, the inverter must regulate the current from the PV modules and control the power injected into the grid in compliance with standards. Key design specifications include nominal power, nominal voltage, maximum DC-link voltage, and inverter control. Effective inverter modeling also requires accurate power regulation, flexible power factor control, minimization of harmonic distortion, and complete suppression of any DC component in the grid-injected current [87, 88].

3.3.3 Modeling of the SPWM-based 2L-VSI

In this study, the power stage is modeled using a 2L-VSI, which converts the 1025 V DC output from the boost converter into a 315 V, 50 Hz AC signal. The three-phase full-bridge configuration, illustrated in Fig. 3.6(a), is composed of six switching devices, arranged with two on each leg. In the Simulink implementation (Fig. 3.6(b)), insulated-gate bipolar transistors (IGBTs) with antiparallel diodes are utilized. These diodes, also referred to as freewheeling or feedback diodes, allow the inductive current to flow.

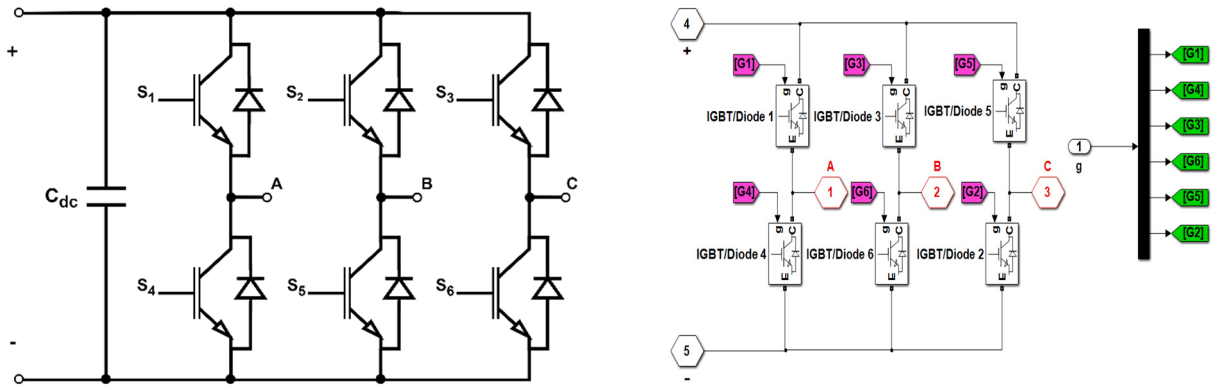

(a) (b)

Figure 3.6 2L-VSI : (a) structure and (b) simulink model.

Six gating signals are required to control the inverter switches. The waveforms of signals H1, H3, and H5 are presented in Fig. 3.7. These signals represent three-phase symmetrical switching with a 120° phase shift, ensuring balanced three-phase voltages. Within each phase leg, the switches operate in a complementary manner to prevent short-circuiting of the DC-link capacitor. As a result, the output voltage attains the same magnitude as the DC-link voltage [89].

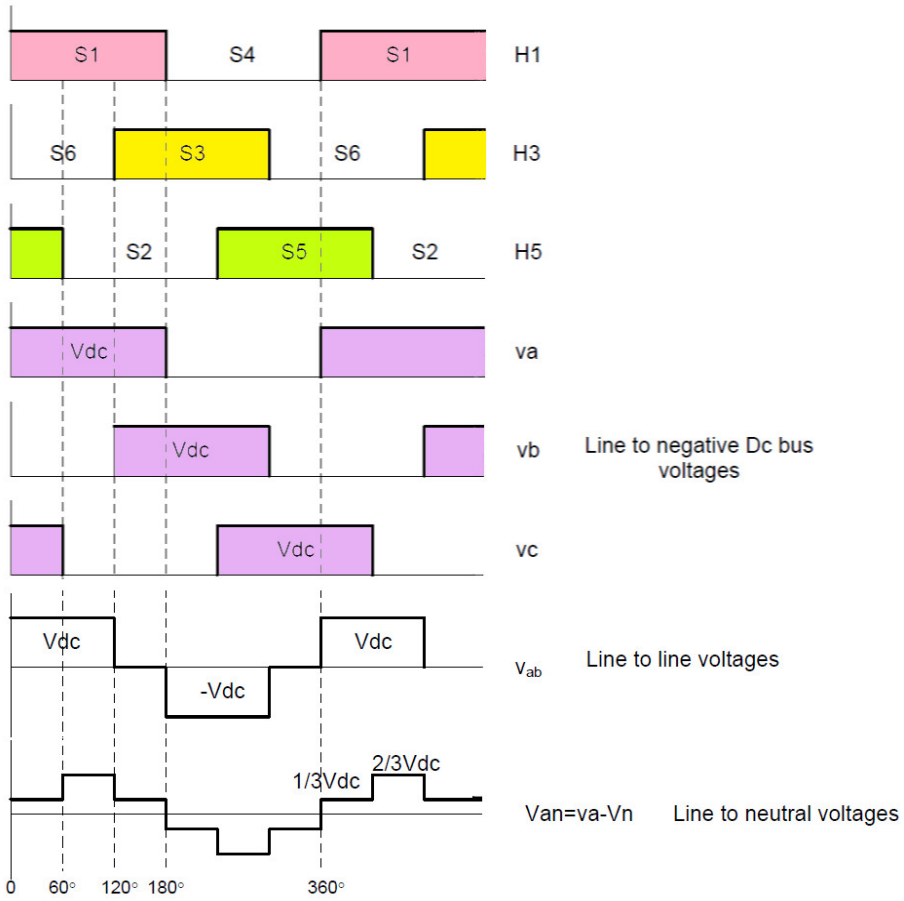

Figure 3.7 Waveforms of the switching functions and output voltages.

The inverter is represented by assigning a logic function F to each phase leg, which specifies its conduction states as summarized in Table 3.1. Using this function, the corresponding inverter line voltages can be expressed as follows:

$$\begin{cases} V_{ab} = V_{dc}\left(F1 - F2\right) \\ V_{bc} = V_{dc}\left(F2 - F3\right) \\ V_{ca} = V_{dc}\left(F3 - F1\right) \end{cases} \tag{3.2}$$

For a balanced load:

$$V_{an} + V_{bn} + V_{cn} = 0 \tag{3.3}$$

Using Eqs. (3.2) and (3.3), the phase to neutral voltages of the inverter are found by the following equations:

F1 = 1	F1 = 0
S1 closed and S4 open	S4 closed and S1 open
F2 = 1	F2 = 0
S2 closed and S5 open	S5 closed and S2 open
F3 = 1	F3 = 0
S3 closed and S6 open	S6 closed and S3 open

Table 3.1 Logic functions assigned to the inverter legs

Finally, the matrix below represents the mathematical model of the 2L-VSI in terms of phase-to-neutral voltages [90]:

$$\begin{bmatrix} V_{an} \\ V_{bn} \\ V_{cn} \end{bmatrix} = \frac{V_{dc}}{3} \begin{bmatrix} 2 & -1 & -1 \\ -1 & 2 & -1 \\ -1 & -1 & 2 \end{bmatrix} \begin{bmatrix} F1 \\ F2 \\ F3 \end{bmatrix} \tag{3.4}$$

Due to its simplicity, the SPWM (sinusoidal pulse width modulation) approach is utilized to generate gate signals for the IGBTs. It provides control over the three-phase output voltage in terms of amplitude and frequency [91]. As shown in Fig. 3.8, a 10 kHz triangular carrier is compared with three sinusoidal reference signals shifted by 120° for each phase, defining the switching states of each leg. These reference signals are supplied by the VSI controllers, which include outer and inner loops, further explained in Section 3.5. The operating principle of this technique is summarized in the table below:

	$V_{a,ref} > Vc_{arrier}$	$V_{a,ref} < V_{carrier}$
S1	ON	OFF
S4	OFF	ON
	$V_{b,ref} > V_{carrier}$	$V_{b,ref} < V_{carrier}$
S3	ON	OFF
S6	OFF	ON
	$V_{c,ref} > V_{carrier}$	$V_{c,ref} < V_{carrier}$
S5	ON	OFF
S2	OFF	ON

Table 3.2 SPWM principle.

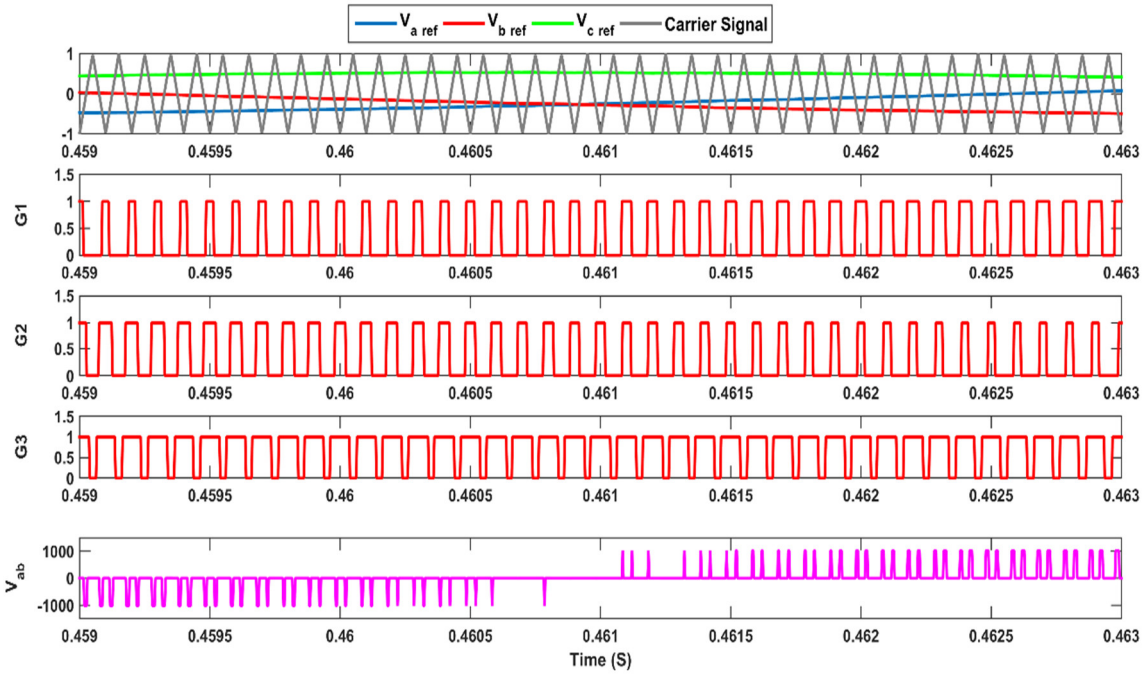

Figure 3.8 SPWM signals and output voltage waveforms.

The observed line-to-line voltage waveform V_{ab} in Fig. 3.8 highlights the necessity of filtering to achieve pure sinusoidal output voltages.

In the SPWM-based 2L-VSI, two important parameters are the amplitude modulation index (m_a) and the frequency modulation index (m_f). The amplitude modulation index is defined as the ratio of the peak amplitude of the sinusoidal reference wave ($V_{m,ref}$) to that of the triangular carrier wave ($V_{carrier}$). It is defined that the frequency modulation index equals the carrier frequency (f_c) divided by the modulating frequency (f_m) [92]. In the present system, f_c=10 kHz and f_m=50 Hz (grid frequency), resulting in m_f=200. This indicates that switching harmonics occur near the 200th harmonic and its multiples.

$$m_a = \frac{V_{m,ref}}{V_{carrier}} \tag{3.5}$$

$$m_f = \frac{f_c}{f_m} \tag{3.6}$$

3.4 Harmonic mitigation

To supply the grid with a sinusoidal line current and voltage, the connection between the grid and the inverter is provided through low-pass filters, which attenuate harmonics caused by high-frequency switching. The total harmonic distortion (THD) is defined for voltage or current as the ratio of the root-sum-square of the harmonic components to the RMS value of the fundamental frequency, multiplied by 100% [93]:

$$THD_i = \frac{\sqrt{\sum_{h=2}^{h} I_h^2}}{I_1} \tag{3.7}$$

$$THD_v = \frac{\sqrt{\sum_{h=2}^{h} V_h^2}}{V_1} \tag{3.8}$$

Here, (I_1, V_1) and (I_h, V_h) are the RMS values of the fundamental frequency and the h-th harmonic (h=2,3,4,…), respectively

3.4.1 Grid filter topologies

In grid-connected PV systems, three filter types are commonly used: L, LC, and LCL (Fig. 3.9). Studies in [94] examine these topologies in terms of design considerations, system dynamics, harmonic suppression, and decoupling from grid impedance, with particular emphasis on the strengths and drawbacks of the LCL filter.

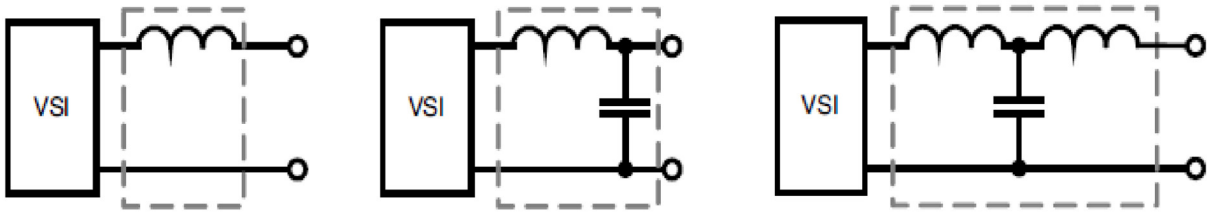

(a) (b) (c)

Figure 3.9 Filter configuations: (a) L-filter, (b) LC-filter, and (c) LCL-filter.

In an L-filter, sufficient harmonic attenuation requires a high switching frequency; however, this is often impractical in high-power applications. At lower switching frequencies, a large inductor is needed, which causes significant voltage drops and degrades system dynamics. Compared to

the L-filter, the LC-filter provides better attenuation, but it requires a relatively large capacitance to reduce losses. This, however, can lead to inrush currents and introduces a resonant frequency that depends on the grid impedance, which varies over time. For these reasons, LC-filters are generally unsuitable for grid-connected applications [95].

In contrast, the LCL-filter achieves lower THD with components of similar size and offers better decoupling from grid parameters. Its advantages include reduced reactive power, compatibility with low switching frequencies, and suitability for high-power applications [38, 94]. Although LCL-filters may be more expensive than simpler topologies shown in Fig. 3.9, their limited dependence on grid impedance makes them highly effective. A drawback, however, is the resonance that can cause current distortion and instability in both dynamic and steady states [96]. To mitigate this issue, passive damping is typically applied by inserting a resistor either in series or parallel with the inverter-side inductor or the filter capacitor [97].

Given its performance benefits, the LCL-filter is selected in this thesis as the most suitable option for grid-connected VSI systems. Here, a damping resistor is placed in series with the filter capacitor. The design steps for the PV-grid connection filter are presented in the following section.

3.4.2 LCL filter design methodology

In this study, passive damping is achieved by adding a series resistor (R_d) to the filter capacitor, which suppresses LCL resonance while keeping fundamental frequency losses low [98]. For the LCL filter at the 2L-VSI output, L_i, L_g, C_f, and R_d are identical in all phases; thus, the equivalent circuit in Fig. 3.10(a) applies to the other two phases as well [99].

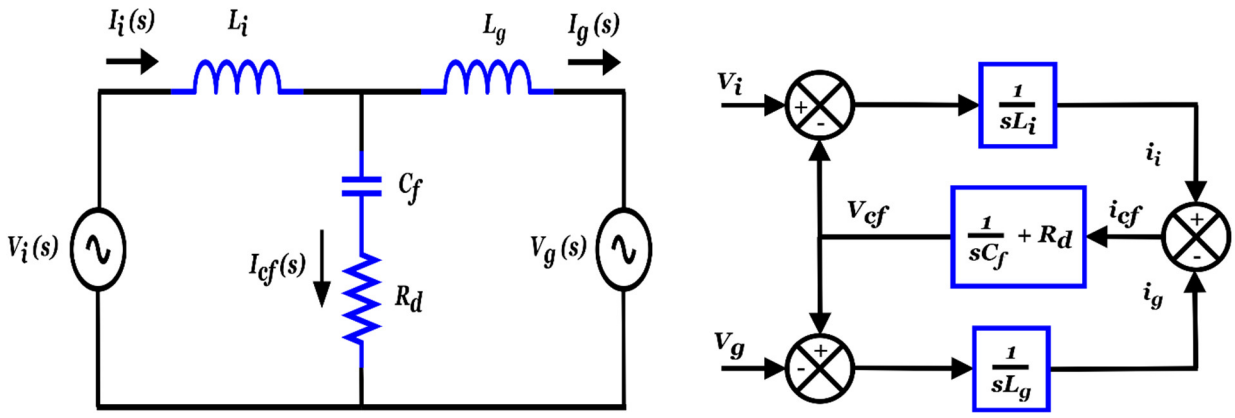

(a) equivalent circuit (b) block duagram

Figure 3.10 Passive damped LCL-filter.

$$\begin{cases} i_i - i_{cf} - i_g = 0 \\ V_i - V_{cf} = i_i s L_i \\ V_{cf} - V_g = i_i s L_g \\ V_{cf} = i_{cf}\left(\dfrac{1}{sC_f} + R_d\right) \end{cases} \tag{3.9}$$

The filter's mathematical model in the s-domain is derived from the given equations. To determine the transfer function $H_{LCL}(s)$, the grid voltage V_g is treated as an ideal source. For analysis purposes, V_g is set to zero since the grid acts as a short circuit at harmonic frequencies. Accordingly, the transfer function can be expressed as [100]:

$$H_{LCL}(s) = \frac{i_i(s)}{V_g(s)} = \frac{sC_f R_d + 1}{s^3 C_f L_i L_g + s^2 C_f R_d (L_i + L_g) + s(L_i + L_g)} \tag{3.10}$$

The LCL filter for the system under study was designed using a MATLAB program that follows the algorithm shown in Fig. 3.11. The main input parameters used in the design include the rated power (S_{rated} or P_{rated}), DC-link voltage (V_{dc}), grid frequency (f_g), line-to-line grid voltage (V_{LL}), and switching frequency of the VSI ($f_{sw\text{-}vsi}$).

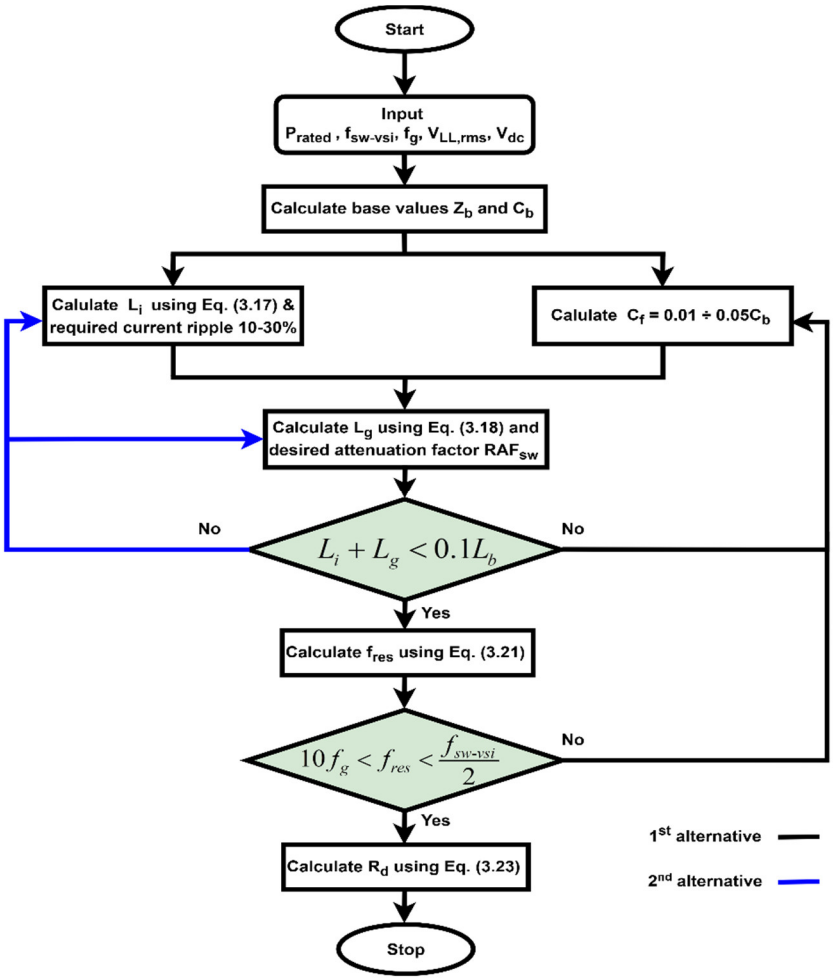

Figure 3.11 LCL-filter design flowchart.

To meet IEEE standards (explained in the next section), the filter must sufficiently suppress harmonic components, ensuring THD compliance. This requires two conditions: the resonance frequency must lie within the range defined in Eq. (3.22), and the total filter inductance must remain below 0.1 pu to limit AC voltage drop, as stated in Eq. (3.20) [21, 101].

- The base impedance Z_b and base capacitance C_b are calculated using the following equations:

$$V_{LL,rms} = \sqrt{3}V_{ph} \tag{3.11}$$

$$Z_b = \frac{V_{LL,rms}^2}{\mathrm{P}_{rated}} \tag{3.12}$$

$$C_b = \frac{1}{2\pi f_g Z_b} \tag{3.13}$$

- C_f is set based on the permissible reactive power absorption, typically limited to 1–5% of C_b, to maintain a power factor between 0.95 and 1.

$$C_f = xC_b \tag{3.14}$$

- L_i, used to reduce current ripple, is usually sized to carry 10–30% of the maximum current.

$$I_b = \frac{\mathrm{P}_{rated}}{\sqrt{3}V_{LL,rms}} \tag{3.15}$$

$$\Delta \mathrm{I}_{b,max} = \%15 I_{b,\max} \tag{3.16}$$

$$L_i = \frac{V_{dc}}{8 f_{sw-vsi} \Delta I_{b,\max}} \tag{3.17}$$

- The value of L_g is selected based on the required Ripple Attenuation Factor RAF_{sw} to suppress high-frequency switching harmonics.

$$L_g = \frac{RAF_{sw} + 1}{RAF_{sw}(2\pi f_{sw-vsi})^2 C_f} \tag{3.18}$$

$$L_b = \frac{Z_b}{2\pi f_g} \tag{3.19}$$

$$L_i + L_g < 0.1 L_b \tag{3.20}$$

$$f_{res} = \frac{1}{2\pi}\sqrt{\frac{L_i + L_g}{L_i L_g C_f}} \tag{3.21}$$

$$10 f_g < f_{res} < \frac{f_{sw-vsi}}{2} \tag{3.22}$$

$$R_d = \frac{1}{3(2\pi f_{res})C_f} \tag{3.23}$$

Input parameters	
$\mathbf{P_{rated}}$	1 MW
$\mathbf{f_{sw\text{-}vsi}}$	10 kHz
$\mathbf{f_g}$	50 Hz
$\mathbf{V_{ph}}$	315 V
x	2.5 %
$\mathbf{\Delta I_{b,max}/I_{b,max}}$	15 %
$\mathbf{RAf_{sw}}$	20 %
Designed filter parameters	
$\mathbf{L_i}$	80.719 µH
$\mathbf{L_g}$	5.6852 µH
$\mathbf{C_f}$	267.33 µF
$\mathbf{R_d}$	0.055 Ω
$\mathbf{f_{res}}$	4.22 kHz

Table 3.3 Designed filter parameters

Fig. 3.12 shows the Bode plots of the designed filter transfer function in Eq. (3.10) both with and without R_d, demonstrating the role of the resistor in reducing filter resonance.

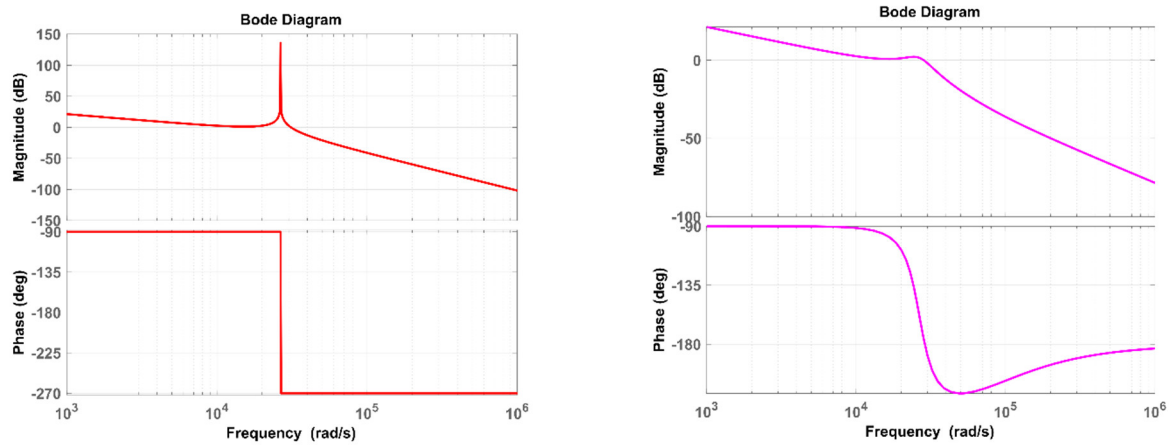

(a) without R_d (b) with R_d

Figure 3.12 Bode diagrams of the designed LCL filter.

3.4.3 Grid interconnection and power quality standards

Connecting PV systems to the utility grid requires compliance with interconnection and power quality standards to maintain safety and reliability. These standards specify allowable limits for harmonic distortion, power factor, and frequency regulation at the point of common coupling (PCC).

IEEE 929–2000: This standard provides recommended practices for the interconnection of PV systems with electric power systems, focusing on safety, performance, and power quality requirements [102].

- **Clause 4.4 – Harmonic Distortion:**

  The PV system output must maintain low current distortion to prevent negative impacts on other grid-connected equipment. At the PCC, the requirements are:

  - Total harmonic current distortion (THD_i) ≤ 5% of the fundamental current at rated inverter output.
  - Each individual harmonic must meet the limits specified in Clause 10.4 of IEEE 519–1992.

- **Clause 4.5 – Power Factor:**

  Grid-connected PV systems should operate with a power factor close to unity, typically ≥ 0.85 (lagging or leading), to reduce reactive power exchange.

IEEE 519–1992 : This standard establishes detailed limits for harmonic distortion at the PCC [103].

- **Voltage Distortion (Clause 11.5):**

  Limits depend on the nominal system voltage. For this study (system voltage of 31.5 kV), only the relevant case is considered, and corresponding values are summarized in Table 3.4.

Bus voltage V at PCC	Individual harmonic distortion (%)	THD (%)
1 kV < V ≤ 69 kV	3.0	5.00

Table 3.4 Voltage distortion limits specified by IEEE 519-1992 [103].

- **Current Distortion (Clause 10.4):**

  Limits are defined according to the ratio of short-circuit current (I_{sc}) to maximum demand load current (I_L). The standard introduces Total Demand Distortion (TDD), applicable only to current. Unlike THD, which is normalized by the fundamental current (I_1), TDD is normalized by the maximum demand current (I_L) as mentionned in Eq. (3.24).

$$TDD = \frac{\sqrt{\sum_{h=2}^{h} I_h^2}}{I_L} \tag{3.24}$$

Even harmonics must be limited to less than 25% of the corresponding odd harmonic limits; this threshold was maintained in IEEE 519–2014 but later relaxed to 50% in IEEE 519–2022.

I_{sc}/I_L	Individual harmonic distortion (%)										TDD (%)
	h < 11		11 ≤ h <17		17 ≤ h < 23		23 ≤ h < 35		h ≥ 35		
	Odd	Even	Odd	Even	Odd	Even	Odd	Even	Odd	Even	
< 20	4	1	2	0.5	1.5	0.375	0.6	0.15	0.3	0.075	5.00

Table 3.5 Current distortion limits for 120 V–69 kV systems specified by IEEE 519-1992 [103].

EN 50160 (European Standard): This standard specifies power quality requirements at the PCC for voltage supplied in public low- and medium-voltage networks. For frequency regulation, the system frequency must remain within ±0.5 Hz (±1% of 50 Hz) during normal operating conditions [50].

3.5 Grid synchronization

A Voltage Source Inverter (VSI), designed for grid connection, requires synchronization with a high power factor as mandated by international standards. The Phase-Locked Loop (PLL) is key to this process, estimating the grid phase angle (θ_g) and extracting the direct and quadrature (dq) components of the PCC voltage from the measured abc signals. This information supports various control blocks, such as current regulators and reference generation [47, 104].

For three-phase systems, the most widely used PLL structures include:

- **Synchronous reference frame PLL (SRF-PLL or dq-PLL):** Standard approach, well-suited for balanced and undistorted grids.
- **Decoupled double synchronous reference frame PLL (DDSRF-PLL):** Enhances SRF-PLL by separating positive- and negative-sequence components, ensuring better performance under unbalanced or distorted conditions.
- **Second-order generalized integrator PLL (SOGI-PLL, including DSOGI-PLL):** Known for strong filtering and robustness in harmonic-rich or distorted environments.

In this thesis, the SRF-PLL is selected since the study focuses on normal grid conditions.

3.5.1 Mathematical modeling of the SRF-PLL

A phase-locked loop (PLL) consists of a phase detector (PD), loop filter (LF), and a voltage-controlled oscillator (VCO). Here, the LF is implemented using a PI controller, while the VCO is represented as an integrator [6]. For balanced three-phase voltages with phase angle θ and peak amplitude V_m, spaced 120° apart (see Fig. 3.13), Clarke and Park transformations (Eqs. (3.26)

and (3.27)) first convert V_{abc} into stationary-frame voltages $V_{\alpha\beta}$, then into synchronous-frame components V_{dq} [105]. By aligning the d-axis component V_d with V_a, the grid phase angle is estimated by forcing the q-axis voltage V_q to zero through the PI controller [106]. The controller output is combined with the feedforward frequency ω_0 to obtain the estimated frequency ω, which the VCO integrates to generate the estimated phase angle θ'. The overall process is shown in Fig. 3.14.

$$\begin{cases} V_a = V_m \sin(\theta) \\ V_b = V_m \sin(\theta - \frac{2\pi}{3}) \\ V_c = V_m \sin(\theta + \frac{2\pi}{3}) \end{cases} \tag{3.25}$$

$$\begin{bmatrix} V_\alpha \\ V_\beta \end{bmatrix} = \frac{2}{3} \begin{bmatrix} 1 & \frac{-1}{2} & \frac{-1}{2} \\ 0 & \frac{\sqrt{3}}{2} & \frac{-\sqrt{3}}{2} \end{bmatrix} \begin{bmatrix} V_a \\ V_b \\ V_c \end{bmatrix} \tag{3.26}$$

$$\begin{bmatrix} V_d \\ V_q \end{bmatrix} = \begin{bmatrix} \cos\theta' & \sin\theta' \\ -\sin\theta' & \cos\theta' \end{bmatrix} \begin{bmatrix} V_\alpha \\ V_\beta \end{bmatrix} \tag{3.27}$$

$$\begin{cases} V_d = V_\alpha \cos\theta' + V_\beta \sin\theta' \\ V_q = -V_\alpha \sin\theta' + V_\beta \cos\theta' \end{cases} \tag{3.28}$$

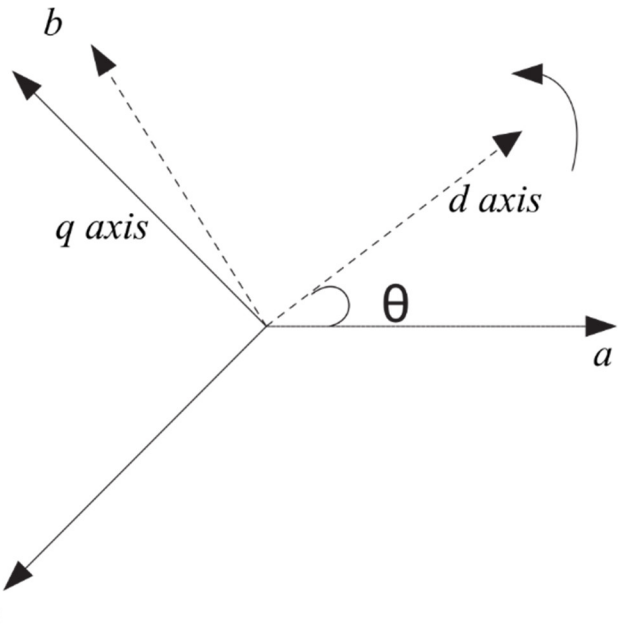

Figure 3.13 The synchronous rotating reference frame.

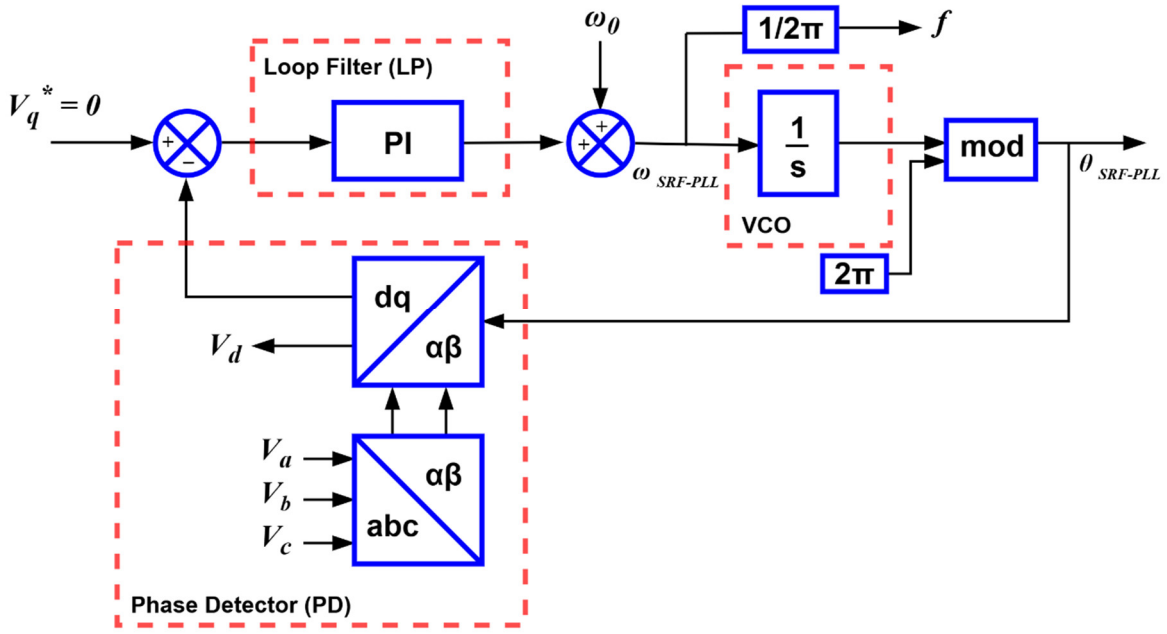

Figure 3.14 SRF-PLL block diagram.

3.5.2 Tuning of PI controller parameters

The PI controller gains of the SRF-PLL are derived by applying the small-angle approximation $\sin(\Delta\theta) \approx \Delta\theta$ as $\Delta\theta \rightarrow 0$ to Eq. (3.28), yielding Eq. (3.29). Accordingly, the simplified SRF-PLL model is shown in Fig. 3.15, with its closed-loop transfer function given in Eq. (3.30).

$$\begin{cases} V_d \approx V_m \\ V_q \approx -V_m(\theta - \theta') \end{cases} \tag{3.29}$$

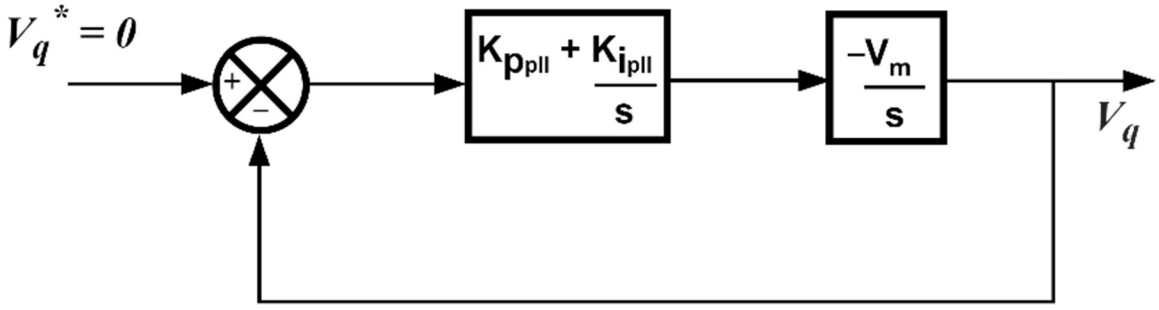

Figure 3.15 Simplified schematic of the SRF-PLL.

$$G_{CL-PLL}(s) = \frac{-V_m(K_{p-pll}s + K_{i-pll})}{s^2 - V_m K_{p-pll}s - V_m K_{i-pll}} \tag{3.30}$$

By equating the denominator of Eq. (3.30) with the standard second-order system form in Eq. (3.31):

$$s^2 + 2\xi\omega_n s + \omega_n^2 \tag{3.31}$$

$K_{p\text{-}pll}$ and $K_{i\text{-}pll}$ are obtained as:

$$\begin{cases} K_{p-pll} = \dfrac{-2\xi\omega_n}{V_m} \\ K_{i-pll} = \dfrac{-\omega_n^2}{V_m} \end{cases} \tag{3.32}$$

The PLL model developed in Simulink is presented in Fig. 3.16.

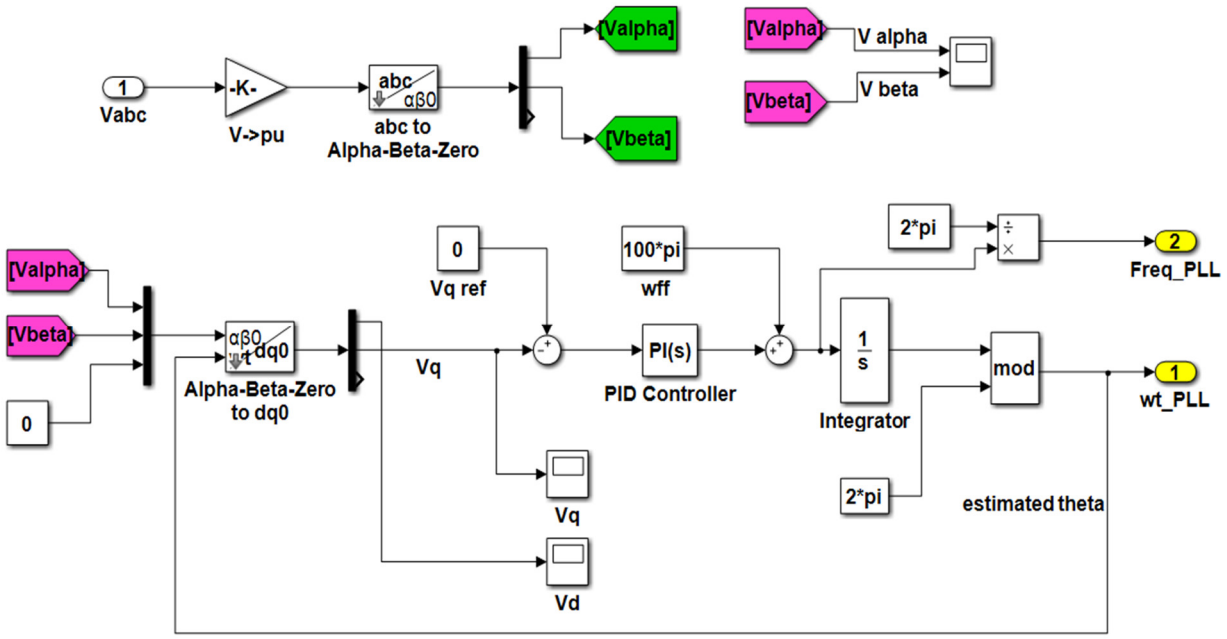

Figure 3.16 MATLAB/simulink model of the SRF-PLL..

3.6 Controller design for the SPWM based VSI

The primary objective of inverter control is to deliver the PV-generated power to the grid effectively, which is achieved using a dual-loop control strategy. The outer loop, shown in red in Fig. 3.17, regulates the DC-link voltage by generating I_d^* for the inner loop, thereby controlling the active current injected into the grid. While the outer loop ensures regulation and system stability, the inner loop focuses on fast response and unity gain. To achieve proper decoupling, the outer loop is typically designed to be 5–20 times slower, as recommended in [107, 108].

3.6.1 Design of inner and outer loops

First, this section elaborates on the controller shown in blue in Fig. 3.17. In the grid-side current feedback (GSCF) scheme, C_f is neglected. To maintain zero phase shift between grid current and

voltage (unity power factor) [109], the reference current I_q^* is set to zero. From Fig. 3.18, the time derivatives of the VSI output current are expressed as:

$$L_{tot}\frac{dI_{abc}}{dt} = V_{inv} - V_{abc} \tag{3.33}$$

Here, V_{inv} denotes the inverter voltage. The symbols I_{abc} and V_{abc} represent the grid current and grid voltage, respectively, while L_{tot} refers to the total filter inductance.

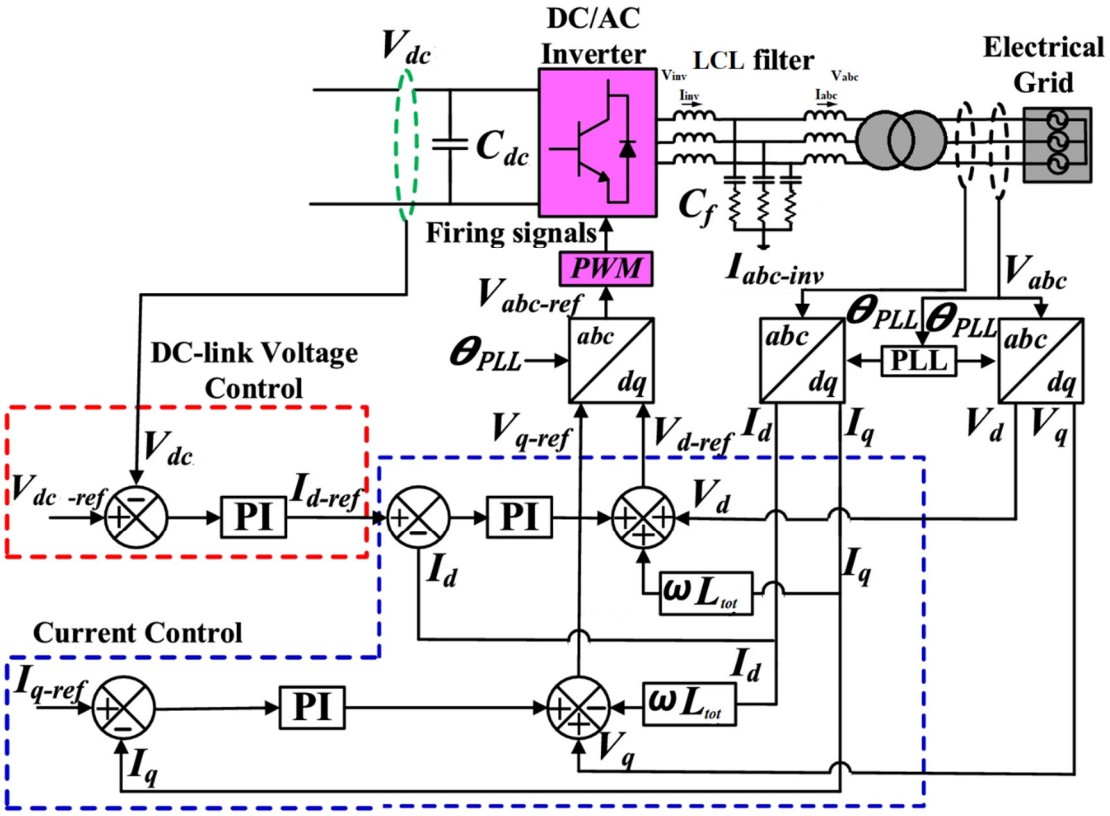

Figure 3.17 VSI controller with GSCF.

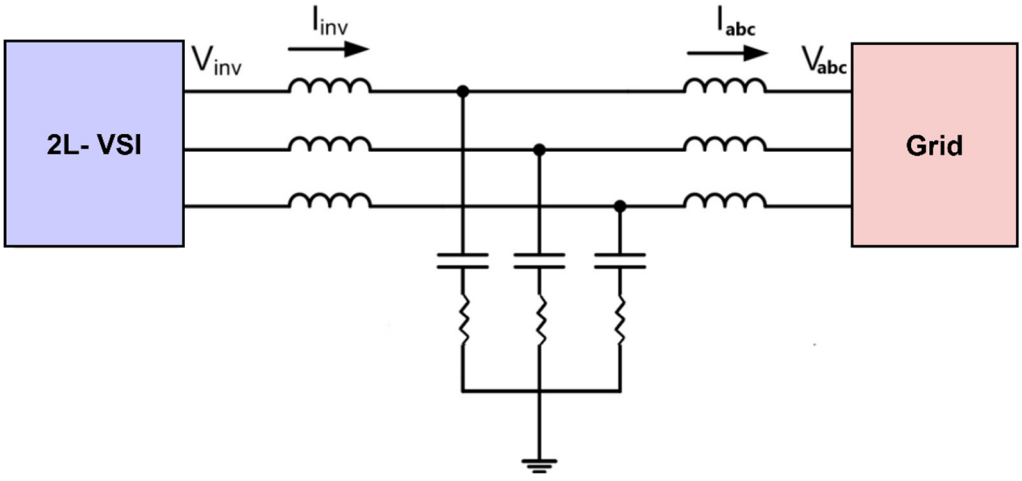

Figure 3.18 Grid-interfaced VSI diagram

Applying the Clarke-Park transformation matrix T to both sides of Eq. (3.33) allows the VSI to be expressed in the dq frame, as shown in Eq. (3.35).

$$T=\sqrt{\frac{2}{3}}\begin{bmatrix}\cos(\omega t) & \cos(\omega t-\frac{2\pi}{3}) & \cos(\omega t+\frac{2\pi}{3})\\ -\sin(\omega t) & -\sin(\omega t-\frac{2\pi}{3}) & -\sin(\omega t+\frac{2\pi}{3})\\ \frac{1}{\sqrt{2}} & \frac{1}{\sqrt{2}} & \frac{1}{\sqrt{2}}\end{bmatrix} \tag{3.34}$$

$$\begin{bmatrix}V_{inv,d}\\ V_{inv,q}\end{bmatrix}=L_{tot}\frac{d}{dt}\begin{bmatrix}I_d\\ I_q\end{bmatrix}+L_{tot}\begin{bmatrix}0 & -\omega\\ \omega & 0\end{bmatrix}\begin{bmatrix}I_d\\ I_q\end{bmatrix}+\begin{bmatrix}V_d\\ V_q\end{bmatrix} \tag{3.35}$$

In order to compensate for the cross-coupling term in Eq. (3.35), the PI controller outputs are modified by including the decoupling terms $+\omega L_{tot}I_q$ for the d-axis and $-\omega L_{tot}I_d$ for the q-axis [110] as shown in Fig. 3.17. The inverter output then follows these control rules to produce the reference voltages:

$$V_{inv,d}^{*}=(K_{p-c}+\frac{K_{i-c}}{s})(I_d^{*}-I_d)+L_{tot}\omega I_q+V_d \tag{3.36}$$

$$V_{inv,q}^{*}=(K_{p-c}+\frac{K_{i-c}}{s})(I_q^{*}-I_q)-L_{tot}\omega I_d+V_q \tag{3.37}$$

To generate the VSI switching signals, $V_{inv,d}^{*}$ and $V_{inv,q}^{*}$ are first transformed into the abc reference frame.

In modeling the control scheme, it is important to include the delays that occur in the control loop, namely the digital processing delay and the PWM transport delay [111]. These are generally modeled as a single sample time delay T_{s-c} for processing, along with an additional $0.5T_{s-c}$ delay introduced by the zero-order hold of the digital PWM [112, 113]. As a result, the overall delay time constant of the loop is given by $T_{eq}=1.5T_{s-c}$, where T_{s-c} represents the sampling time of the inner control loop.

When operating at a low frequency ($\omega<\omega_{res}$):

- R_d can be neglected since it is connected in series with C_f and staisfies $R_d \ll 1/(C_f\omega)$
- The term $s^3C_fL_iL_g$ is negligible in comparison to (L_i+L_g).

$$Y_{LCL}(s)\approx\frac{1}{s(L_i+L_g)} \tag{3.38}$$

Therefore, the LCL filter can be simplified to a first-order delay element, as shown in Eq. (3.38), due to the decoupling of the dq axes. This simplification enhances the tracking performance of the PI controllers. In this case, u_{dis}, illustrated in Fig. 3.19(a), denotes the grid voltage disturbance. The inner-loop time constant T_{inner} is affected by T_{eq} and is given as $T_{inner}=\alpha^2T_{eq}$.

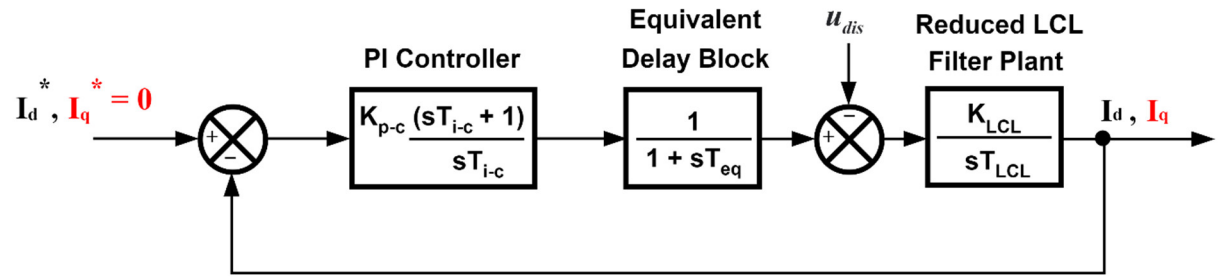

(a) inner current control loop only

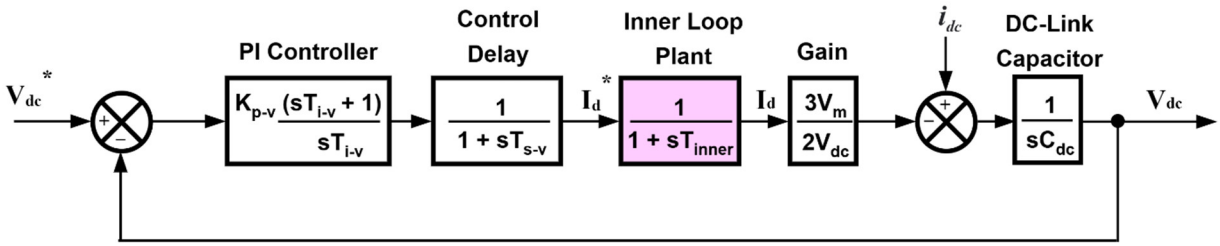

(b) inner loop inside outer loop

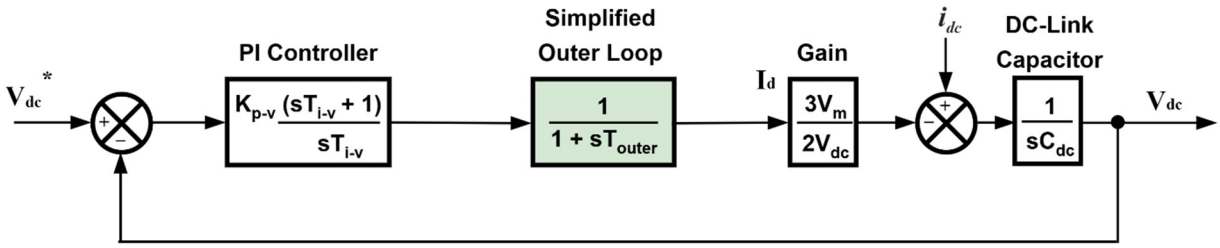

(c) outer loop control with delay

Figure 3.19 Vector Current control loops of the 2L-VSI.

In studying the outer loop highlighted in red in Fig. 3.17, it is assumed that the VSI operates without losses, allowing the application of the power balance between P_{ac} and P_{dc} [6].

$$P_{dc} \approx P_{ac} \rightarrow v_{dc} i_{dc} - v_{dc} C_{dc} \frac{dv_{dc}}{dt} = \frac{3}{2}(v_d i_d + v_q i_q) \tag{3.39}$$

Here, i_{dc} denotes the input current.

An equivalent first-order transfer function is used to approximate the closed-loop behavior of the GSCF controller, as shown in Fig. 19(b). The DC-link loop is built using Eq. (3.40), while I_d^* is given in Eq. (3.41).

$$v_{dc}(s) = \frac{1}{sC_{dc}} \left(i_{dc}(s) - \frac{3}{2} \frac{V_m}{V_{dc}} i_d(s) \right) \tag{3.40}$$

$$I_d^* = (K_{p-v} + \frac{K_{i-v}}{s})(V_{dc}^* - V_{dc}) \tag{3.41}$$

The outer-loop time T_{outer} accounts for the effect of the inner loop, defined as the sum of the DC-link voltage control sampling time T_{s-v} and T_{inner}. The resulting simplified outer loop, shown in Fig. 3.19(c), is obtained.

3.6.2 PI controller tuning for inner and outer loops

To adjust the PI controller in this loop, the Symmetrical Optimum (SO) method is applied, following the procedure outlined in [107], where it was successfully implemented for PI controllers in a small PMSG-based wind energy conversion system. The SO method is designed to increase the phase margin at a specific crossover frequency ω_c, thereby improving the system's ability to handle delays and reject disturbances. It is particularly advantageous in cases where the open-loop transfer function includes a pole close to or at the origin, as the SO criterion helps in selecting appropriate PI controller parameters [114].

When the open-loop transfer function is approximated as:

$$G_{p1}(s) = \frac{K_1}{(1+sT_1)(1+sT_2)} \quad ; T_1 >> T_2 \tag{3.42}$$

According to the SO criterion, the proportional gain and the integral time constant $K_{p1,SO}$ and $T_{i1,SO}$, respectively are determined as:

$$\begin{cases} K_{p1,SO} = \dfrac{T_1}{\alpha T_2 K_1} \\ T_{p1,SO} = \alpha^2 T_2 \end{cases} \tag{3.43}$$

If instead the open loop transfer function can be approximated by:

$$G_{p2}(s) = \frac{K_2}{s(1+sT_2)} \tag{3.44}$$

The SO tuning rules are then defined as:

$$\begin{cases} K_{p2,SO} = \dfrac{1}{\alpha T_2 K_2} \\ T_{p2,SO} = \alpha^2 T_2 \end{cases} \tag{3.45}$$

Here, T_1 denotes the dominant plant time constant and T_2 the parasitic, or minor, time constant. The parameters K_1 and K_2 are the plant gains associated with the two model forms. The design parameter α is determined using Eq. (3.46) to ensure the required damping ratio ξ.

$$\alpha = 2\xi + 1 \tag{3.46}$$

Accordingly, the tuning of the PI controller gains for the inner loop of the present work is carried out by matching its open-loop transfer function, $H_{ol,c}(s)$, to $G_{p2}(s)$, as given by:

$$H_{ol,c}(s)=\frac{K_{LCL}}{s(1+sT_{inner})}=\frac{\frac{1}{(L_i+L_g)}}{s(1+sT_{inner})}\Leftrightarrow G_{p2}(s)=\frac{K_2}{s(1+sT_2)}\Rightarrow\begin{cases}K_{p-c}=\dfrac{L_i+L_g}{\alpha T_{inner}}\\ T_{i-c}=\alpha^2 T_{inner}\end{cases} \quad (3.47)$$

Similarly, for the outer loop, the PI controller gains are determined from its open-loop transfer function, $H_{ol,v}(s)$, as follows:

$$H_{ol,v}(s)=\frac{\frac{3V_m}{2V_{dc}C_{dc}}}{s(1+sT_{outer})}\Leftrightarrow G_{p2}(s)=\frac{K_2}{s(1+sT_2)}\Rightarrow\begin{cases}K_{p-v}=\dfrac{2V_{dc}C_{dc}}{3V_m\alpha T_{outer}}\\ T_{i-v}=\alpha^2 T_{outer}\end{cases} \quad (3.48)$$

Implementation of the dual-loop model was carried out in the MATLAB/Simulink environment, as illustrated in Fig. 3.20.

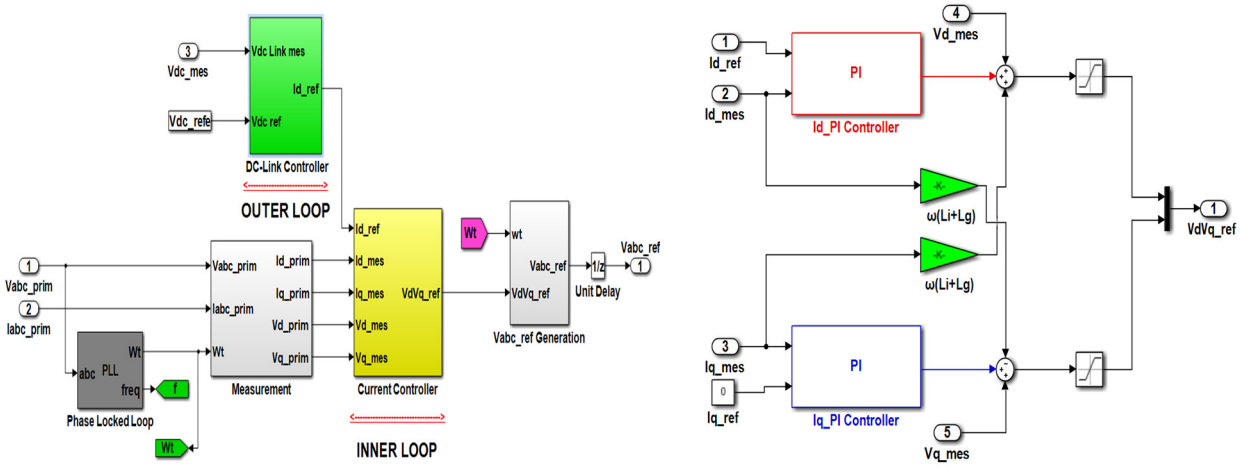

(a) dual loops (b) inner loop

Figure 3.20 Simulink model of 2L-VSI controller.

3.7 Transmission line parameters

As highlighted in Chapter I, the power generated by the Oued El Kebrit PV plant is transferred to the El Aouinet substation through the transmission line presented in Fig. 3.21(b). This line employs an AAAC (All Aluminum Alloy Conductors) cable, also referred to as "Almelec," with a cross-sectional area of 93.3 mm² and a length of 6.3 km. The transmission line is represented using the π-model seen in Fig. 3.21(a), which is characterized by four key parameters: resistance (R), inductive reactance (X), susceptance (B), and shunt conductance (G). At medium voltage levels, the contribution of shunt conductance is typically disregarded due to its minimal value, while the other parameters are calculated analytically as [115]:

3.7.1 Resistance

The conductor's resistance per unit length, denoted as R′ (Ω/km), can be calculated according to the following expression:

$$R' = \frac{\rho}{A} 1000 \tag{3.49}$$

Here, A denotes the cross-sectional area of the conductor in (m^2), and ρ represents the resistivity of the material in (Ω·m).

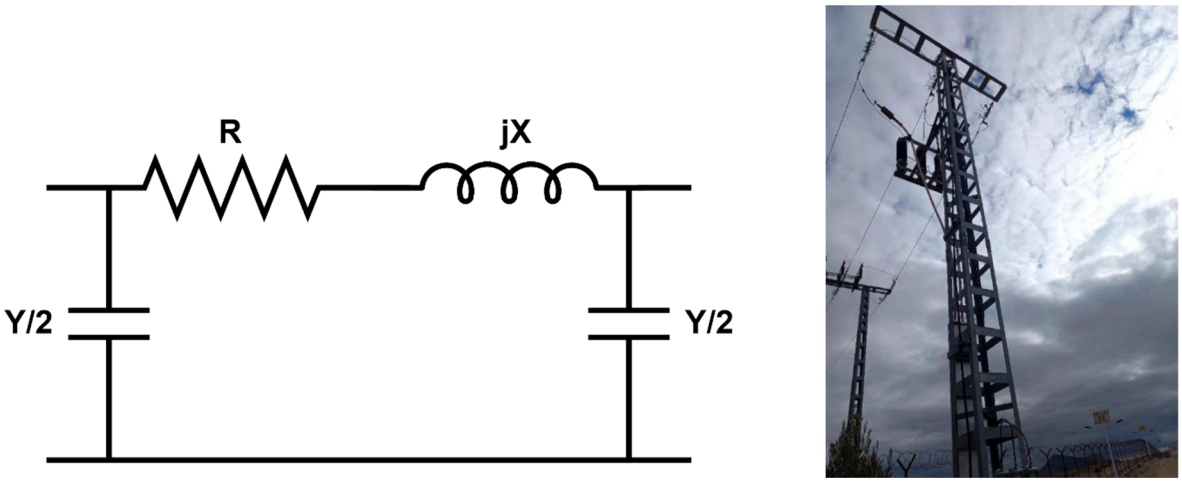

(a) (b)

Figure 3.21 PV plant transmission line: (a) nominal PI model, (b) real photo of the transmission line.

3.7.2 Inductive reactance

For overhead conductors and cables, the inductive reactance per unit length X′ (Ω/km) is calculated using:

$$X' = 0.144 \log\left(\frac{D_m}{r}\right) + 0.0157 \tag{3.50}$$

For the horizontal phase configuration illustrated in Fig. 3.21(b), D_m is calculated using Eq. (3.51).

$$D_m = \sqrt[3]{D.D.2D} = 1.26D \tag{3.51}$$

Here, r refers to the conductor's radius, while D_m indicates the mean geometric spacing between conductors, with both quantities measured in (Ω·m).

Accordingly, the line impedance Z can be written in complex form, where R' corresponds to the real component and X' corresponds to the imaginary component.

3.7.3 Susceptance

For various line configurations, the susceptance per unit length B' (S/km) is determined by the electric field interactions between conductors and between each conductor and the ground, as given by :

$$B' = C\omega = C.2.\pi.f_g = \frac{7.58.10^{-6}}{\log\left(\frac{D_m}{r}\right)} \tag{3.52}$$

Thus, the line admittance Y can be expressed as in complex form, where G' represents the real part and B' represents the imaginary part.

Before the point of common coupling (PCC), a 0.315/31.5 kV step-up transformer with a capacity of 1250 kVA is utilized (see Appendix D). The electrical grid was simulated in MATLAB/Simulink using a three-phase 220 kV voltage source connected to a 220/31.5 kV step-down transformer rated at 30 MVA, as illustrated in Fig. 3.22. The three demand centers—Mesloula, Meskiana, and Ouenza 3—are modeled as static loads, with their average power consumption derived from the consumption records of SONELGAZ, the Algerian national electricity and gas provider. All the parameters used in the model are detailed in Table 3.6.

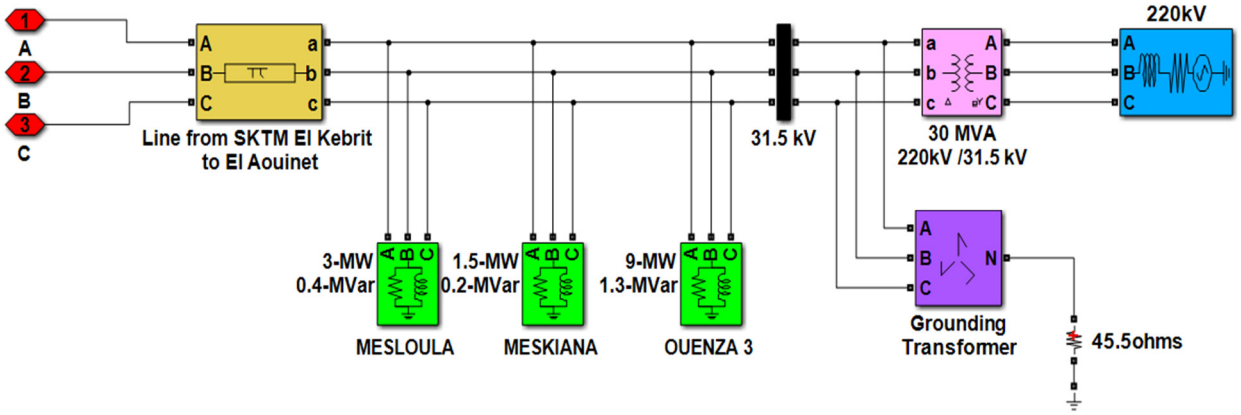

Figure 3.22 The utility grid model in MATLAB/simulink.

3.8 Conclusion

In this chapter, after presenting the role of each constituent element of the AC stage of the grid-connected PV system, their mathematical models were developed and implemented in the MATLAB/Simulink environment using real data from the Oued El Kebrit PV plant. The modeling began with the selection of the DC-link voltage, followed by the implementation of the SPWM-based 2L-VSI. Next, an LCL filter was designed for harmonic mitigation, an SRF-PLL was implemented for grid synchronization, and finally the transmission line parameters were calculated analytically to reproduce the actual operating conditions of the plant.

Current feed-in to the grid is ensured through control of the SPWM-based 2L-VSI using a dual-loop structure, where the inner current loop and outer DC-link voltage loop were tuned using the Symmetrical Optimum method.

To ensure stable power quality and effective harmonic attenuation, the LCL filter was designed in accordance with IEEE standards, taking into account the rated power, DC-link voltage, switching frequency, and grid parameters of the Oued El Kebrit PV plant. The filter performance was improved by introducing a passive damping resistor in series with the capacitor, which suppresses resonance phenomena while maintaining low fundamental-frequency losses.

Moreover, since precise synchronization with the grid is essential for stable current injection and unity power factor operation, the developed SRF-PLL block was tuned to provide a reliable synchronization signal for the VSI control system while maintaining the frequency within the recommended European standards.

Up to this point, all elements have been modeled separately. In the next chapter, they are integrated into the complete PV plant model to enable system-level simulations and performance analysis.

PV array with Yingli Solar YL250P-29b				**LCL filter**				**Transmission line**			
N_s	60	N_{ss}	22	x	2.5 %	L_i	80.719 µH	ρ	32.6 nΩ.m	R'	0.350 Ω/km
N_{pp}	182	$V_{pv,mpp}$	655.6V	$RAF_{sw\text{-}vsi}$	20 %	C_f	267.33 µF	A	93.3 mm^2	X'	0.4 Ω/km
$I_{pv,mpp}$	1527 A	$P_{pv,mpp}$	1 MW	$\Delta I_{b,max}/I_{b,max}$	15 %	L_g	5.6852 µH	D	2 m	B'	2.844
				f_{res}	4.22 kHz	R_d	0.0550 Ω	r	5.45 mm	G'	µS/km neglected

Boost converter				**Step up transformer: SCLB10 1250/30/2X0.315**		**Electrical grid: (El Aouinet electrical substation)**	
V_{dc}	1025 V	R	1.050Ω	Power rating	1250 KVA	V_g	220 kV
$f_{sw\text{-}boost}$	20 kHz	I_L	1524A	*Transformation ratio*	0.315/31.5kV	f_g	50 Hz
$\Delta I_l/I_L$	10 %	L	78 µH	*Per unit impedance*	0.366 + j0.619 pu	*X/R ratio*	7
$\Delta V_{dc}/V_{dc}$	5 %	C_{pv}	343 µF	**Loads**		**Grid transformer**	
D	0.36	C_{dc}	30298 µF	*Mesloula*	P_1= 3 MW, Q_1= 0.4 MVar	Power rating	30 MVA
				Meskiana	P_2= 1.5 MW, Q_2= 0.2 Mvar	*Transformation ratio*	0.315/31.5kV
				Ouenza 3	P_3= 9 MW, Q_3= 1.3 Mvar	*Per unit impedance*	0.0064 + j0.064 pu

2L-VSI		**Inner loop**		**Outer loop**		**PLL**	
$f_{sw\text{-}vsi}$	10 kHz	$T_{s\text{-}c}$	0.085 ms	$T_{s\text{-}v}$	1.7 ms	$K_{p\text{-}pll}$	-420
V_{LL}	315 V	$K_{p\text{-}c}$	1	$K_{p\text{-}v}$	-13.64	$K_{i\text{-}pll}$	-90000
		$K_{i\text{-}c}$	11	$K_{i\text{-}v}$	-958.43		

Table 3.6 Model parameters.

Chapter IV

Results, Analysis, and Discussion

4.1 Introduction

This chapter presents the complete simulation and performance assessment of the proposed 1 MW grid-connected PV system, developed using the individual components modeled in previous chapters. The study begins with steady-state evaluation under standard test conditions (STC), followed by dynamic analysis under varying solar irradiance to replicate real-world operating scenarios. The performance is examined on both the DC and AC sides, focusing on power stability, control effectiveness, power quality indices, and compliance with international standards (IEEE and EN). Furthermore, the overall efficiency and harmonic distortion are quantified, and the model's outcomes are benchmarked against the literature and validated with real operational data from the Oued El Kebrit PV plant.

4.2 Simulation setup and operating conditions

The proposed 1 MW grid-connected photovoltaic (PV) system, modeled with data of Oued El Kebrit PV plant, was simulated in MATLAB/Simulink to assess its steady-state and transient performance. Fig. 4.1 shows the developed model.

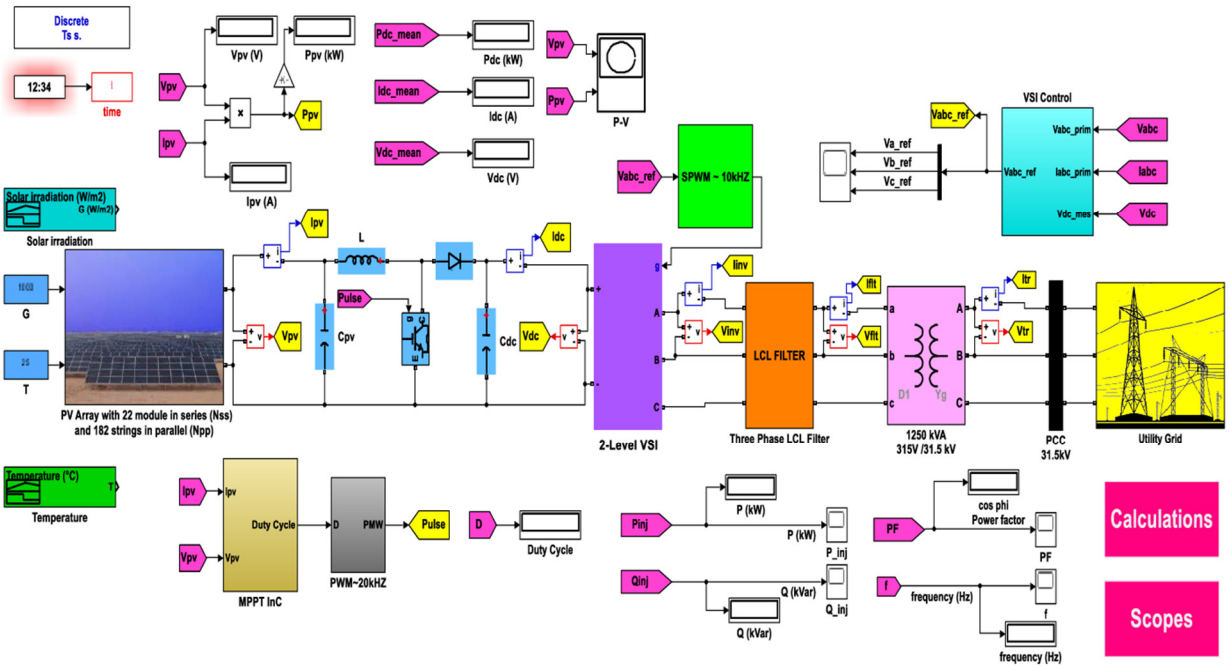

Figure 4.1 Simulation model in Simulink of the 1 MW PV facility at Oued El Kebrit, Souk Ahras.

The simulation was first carried out under STC, defined by solar irradiance G = 1000 W/m² and cell temperature T = 25 °C. These conditions represent the reference baseline for evaluating PV performance.

To investigate the dynamic behavior of the system, a disturbance scenario was introduced at t = 0.5 s, where solar irradiance dropped suddenly from 1000 W/m² to 700 W/m² as depicted in Fig. 4.2. This scenario replicates a real-world condition such as sudden cloud cover passing over the PV array. Temperature was kept constant at 25 °C for all tests to isolate the impact of irradiance variation on system dynamics.

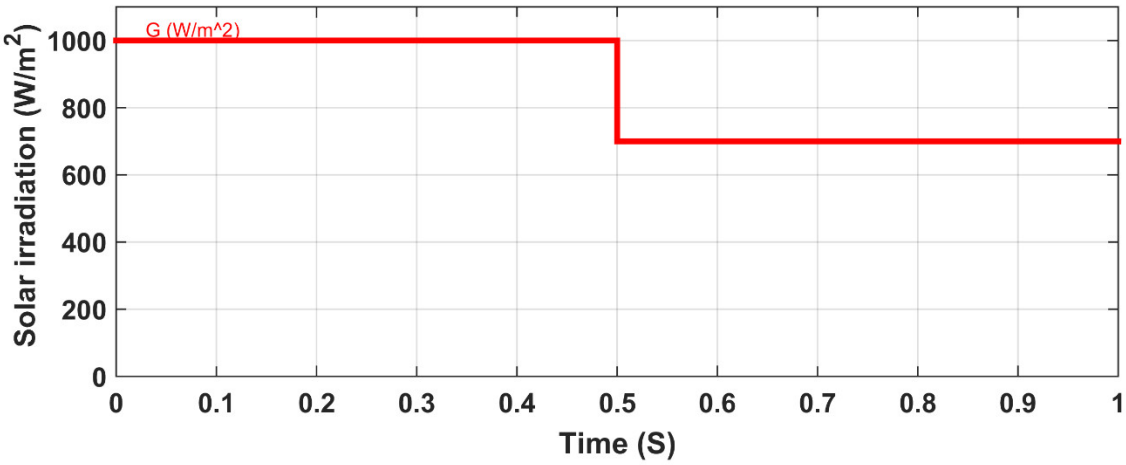

Figure 4.2 Solar irradiance profile

The analysis focused on the following key aspects:

- **DC-side performance**: PV voltage (V_{pv}), current (I_{pv}), power (P_{pv}), and DC-link voltage stability.
- **AC-side performance**: injected grid current, grid voltage stability at the point of common coupling (PCC), active and reactive power control, and unity power factor operation.
- **Power quality metrics**: frequency stability, harmonic distortion (THD_v, THD_i, and TDD), and total conversion efficiency.
- **Transient behavior**: system response to irradiance changes, current controller performance, and DC-link stabilization.

These conditions allow a comprehensive evaluation of both static performance under STC and dynamic resilience under real-world disturbances.

4.3 Performance analysis and compliance with IEEE and EN standards

4.3.1 On DC-side

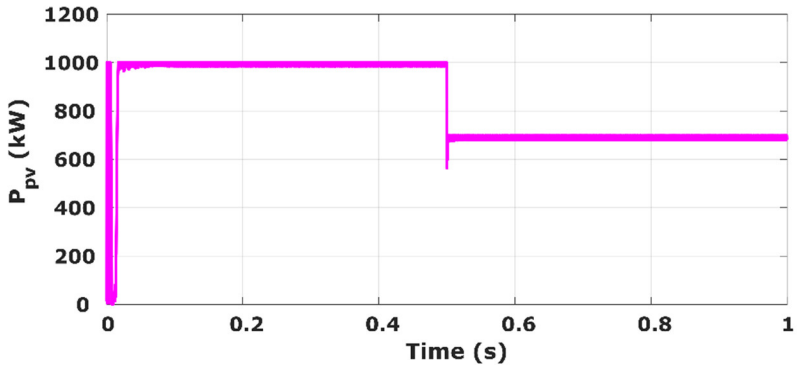

(a)

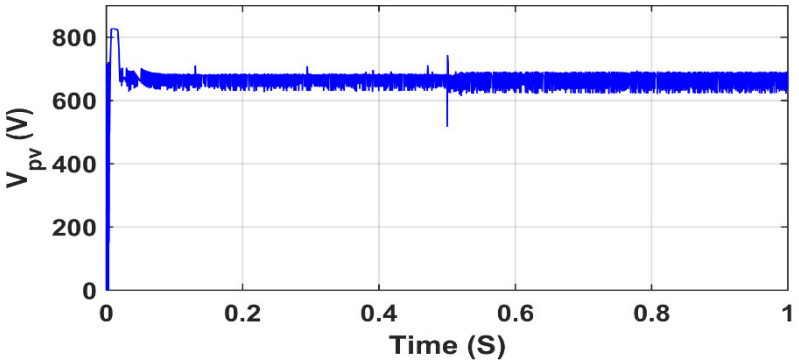

(b)

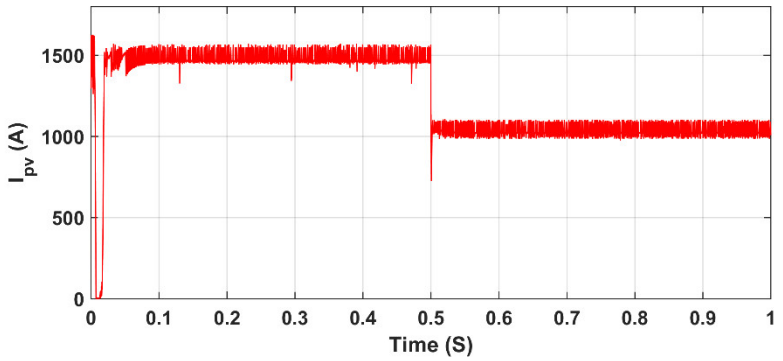

(c)

Figure 4.3 Simulation results : (a) PV array output power, (b) PV array output voltage, (c) PV array output current.

As shown in Fig. 4.3, at 2 ms the PV generator reaches its optimal operating point, supplying about 1527 A at nearly 655.6 V, which corresponds to a power output of 1 MW at the MPP. When solar irradiation decreases, both the PV current (I_{pv}) and power (P_{pv}) experience a

noticeable drop, while the voltage (V_{pv}) remains almost unchanged. Specifically, the current falls from 1523 A to 1066 A, and the power output decreases from 1001 kW to 698.3 kW—approximately a 30% reduction. This behavior is consistent with the fact that Ipv is directly proportional to solar irradiation, as discussed in Chapter II.

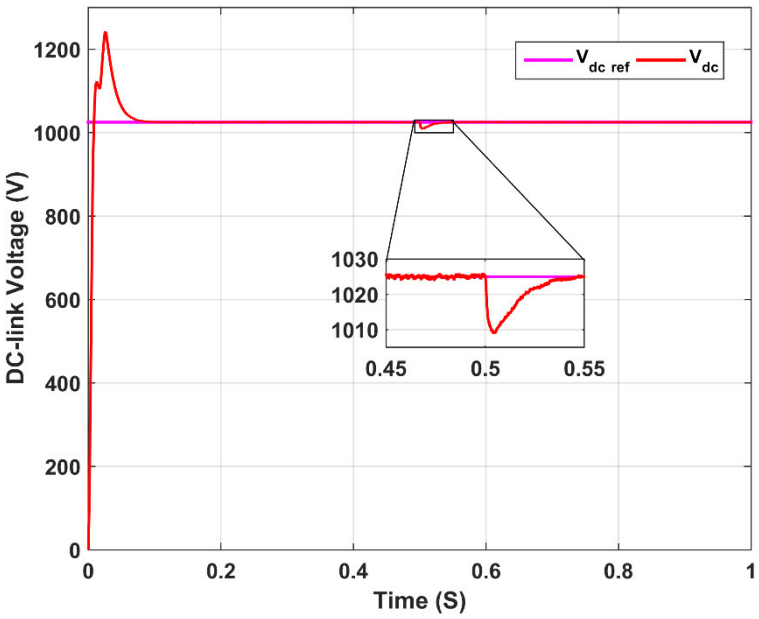

Figure 4.4 Reference and measured DC-link voltage waveforms.

As illustrated in Fig. 4.4, the reference and measured DC-link voltages show that after nearly 0.08 seconds (about four cycles), the voltage reached and stabilized at the set value of 1025 V. At t = 0.5 s, the DC-link displayed a short and slight voltage drop of roughly 50 ms. After this minor disturbance, it quickly returned to and maintained the 1025 V level. This stability is important, as it supports the correct functioning of the VSI and allows it to supply the required output currents efficiently.

4.3.2 On AC-side

From Fig. 4.5, it is evident that the grid voltage and current waveforms at the PCC reached steady state within just three AC cycles, demonstrating strong performance under STC conditions. At t = 0.5 s, a sudden drop in irradiance led to a noticeable reduction in the grid current amplitude. Nevertheless, this change had no effect on the dynamic behavior of the grid voltage waveform at the PCC, as it is dictated by the AC network.

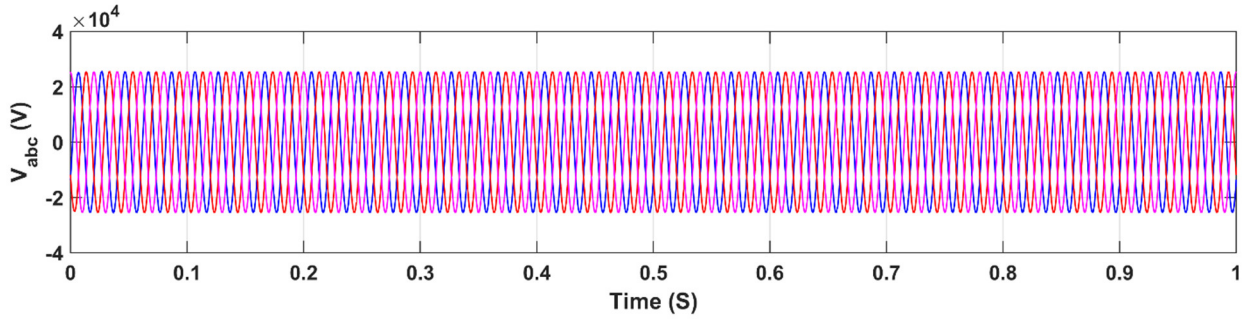

(a)

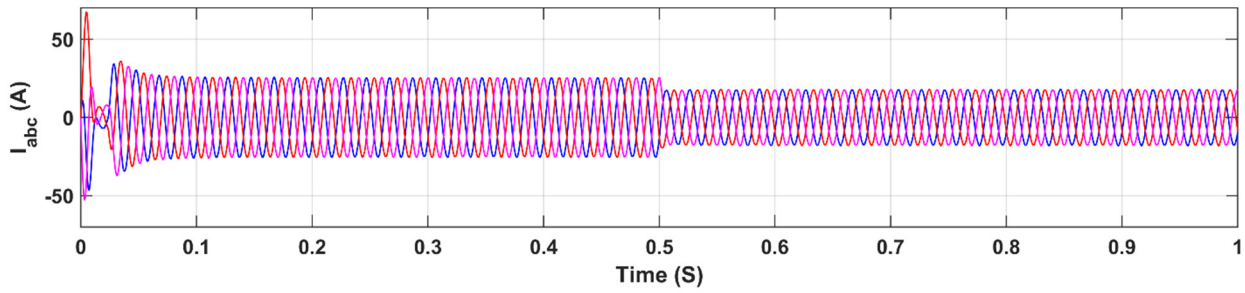

(b)

Figure 4.5 Grid current and voltage profiles at PCC.

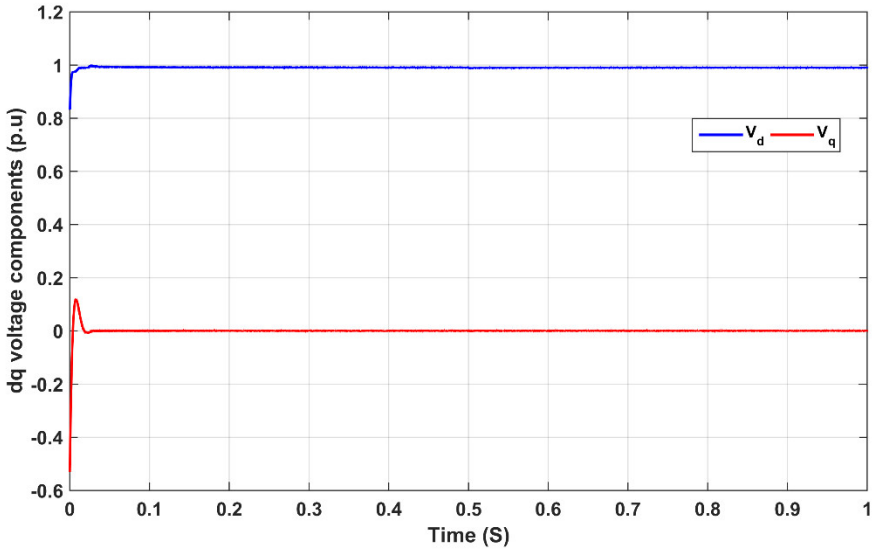

Figure 4.6 The d- and q-axis components of the voltage.

From Fig. 4.6, it can be seen that the quadrature component V_q at the PCC was successfully driven to zero by the PLL, while the direct-axis component V_d converged to the grid voltage magnitude. This confirms that the PLL accurately aligned the grid voltage vector with the d-axis, resulting in $V_d = V_m = 1$ pu.

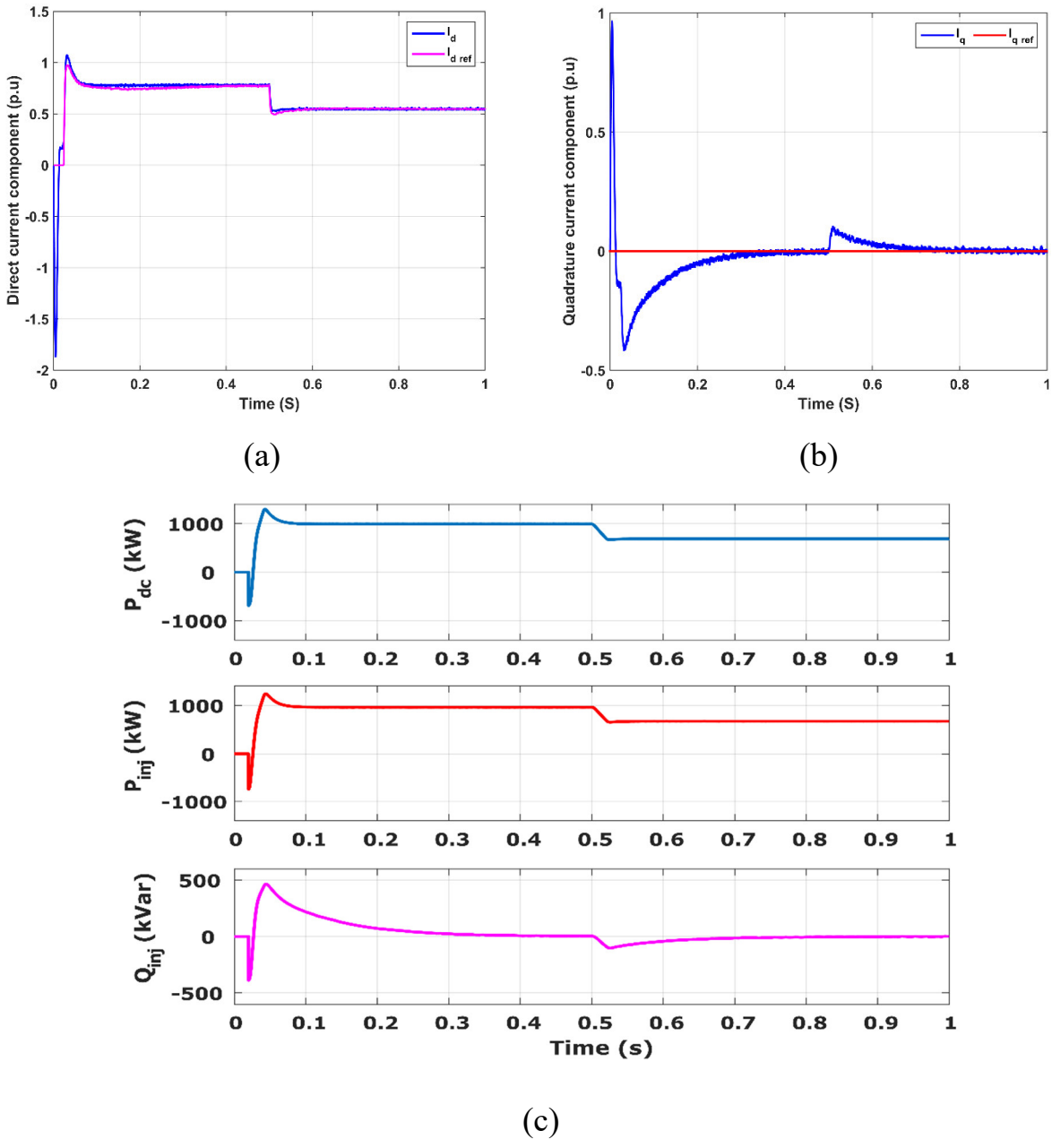

Figure 4.7 Simulation results: (a) direct component of injected current (I_d), (b) quadrature component of injected current (I_q), and (c) injected power at the PCC.

As illustrated in Fig. 4.7(a) and (b), the injected dq-axis current components (I_d and I_q) accurately tracked their respective reference values. To maintain unity power factor, the current controller forced I_q, which determines the inverter's reactive power, to remain at zero. At the same time, the DC-link voltage controller provided the reference signal I_d^*, which the I_d component was regulated to follow. When the input power to the DC-link capacitor decreased, the output power was adapted to match the new control target. Consequently, the outer-loop controller generated an updated reference current for the VSI, resulting in the injected I_d being regulated to the new reference of 0.55 pu.

In addition, Fig. 4.7(b) and (c) reveal that the I_q component experienced a slight increase between t = 0.5 s and 0.6 s (around five cycles). This behavior was caused by the sudden decrease in solar irradiance, which temporarily lowered the injected reactive power (Q_{inj}). During this transient phase, I_q increased to compensate and preserve constant reactive power. After the system settled, I_q returned to its reference value (I_q = 0), thereby re-establishing unity power factor operation.

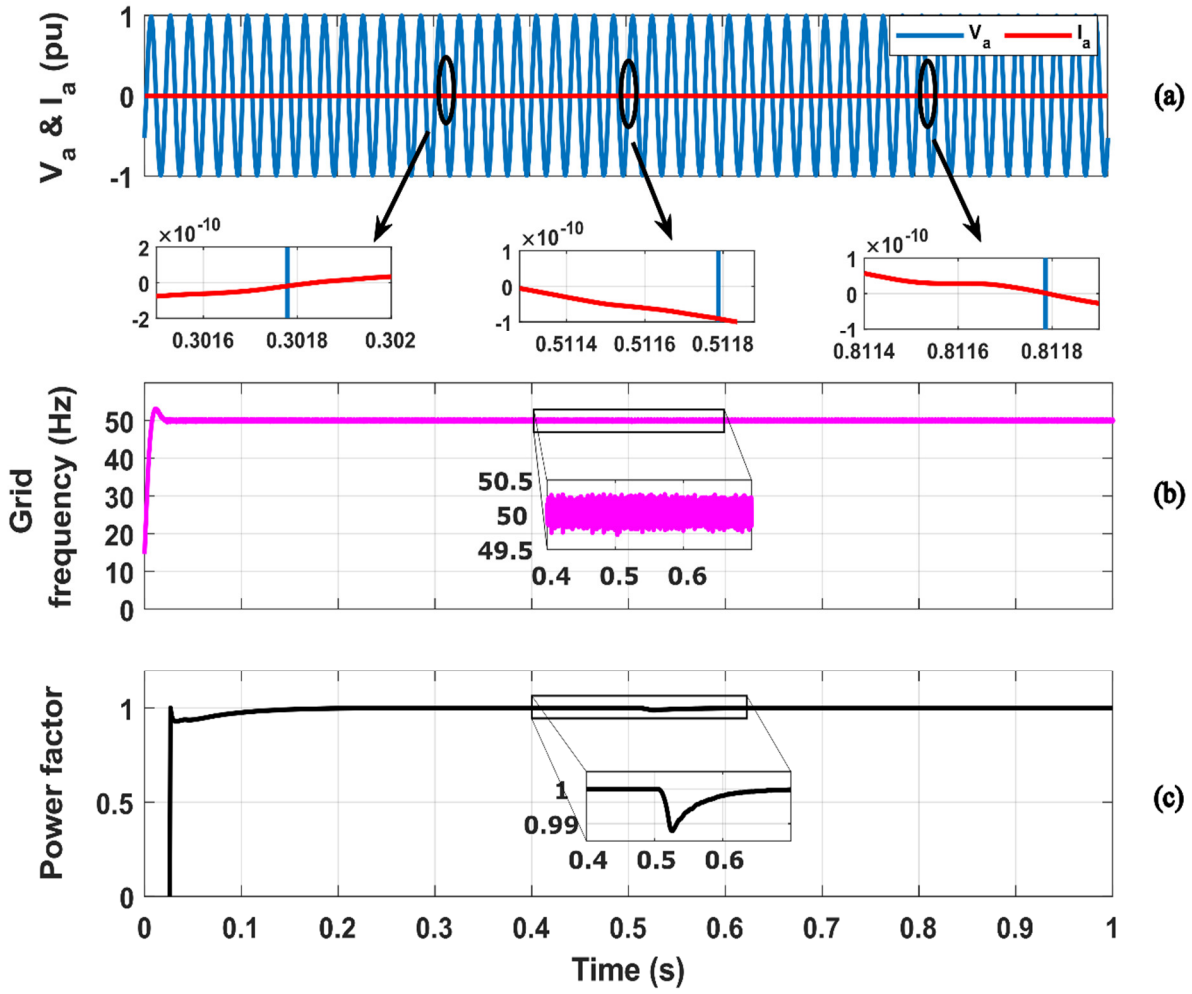

Figure 4.8 Simulation results: (a) Phase voltage and current at PCC, (b) grid frequency, and (c) power factor.

Fig. 4.8 shows that the phase shift between the grid voltage and current at the PCC was slightly disturbed for nearly 0.1 s following the irradiance drop (between t = 0.5 and 0.6 s). This short disturbance is reflected in the power factor curve, which temporarily decreased to 0.99. After t = 0.6 s, the voltage and current returned to full synchrony, ensuring unity power factor as required by IEEE 929-2000 (Clause 4.5). Unlike the power factor, the system frequency was not influenced by irradiance variation and remained stable within the permissible range of 49.5–50.5

Hz, thereby meeting the European EN 50160 standard that limits frequency deviation to ±1% of 50 Hz.

4.3.3 Efficiency

Analysis of the power curves in Figs. 4.3(a) and 4.7(c) indicates that the static MPPT efficiency under STC is approximately 99.13%. This efficiency can be expressed as:

$$\eta_{mppt,static} = \frac{P_{dc}}{P_{pv,mpp}} \tag{4.1}$$

Meanwhile, the overall DC–AC conversion process, which accounts for inverter and transformer losses, yields a static conversion efficiency of about 97.23%, given by:

$$\eta_{conv} = \frac{P_{inj}}{P_{dc}} \tag{4.2}$$

This equals 964.9 kW of active power supplied to the grid. Since the current controller efficiently minimizes reactive power, the overall system efficiency is 96.38%, represented as:

$$\eta_{tot} = \eta_{mppt,static} . \eta_{conv} \tag{4.3}$$

These outcomes demonstrate the effectiveness and reliability of the power conditioning unit (PCU) incorporated in the proposed model.

4.3.4 Harmonic Distortion

When solar irradiance drops suddenly, the comparison of unfiltered and filtered VSI output voltage, together with their FFT spectrum results in Fig. 4.9(a) and (b), makes it clear that the unfiltered signal is non-sinusoidal and contains a large distortion level (137.12%). After applying the LCL filter, the waveform becomes almost sinusoidal, and the THD decreases to 1.24%, which complies with the IEEE 519-1992 standard requirement of less than 5% (Clause 11.5). In addition, the delta-star transformer connection lowers the THD further to 0.19%, as illustrated in Fig. 4.9(d). This supports the advantages reported in previous studies, where delta-star transformers are known to prevent secondary voltage distortion and remove the influence of 3rd harmonic components.

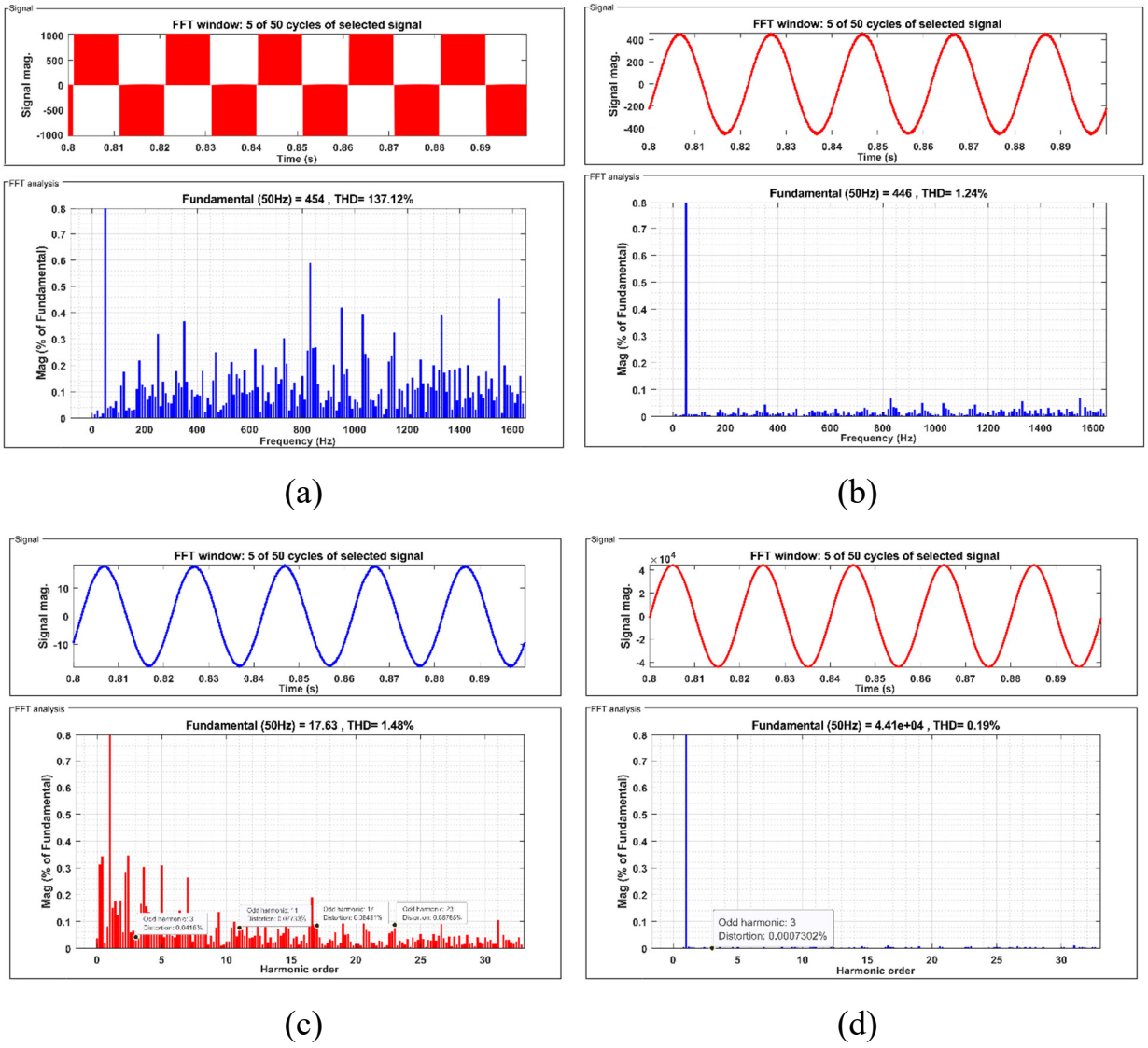

Figure 4.9 Simulation results: (a) FFT spectrum and THD of the VSI voltage before the filter, (b) FFT spectrum and THD of the VSI voltage after the filter, (c) FFT spectrum and THD of the current at PCC at 700 W/m^2 and 25°C, and (d) FFT spectrum and THD of the voltage at PCC.

At the PCC, positioned directly after the step-up transformer, the FFT results in Fig. 4.9(c) and Table 4.1 show that lowering the irradiation level slightly raised the THDi,pcc. The distortion became more noticeable as the current magnitude decreased.

	During STC : G= 1000 W/m^2, T= 25°C	**During : G= 700 W/m^2, T= 25°C**
$THD_{i,pcc}$ (%)	1.21%	1.48%
TDD_{pcc} (%)	$TDD_{pcc} \approx THD_{i,pcc}$	1.16%

Table 4.1 THD_i vs. TDD at PCC

More specifically, the $THD_{i,pcc}$ increased from 1.21% under STC (1000 W/m², 25°C) to 1.48% at 700 W/m² and 25°C, marking a rise of 22.31%. Nevertheless, both values remain within the limits defined by the IEEE standard, thereby fulfilling grid interconnection requirements.

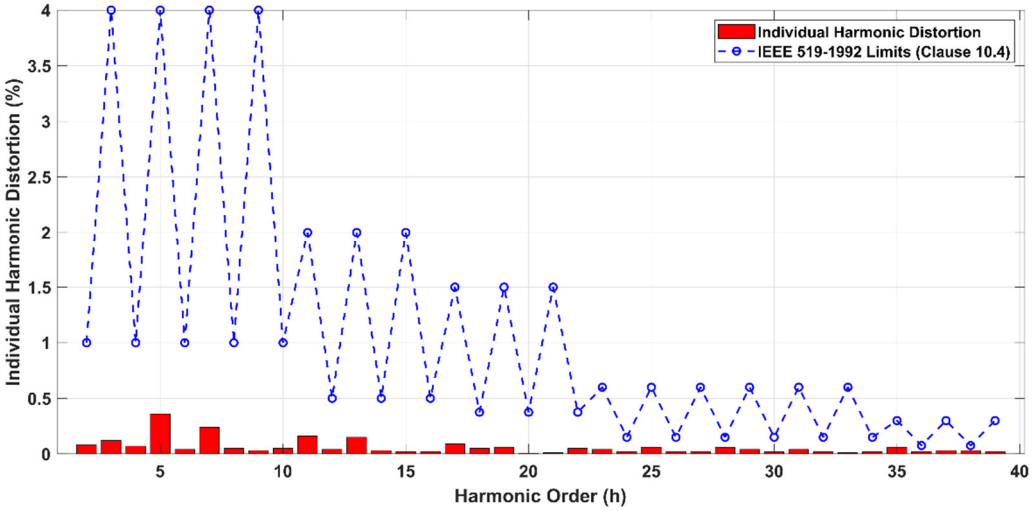

(a) at 1000 W/m^2, T= 25°C

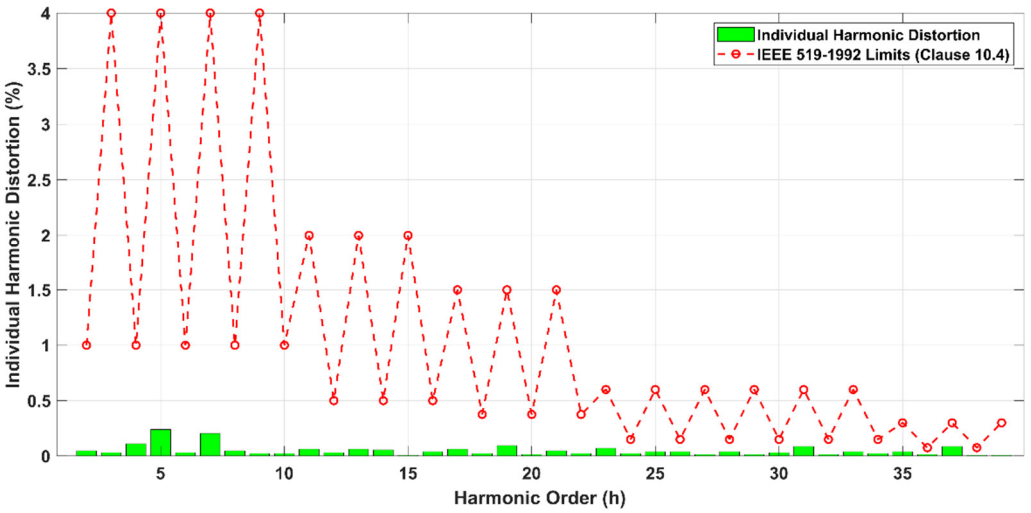

(a) at 700 W/m^2, T= 25°C

Figure 4.10 Individual harmonic distortion vs. IEEE 519-1992 limits.

In contrast, the TDD_{pcc} shows the opposite trend, decreasing from about 1.21% at STC to 1.16% under reduced irradiation. This behavior can be explained by the TDD formula:

$$TDD_{pcc} = \frac{I_1}{I_L} THD_{i,pcc} \tag{4.4}$$

Here, I_1 denotes the actual fundamental current, and I_L corresponds to the maximum demand current of the system. For the Oued El Kebrit PV system, this value is 15.87 A.

At STC, the PV system operates close to full load ($I_1 \approx I_L$), which makes the TDD_{pcc} value nearly equal to $THD_{i,pcc}$. When irradiation decreases, the fundamental current I1 becomes much smaller than the constant reference I_L, reflecting a lighter load condition. Although $THD_{i,pcc}$ (%) rises in this case—since the current waveform appears more distorted compared to its smaller fundamental—the numerator of the TDD_{pcc} formula ($I_1 \times THD_{i,pcc}$) decreases, causing the overall TDD_{pcc} to fall and remain below 5%. Furthermore, as shown in Fig. 4.10, the individual harmonic distortion values stayed within the limits set by Clause 10.4 of IEEE 519-1992.

This distinction explains why IEEE 519-1992 specifies harmonic limits using TDD instead of THD. Relying only on THD may overstate distortion during light-load conditions, whereas TDD offers a more stable measure of the harmonic contribution in relation to the system's rated demand. As a result, the use of TDD ensures that compliance reflects the actual influence of harmonics on the power grid rather than just the waveform's appearance at different operating conditions.

4.4 Performance benchmarking against previous works

The performance of the proposed 1 MW real PV plant model was benchmarked against other representative works in the literature, as summarized in Table 4.2. Several key insights emerge from this comparison: unlike earlier studies that relied on generic models with lower power levels and limited modeling detail, the present work employs a real utility-scale system with a high-fidelity approach, including iterative parameter identification, systematic inverter tuning, and dedicated filter design. As a result, it achieves superior MPPT efficiency, higher static and total conversion efficiencies, and significantly reduced harmonic distortion, all while fully complying with IEEE and EN grid code standards. This establishes the proposed model as both more realistic and more effective than prior benchmarks.

Ref.		**A. Refaat et al. [12] 2013**	**N. Motan et al. [13, 39] 2018**	**E. M. Khawla et al. [45] 2019**	**B. S. Mahdi et al. [46] 2022**	**M. Gupta et al. [48] 2025**	**This work**
Power Level		500 kW (Generic model)	6 kW (Generic model)	100 kW (Generic model)	250kW (Generic model)	5 kW (Generic model)	1 MW (Real PV plant model)
System Topology		3-phase/two-stage (boost converter + 2L-VSI)	3-phase/two-stage (boost converter + 2L-VSI)	3-phase/two-stage (boost converter + 2L-VSI)	3-phase/two-stage (boost converter + 3L-NPC)	3-phase/two-stage (boost converter + 2L-VSI)	3-phase/two-stage (boost converter + 2L-VSI)
Modeling Approach		Limited	Moderate	Limited	Limited	Limited	**High**
Identification of R_s/R_p of PV panel		----------	----------	----------	----------	----------	Iterative curve fitting technique
Boost converter design steps		No	**Yes**	No	No	No	**Yes**
MPPT Algorithm		INC	P&O	INC	P&O	INC	INC
Inverter Controller Tuning method		----------	----------	----------	----------	GWO	SO approach
PLL Tuning		----------	----------	----------	----------	----------	**Yes**
Filter design steps		No	**Yes**	No	No	No	**Yes**
Peak Efficiency (%)	Static MPPT efficiency $\eta_{mppt,static}$:	98.6%	----------	----------	----------	----------	**99.13%**
	Static conversion efficiency (inverter) η_{conv} :	----------	96%	----------	----------	----------	**97.23%**
	Total conversion efficiency η_{tot} :	----------	----------	----------	----------	----------	**96.38%**
Grid Code Compliance	IEEE 929-2000	**Yes**	**Yes**	Unity power factor criteria only (Clause 4.5)	Unity power factor criteria only (Clause 4.5)	Unity power factor criteria only (Clause 4.5)	**Yes**
	IEEE 519-1992	No	No	No	No	----------	**Yes**
	EN 50160	No	No	No	No	No	**Yes**

Where ---------- remain unclarified in the associated reference.

Table 4.2 Proposed model benchmarked against other published works.

4.5 Validation with real-time PV plant data

The accuracy of the proposed model was verified using real-time operational data collected on May 2, 2024, from the NC2000 monitoring and control system at the Oued El Kebrit PV plant (see Fig. 4.11). The dataset covered solar irradiance, temperature, and other parameters measured at TP01 (comprising two 500 kW central inverters) and at the PCC. For further details, refer to Appendix E.

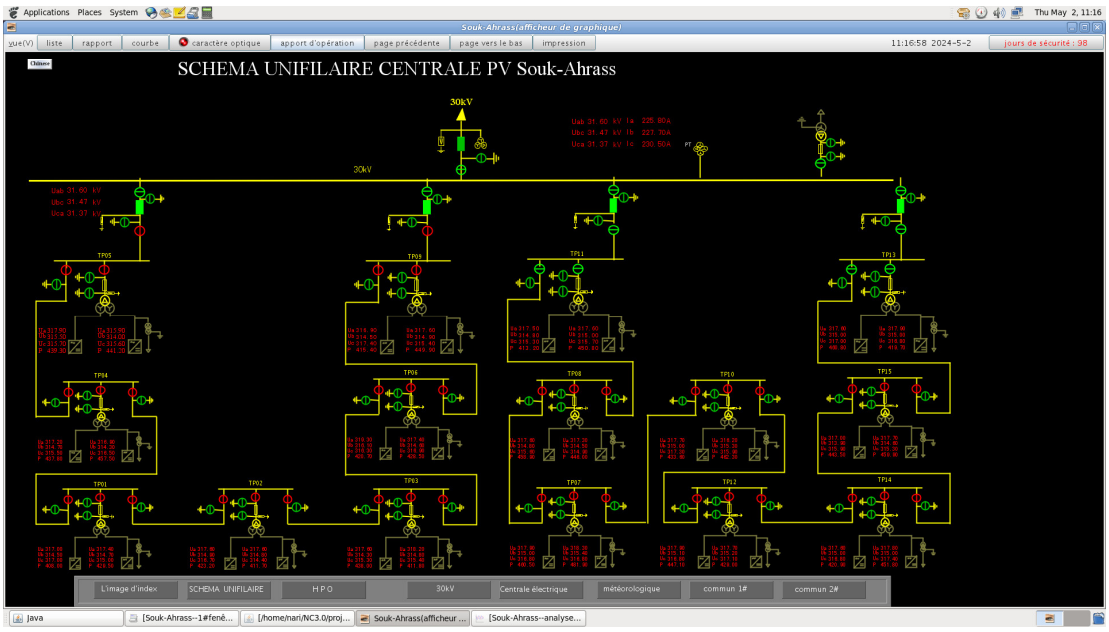

(a) single line diagram

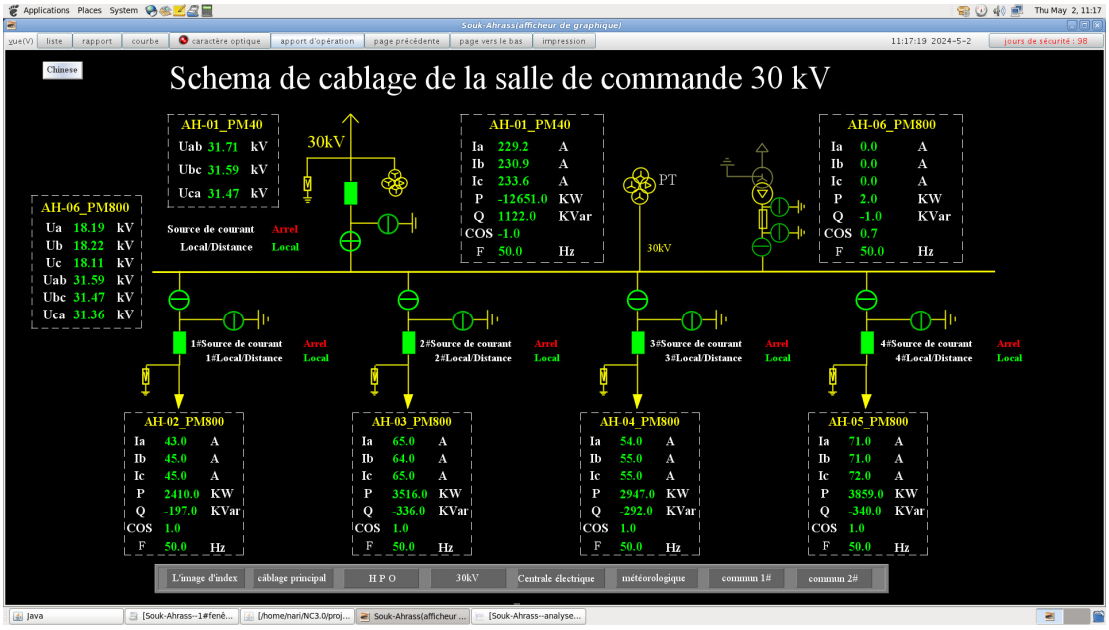

(b) wiring diagram

Figure 4.11 Interface of the NC2000 software utilized at the Souk Ahras photovoltaic plant.

	Real PV Plant Results	The Proposed Model Results
Meteorological Data	**G= 839.3 W/m^2, T_{cell}= 50°C**	
P_{pv} (kW)	710.65	751.59
$I_{a,\,PCC}$ (A)	12.43	13.48
$U_{ab,\,PCC}$ (kV)	31.50	31.17
$P_{inj,\,PCC}$ (kW)	681.51	729.14
Power Factor	1	1
f (Hz)	50.02	50.01
$THD_{v,PCC}$ (%)	1.40	0.20
$THD_{i,PCC}$ (%)	2.97	1.47
η_{tot} (%)	95.89	97.01

Table 4.3 Results of the proposed model vs. actual PV plant data at 10:00 AM,G=839.3 W/m^2, T_{cell}= 50 °C

Table 4.3 demonstrates that the model closely reproduced the real measurements at the PCC, particularly regarding injected active power, power factor, and grid frequency. Although the THD_v and THD_i values from the model were marginally below those observed in the actual plant, they remained well within the acceptable ranges defined by IEEE and EN standards.

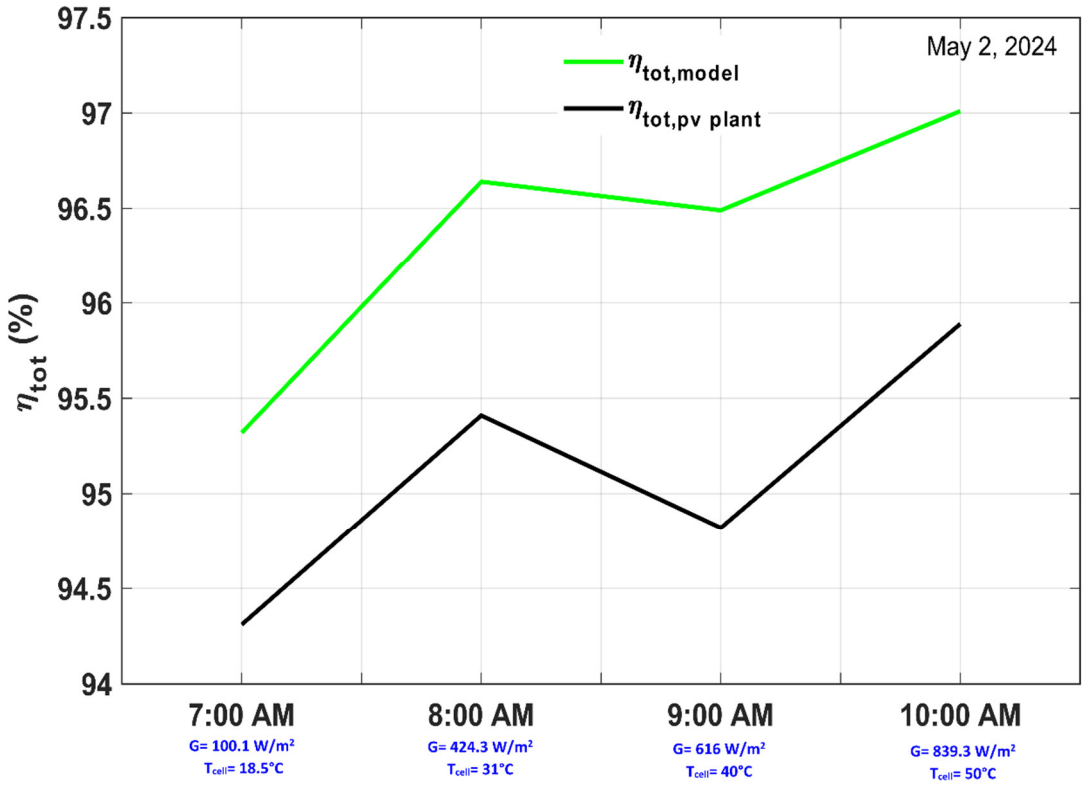

Figure 4.12 Comparison of overall conversion efficiency of the PV plant with that of the proposed model.

As shown in Fig. 4.12, the model reached a total conversion efficiency of 97.01% at 10 AM, closely corresponding to the 95.89% measured in the actual PV plant at that time. The minor difference between the two values is mainly due to extra system-level losses in the real plant, including cable, switchgear, and transformer copper losses, which the simulated model does not fully account for.

Nevertheless, the close match between simulated outputs and measured data verifies the robustness of the proposed model, showing that it can effectively capture both steady-state and dynamic behavior of the actual PV plant. Beyond proving compliance with IEEE 929–2000 and EN 50160 standards—supporting grid integration and power quality requirements—the model also offers a practical framework for control design, efficiency improvement, and predictive assessments under varying conditions. This dual role, as both a validated representation of the physical system and a practical research tool, highlights its value for further studies and real-world PV plant applications.

4.6 Conclusion

This chapter has presented a comprehensive performance evaluation of the proposed 1 MW grid-connected PV system, modeled using real data of the Oued El Kebrit PV plant. The results confirmed the system's ability to operate efficiently and reliably under both steady-state and transient conditions, meeting the technical requirements for grid interconnection as recommended by IEEE 929-2000, IEEE 519-1992, and EN 50160 standards.

Dynamic testing under sudden irradiance variations (from 1000 W/m² to 700 W/m²) revealed robust transient performance. Both the INC-based MPPT controller and VSI controller adapted quickly, restoring stable operation after a short transient. Furthermore, throughout the disturbance period, all power quality indicators remained within IEEE and EN limits. In terms of efficiency, the PV system model achieved a total conversion efficiency exceeding 96%, reflecting the effectiveness of the integrated power conditioning unit.

On the other hand, comparative analysis with the literature confirmed the advantages of the proposed model over more generic approaches, with superior efficiency, reduced harmonic distortion, and closer alignment with real-world operation. Validation against real PV plant data further strengthened these findings, confirming the model's accuracy, with simulated results closely matching actual measurements for active power injection, power factor, grid frequency,

and conversion efficiency (97.01% simulated vs. 95.89% measured), with only minor differences attributable to additional physical losses not captured in the simulation.

Finally, the results demonstrate that the developed 1 MW PV system model not only provides an accurate representation of the actual plant but also serves as a powerful design and analysis tool for future research in utility-scale PV systems.

General Conclusion and Perspective

General Conclusion and Perspective

Conclusion

The global transition towards renewable energy has become imperative, both to address growing electricity demands and to mitigate the environmental impacts of fossil fuels. In this context, this thesis has focused on the development of a detailed modeling and control strategy for a 1 MW grid-connected photovoltaic (PV) system, utilizing real operational data from the Oued El Kebrit (OKP) 15 MW_p PV plant in Souk Ahras, Algeria. By addressing identified research gaps, this work has made a meaningful contribution to advancing the design and implementation of large-scale PV systems, particularly in support of Algeria's ambitious renewable energy goals.

The primary objective was to create a high-fidelity model and control strategy for a grid-connected PV system that accurately reflects real-world conditions. To achieve this, Chapter II established a detailed DC-side model, employing the single-diode representation for the PV array with iteratively determined series and shunt resistances for the Yingli Solar YL250P-29b module. Furthermore, a comparative analysis of Hill Climbing and Incremental Conductance (INC) MPPT algorithms under dynamic conditions, such as irradiance variations, confirmed the INC method's superior performance for the OKP plant. In addition, a boost converter was designed to optimize energy transfer. Building upon this, Chapter III focused on the AC-side components. Specifically, it modeled a two-level voltage source inverter (2L-VSI) with sinusoidal pulse width modulation (SPWM), a passive-damped LCL filter for harmonic mitigation, and a synchronous reference frame phase-locked loop (SRF-PLL) for grid synchronization. The dual-loop control strategy, tuned using the symmetrical optimum method, ensured stable current injection and unity power factor operation. To replicate the OKP plant's actual operating conditions, transmission line parameters were analytically derived.

Subsequently, Chapter IV integrated these components into a comprehensive 1 MW system model, simulated in MATLAB/Simulink under both standard test conditions (STC) and dynamic scenarios, such as a sudden irradiance drop from 1000 W/m² to 700 W/m². The results demonstrated robust system performance, maintaining DC-link voltage stability, unity power factor, and compliance with IEEE 929-2000, IEEE 519-1992, and EN 50160 standards. Notably, the total conversion efficiency reached 96.38%, while harmonic distortion metrics (THD_i < 1.5%, TDD < 1.2%) remained well within the prescribed limits. Importantly, validation against real-time data from the OKP plant on May 2, 2024, confirmed the model's accuracy, with

simulated results closely matching measured active power, power factor, and efficiency (97.01% simulated vs. 95.89% actual).

Finally, benchmarking against prior studies highlighted the superiority of this work's approach. Unlike generic models with limited detail, this thesis incorporated real plant data, systematic controller tuning, and comprehensive grid code compliance. As a result, it represents the first validated large-scale PV system model in Algeria, thereby underscoring its value for both further academic studies and real-world PV plant applications.

Perspectives

While this thesis has made important contributions to the modeling and control of large-scale photovoltaic systems, several avenues remain open for future exploration:

- **Accounting for system-level losses:** future work could incorporate detailed models of auxiliary components such as cables, switchgear, and transformers to better capture copper and parasitic losses. This refinement would help reduce the small discrepancies observed between simulated and real system efficiencies.
- **Advanced MPPT and control strategies:** further research may investigate the use of artificial intelligence and optimization-based MPPT algorithms. These approaches could enhance tracking accuracy under partial shading or rapidly changing environmental conditions. In addition, future work could explore improvements in synchronization techniques and their associated controllers, thereby ensuring more robust and stable grid integration. Moreover, exploring alternative types of PLL designs could help enhance performance under distorted grid conditions and during transient faults.
- **Enhanced grid support functions:** expanding the model to include grid-support features such as fault ride-through capabilities or dynamic reactive power injection strategies tailored to high-penetration PV scenarios

References

References

[1] International Energy Agency (IEA) : Electricity Mid-Year Update [Report], July 2025.

[2] X. Lan, Tans, P. and K.W., Thoning: Trends in globally-averaged CO2 determined [Report], NOAA Global Monitoring Laboratory, 2025-09. doi: 10.15138/9N0H-ZH07.

[3] CRIPPA, M., GUIZZARDI, D., PAGANI, F., BANJA, M., MUNTEAN, M. et al., GHG emissions of all world countries - 2025 Report, Publications Office of the European Union, Luxembourg, 2025, https://data.europa.eu/doi/10.2760/9816914, JRC143227.

[4] H. Fathima, N. Prabaharan, P. Kaliannan, A. Kalam, S. Mekhilef, and J. J. Justo, Hybrid-Renewable Energy Systems in Microgrids: Integration, Developments and Control [Book]. 2018, pp. 1–253. doi: 10.1016/C2017-0-01772-X.

[5] Y. R. Li, F. Nejabatkhah, and H. Tian, Smart Hybrid AC/DC Microgrids: Power Management, Energy Management, and Power Quality Control [Book], 2022. doi: 10.1002/9781119598411.

[6] Y. Yang, K. A. Kim, F. Blaabjerg, and A. Sangwongwanich, Advances in grid-connected photovoltaic power conversion systems [Book], Woodhead Publishing, 2018.

[7] H. M. Shertukde, Distributed photovoltaic grid transformers. Crc Press, 2017.

[8] S. Bouacha, "A Study on Photovoltaic Power Plant Connected to the Distribution Network," Doctoral Thesis, Electronic Departement, National Polytechnic School, 2021.

[9] A. Chabani, S. Makhloufi, and S. Lachtar, "Overview and impact of the renewable energy plants connected to the electrical network in southwest Algeria," EAI Endorsed Transactions on the Energy Web, vol. 8, no. 36, 2021.

[10] K. Bouchouicha, N. Bailek, A. Razagui, M. EL-Shimy, M. Bellaoui, and N. E. I. Bachari, "Comparison of artificial intelligence and empirical models for energy production estimation of 20 MWp solar photovoltaic plant at the Saharan Medium of Algeria," International Journal of Energy Sector Management, vol. 15, no. 1, pp. 119-138, 2021.

[11] S. Haddoum, H. Bennour, and T. A. Zaid, "Renewables in the Energy Mix of Algeria, a pledge for food security," ENP Engineering Science Journal, vol. 4, no. 1, pp. 50-54, 2024.

[12] A. Refaat, A. Kalas, A. Daoud, and F. Bendary, "A control methodology of three phase grid connected pv system," energy, vol. 1, no. 2, 2013.

[13] N. Motan, M. Abu-Khaizaran, and M. Quraan, "Photovoltaic array modelling and boost-converter controller-design for a 6kW grid-connected photovoltaic system-DC stage," in 2018 IEEE International Conference on Environment and Electrical Engineering and 2018 IEEE Industrial and Commercial Power Systems Europe (EEEIC/I&CPS Europe), 2018: IEEE, pp. 1-6.

[14] S. V. Rajani and V. J. Pandya, "Simulation and comparison of perturb and observe and incremental conductance MPPT algorithms for solar energy system connected to grid," Sadhana, vol. 40, no. 1, pp. 139-153, 2015.

[15] E. Institute, "Statistical Review of World Energy 2025," ed: Energy Institute London, UK, 2025.

[16] Y. M. R. Yaiche and A. Bouhanik, Gisement solaire: Energie produite pour des centrales de 1 MWc Environnement, Atlas GEE, Renewable Energy Development Center (CDER), 2023. ISSN: 1112-3850.

[17] H. Abu-Rub, M. Malinowski, and K. Al-Haddad, Power electronics for renewable energy systems, transportation and industrial applications [Book], John Wiley & Sons, 2014.

[18] "U.S. Energy Information Administration. International Energy Outlook 2023," October 2023.

[19] A. Belaid et al., “High-Resolution Mapping of Concentrated Solar Power Site Suitability in Ghardaïa, Algeria: A GIS-Based Fuzzy Logic and Multi-Criteria Decision Analysis,” IEEE Access, vol. 13, pp. 231–255, 2025. doi: 10.1109/ACCESS.2024.3522572.

[20] B. LAMRI, "Analyse énergétique et intégration de la sûreté de fonctionnement dans un système photovoltaïque connecté au réseau électrique," Thèses de doctorat, Université de Annaba-Badji Mokhtar, 2018.

[21] N. Mennai, A. Medoued, and Y. Soufi, "A detailed model and control strategy for a three-phase grid-connected PV system: a case study of Oued El Kebrit 15 MWp PV plant," Electrical Engineering, vol. 107, no. 3, pp. 3197-3216, 2025.
[22] D. Myers, Chapter 1.12: Solar Radiation Resource Assessment for Renewable Energy Conversion, in: A. Sayigh (Ed.), Comprehensive Renewable Energy, 2012, pp. 213–237. doi: 10.1016/B978-0-08-087872-0.00112-8
[23] M. Järvinen and H. Paulomäki, Designing Renewable Energy Systems within Planetary Boundaries: A Textbook for Energy Engineers. Springer Nature, 2025.
[24] J. S. Stein, "Energy Prediction and System Modeling," in Photovoltaic Solar Energy, 2016, pp. 564-578.
[25] Z. Sen, Solar energy fundamentals and modeling techniques: atmosphere, environment, climate change and renewable energy. Springer Science & Business Media, 2008.
[26] A. Labouret and M. Villoz, Energie solaire photovoltaïque [Livre]. Dunod Paris, 2006.
[27] K. Namrata, R. Saini, and D. P. Kothari, Wind and Solar Energy Systems. Springer Nature, 2024.
[28] A. Blakers and N. Zin, "Silicon Solar Cell Device Structures," in Photovoltaic Solar Energy, 2016, pp. 80-91.
[29] H.-L. Chen et al., "A 19.9%-efficient ultrathin solar cell based on a 205-nm-thick GaAs absorber and a silver nanostructured back mirror," Nature Energy, vol. 4, no. 9, pp. 761-767, 2019.
[30] A. Chellakhi and S. El Beid, Optimizing Solar Photovoltaic Systems: Advances in MPPT Techniques for Enhanced Energy Efficiency. Springer Nature, 2025.
[31] R. Mukund and B. PATEL, Wind and solar power systems: design, analysis, and operation [Book]. CRC press, 2021. doi: 10.1201/9781420039924
[32] A. Mellit and S. Kalogirou, Handbook of Artificial Intelligence Techniques in Photovoltaic Systems: Modeling, Control, Optimization, Forecasting and Fault Diagnosis. Academic Press, 2022.
[33] A. El Hammoumi, S. Chtita, S. Motahhir, and A. El Ghzizal, "Solar PV energy: From material to use, and the most commonly used techniques to maximize the power output of PV systems: A focus on solar trackers and floating solar panels," Energy Reports, vol. 8, pp. 11992-12010, 2022.
[34] D. Rekioua and E. Matagne, Optimization of photovoltaic power systems: modelization, simulation and control [Book], Springer Science & Business Media, 2012.
[35] N. Priyadarshi, P. Sanjeevikumar, F. Azam, C. Bharatiraja, and R. Singh, Advanced Power Electronics Converters for Future Renewable Energy Systems [Book], CRC Press, 2023. doi: 10.1201/9781003323471
[36] D. Kolantla, S. Mikkili, S. R. Pendem, and A. A. Desai, "Critical review on various inverter topologies for PV system architectures," IET Renewable Power Generation, vol. 14, no. 17, pp. 3418-3438, 2020.
[37] W. Yao, Y. Xiong, H. Zhou, and J. Wen, Large-Scale Grid-Connected Wind and Photovoltaic Farms: Modeling, Stability and Control [Book], 2025. doi: 10.1007/978-981-96-3781-2.
[38] A. Haque, M. A. Khan, and V. Kurukuru, Design and Control of Grid-Connected Photovoltaic System. CRC Press, 2023.
[39] N. Motan and M. Abu-Khaizaran, "Design and Modelling of a 6kW Grid-Connected Photovoltaic System-AC Stage," in 2018 IEEE International Conference on Environment and Electrical Engineering and 2018 IEEE Industrial and Commercial Power Systems Europe (EEEIC/I&CPS Europe), 2018: IEEE, pp. 1-7.
[40] A. Islam and M. I. B. Chowdhury, "A Simulink based generalized model of PV cell/array," in 2014 3rd International Conference on the Developments in Renewable Energy Technology (ICDRET), 2014: IEEE, pp. 1-5.
[41] M. G. Villalva, J. R. Gazoli, and E. Ruppert Filho, "Modeling and circuit-based simulation of photovoltaic arrays," in 2009 Brazilian power electronics conference, 2009: IEEE, pp. 1244-1254.
[42] L. Y. Keong and F. A. Jamaludin, "Design and study the PV cell characteristic and INC MPPT method under varying Irradiance and Temperature in MATLAB/Simulink," ed, 2019.
[43] S. A. Mohamed and M. Abd El Sattar, "A comparative study of P&O and INC maximum power point tracking techniques for grid-connected PV systems," SN Applied Sciences, vol. 1, no. 2, p. 174, 2019.

[44] A. A. Valedsaravi Seyedamin, Barrado, José Antonio, Hamzeh Mohsen, Martinez-Salamero, "Grid-connected LCL Filter Design with Different Damping Methods," presented at the The 28th edition of the Annual Seminar on Automation, Industrial Electronics and Instrumentation (SAAEI'21), Ciudad Real, University of Castilla-La Mancha, 2021.
[45] E. M. Khawla, D. E. Chariag, and L. Sbita, "A control strategy for a three-phase grid connected PV system under grid faults," Electronics, vol. 8, no. 8, p. 906, 2019.
[46] B. S. Mahdi, M. S. Ali, N. Sulaiman, H. Hizam, S. Shafie, and M. A. Shehab, "Comparative Study of DC/AC InverterControl Techniques for Three Phase Grid Connected PV System," TEM Journal, vol. 11, no. 3, 2022.
[47] M. P. Thakre, N. P. Matale, and P. S. Borse, "A Survey based on PLL and its Synchronization Techniques for Interconnected System," in 2021 International Conference on Artificial Intelligence and Smart Systems (ICAIS), 2021: IEEE, pp. 1011-1016.
[48] M. Gupta, P. Tiwari, R. Viral, A. Shrivastava, B. A. Zneid, and I. Hunko, "Grid-connected PV inverter system control optimization using Grey Wolf optimized PID controller," Scientific reports, vol. 15, no. 1, p. 28869, 2025.
[49] M. H. Mohamed Hariri, M. Salem, M. K. Mohd Jamil, M. N. Abdullah, and M. K. Mat Desa, "Modeling and analysis of 100 kW two-stage three-phase grid-connected PV generation system under absurd atmospheric and grid disturbances," PLoS One, vol. 20, no. 6, p. e0323269, 2025.
[50] European standard EN 50160, Cenelec, 2000. [Online]. Available: http://dfv-technologie.com/doc_technique_dfv/normes_afnor/EN50160.pdf
[51] M. H. Mohamed Hariri, M. K. Mat Desa, S. Masri, and M. A. A. Mohd Zainuri, "grid-connected PV generation system—Components and challenges: A review," Energies, vol. 13, no. 17, p. 4279, 2020.
[52] A. Lunardi, L. F. Normandia Lourenco, E. Munkhchuluun, L. Meegahapola, and A. J. Sguarezi Filho, "Grid-connected power converters: An overview of control strategies for renewable energy," Energies, vol. 15, no. 11, p. 4151, 2022.
[53] A. S. Al-Ezzi and M. N. M. Ansari, "Photovoltaic solar cells: a review," Applied System Innovation, vol. 5, no. 4, p. 67, 2022.
[54] M. S. Pattelath, S. M. Giripunje, and A. K. Verma, "A Review of Photovoltaic Cell Generations and Simplified Overview of Bifacial Photovoltaic Cell Technology," Applied Solar Energy, vol. 59, no. 5, pp. 621-646, 2023.
[55] C. Cabal, "Optimisation énergétique de l'étage d'adaptation électronique dédié à la conversion photovoltaïque," phd thesis, Université Paul Sabatier - Toulouse III, 2008. [Online]. Available: https://theses.hal.science/tel-00357487
[56] J. R. Balfour, M. Shaw, and N. B. Nash, Introduction to photovoltaic system design [Book], Jones & Bartlett Publishers, 2011.
[57] G. Stapleton and S. Neill, Grid-connected solar electric systems: the earthscan expert handbook for planning, design and installation [Book], Routledge, 2012.
[58] V. Tamrakar, S. Gupta, and Y. Sawle, "Study of characteristics of single and double diode electrical equivalent circuit models of solar PV module," in 2015 International Conference on Energy Systems and Applications, 2015: IEEE, pp. 312-317.
[59] S. A. Kalogirou, Solar energy engineering: processes and systems [Book], Elsevier, 2023.
[60] J. Cubas, S. Pindado, and M. Victoria, "On the analytical approach for modeling photovoltaic systems behavior," Journal of power sources, vol. 247, pp. 467-474, 2014.
[61] C. S. Solanki, Solar photovoltaics: fundamentals, technologies and applications [Book], Phi learning pvt. Ltd., 2015.
[62] S. K. Peddapelli and P. Virtic, Wind and Solar Energy Applications: Technological Challenges and Advances [Book], 2023.
[63] P. Malik and S. S. Chandel, A new integrated single-diode solar cell model for photovoltaic power prediction with experimental validation under real outdoor conditions, International Journal of Energy Research, vol. 45, no. 1, pp. 759-771, 2021.
[64] N. Mennai, A. Medoued, and Y. Soufi, "Comparative analysis of dynamic and steady State performances of Hill climbing and incremental conductance MPPT controllers for PV systems," Journal of Renewable Energy and Environment, vol. 11, no. 3, pp. 35-41, 2024.

[65] M. G. Villalva, J. R. Gazoli, and E. Ruppert Filho, "Comprehensive approach to modeling and simulation of photovoltaic arrays," IEEE Transactions on power electronics, vol. 24, no. 5, pp. 1198-1208, 2009.
[66] Yge 60 cell series datasheet. [Online]. Available: https://www.solaris-shop.com/content/YL250P-29b-H4-Blk%20Specs.pdf
[67] K. Kumar, P. Kumar, and A. K. Bohre, "Performance analysis of IC MPPT algorithm for applications of solar PV in DC microgrid," SN Computer Science, vol. 4, no. 5, p. 579, 2023.
[68] N. E. Zakzouk, A. K. Abdelsalam, A. A. Helal, and B. W. Williams, "PV single-phase grid-connected converter: DC-link voltage sensorless prospective," IEEE Journal of Emerging and Selected Topics in Power Electronics, vol. 5, no. 1, pp. 526-546, 2016.
[69] M. A. Memon, G. M. Bhutto, and E. A. Buriro, "Sizing of dc-link capacitor for a grid connected solar photovoltaic inverter," Indian J. Sci. Technol, vol. 13, no. 22, pp. 2272-2281, 2020.
[70] M. Srikanth and K. Yadlapati, "MPPT Techniques Exploration under Uniform and Non-Uniform Solar Irradiance Condition–A Survey," in E3S Web of Conferences, 2024, vol. 472: EDP Sciences, p. 01024.
[71] Ö. F. Tozlu and H. Çalık, "A review and classification of most used MPPT algorithms for photovoltaic systems," Hittite Journal of Science and Engineering, vol. 8, no. 3, pp. 207-220, 2021.
[72] Y.-P. Huang, "A rapid maximum power measurement system for high-concentration photovoltaic modules using the fractional open-circuit voltage technique and controllable electronic load," IEEE journal of Photovoltaics, vol. 4, no. 6, pp. 1610-1617, 2014.
[73] M. S. Bhaskar, N. Gupta, S. Padmanaban, J. B. Holm-Nielsen, and U. Subramaniam, Power electronics for green energy conversion [Book], John Wiley & Sons, 2022.
[74] A. Aurairat and B. Plangklang, "An alternative perturbation and observation modifier maximum power point tracking of PV systems," Symmetry, vol. 14, no. 1, p. 44, 2021.
[75] H. Z. Al Garni, A. Sundaram, A. Awasthi, R. Chandel, S. Tajjour, and S. S. Chandel, "A comprehensive review of most competitive maximum power point tracking techniques for enhanced solar photovoltaic power generation," Journal of Renewable Energy and Environment, vol. 11, no. 3, pp. 60-80, 2024.
[76] K. Lappalainen and J. Kleissl, "Analysis of the cloud enhancement phenomenon and its effects on photovoltaic generators based on cloud speed sensor measurements," Journal of Renewable and Sustainable Energy, vol. 12, no. 4, 2020.
[77] M. Ahmed, M. Abdelrahem, A. Farhan, I. Harbi, and R. Kennel, "DC-link sensorless control strategy for grid-connected PV systems," Electrical Engineering, vol. 103, no. 5, pp. 2345-2355, 2021.
[78] M. Liserre*, F. Blaabjerg, and A. Dell'Aquila, "Step-by-step design procedure for a grid-connected three-phase PWM voltage source converter," International journal of electronics, vol. 91, no. 8, pp. 445-460, 2004.
[79] T. R. Nath, "Solar Photovoltaic Power Generating System & Grid Integration-Modeling, Controller Design and Optimization," phd thesis, Kyushu Institute of Technology, 2017. [Online]. Available: http://hdl.handle.net/10228/00006329
[80] G. D. Price, Power Systems and Renewable Energy: Design, Operation, and Systems Analysis [Book], Momentum Press, 2014.
[81] Muhammad H. Rashid, Power Electronics: Devices, Circuits, and Applications [Book], Fourth Edition. Pearson Education, 2014, p. 1027.
[82] M. Jamil, M. Rizwan, and D. P. Kothari, Grid integration of solar photovoltaic systems [Book], Crc Press, 2017.
[83] Z. J. Čorba, V. A. Katić, B. P. Dumnić, and D. M. Milićević, "In-grid solar-to-electrical energy conversion system modeling and testing," Thermal Science, vol. 16, no. suppl. 1, pp. 159-171, 2012.
[84] E. Kabalci, Y. Kabalci, and J. M. Guerrero, "Design and implementation of a dual-input single-output photovoltaic converter," Energies, vol. 13, no. 14, p. 3679, 2020.
[85] W. Xiao, Photovoltaic power system: modeling, design, and control [Book], John Wiley & Sons, 2017.

[86] K. Zeb et al., "An overview of transformerless inverters for grid connected photovoltaic system," in 2018 International Conference on Computing, Electronic and Electrical Engineering (ICE Cube), 2018: IEEE, pp. 1-6.
[87] Y. Yang, F. Blaabjerg, H. Wang, and M. G. Simões, "Power control flexibilities for grid-connected multi-functional photovoltaic inverters," IET Renewable Power Generation, vol. 10, no. 4, pp. 504-513, 2016.
[88] M. A. Hasan, N. K. Vemula, R. Devarapalli, and Ł. Knypiński, "Investigation into PV Inverter Topologies from the Standards Compliance Viewpoint," Energies, vol. 17, no. 16, p. 3879, 2024.
[89] A. I. Maswood and H. D. Tafti, "Advanced multilevel converters and applications in grid integration," 2018.
[90] M. Fakharmanesh, C. M. Hackl, and R. Perini, "Instantaneous conduction and switching losses in two-level voltage source inverters," in 2017 IEEE International Conference on Environment and Electrical Engineering and 2017 IEEE Industrial and Commercial Power Systems Europe (EEEIC/I&CPS Europe), 2017: IEEE, pp. 1-6.
[91] T. Bhattacharjee, M. Jamil, and A. Jana, "Design of SPWM based three phase inverter model," in 2018 Technologies for Smart-City Energy Security and Power (ICSESP), 2018: IEEE, pp. 1-6.
[92] N. Ismail, A. Permadi, A. Risdiyanto, B. Susanto, and M. A. Ramdhani, "The effect of amplitude modulation index and frequency modulation index on total harmonic distortion in 1-phase inverter," in IOP Conference Series: Materials Science and Engineering, 2018, vol. 288, no. 1: IOP Publishing, p. 012107.
[93] B. Alamri and Y. M. Alharbi, "A framework for optimum determination of LCL-filter parameters for N-level voltage source inverters using heuristic approach," IEEE Access, vol. 8, pp. 209212-209223, 2020.
[94] U. P. Yagnik and M. D. Solanki, "Comparison of L, LC & LCL filter for grid connected converter," in 2017 International Conference on Trends in Electronics and Informatics (ICEI), 2017: IEEE, pp. 455-458.
[95] I. Villanueva, N. Vázquez, J. Vaquero, C. Hernández, H. López, and R. Osorio, "L vs. LCL Filter for Photovoltaic Grid-Connected Inverter: A Reliability Study," International Journal of Photoenergy, vol. 2020, no. 1, p. 7872916, 2020.
[96] N. Arab, Study of the impact of power converters equipped with LC-LCL filters interfacing renewable energy sources to the grid, Thèse de doctorat électronique, Montréal, École de technologie supérieure, 2021.
[97] Y. Han, Modeling and Control of Power Electronic Converters for Microgrid Applications [Book], Springer Nature, 2021.
[98] Y. Han et al., "Modeling and stability analysis of $ LCL $-type grid-connected inverters: A comprehensive overview," IEEE Access, vol. 7, pp. 114975-115001, 2019.
[99] S. Baid, A. Priyadarshi, and R. Saha, "A Methodological Approach of LCL filter design for Industrial Application using MATLAB script," in 2023 IEEE 3rd International Conference on Smart Technologies for Power, Energy and Control (STPEC), 2023: IEEE, pp. 1-5.
[100] X. Ruan, X. Wang, D. Pan, D. Yang, W. Li, and C. Bao, Control techniques for LCL-type grid-connected inverters. Springer, 2018.
[101] M. Dursun and M. K. DÖŞOĞLU, "LCL filter design for grid connected three-phase inverter," in 2018 2nd International Symposium on Multidisciplinary Studies and Innovative Technologies (ISMSIT), 2018: IEEE, pp. 1-4.
[102] IEEE recommended practice for utility interface of photovoltaic (PV) systems, IEEE Std, vol. 929, 2000.
[103] IEEE Recommended Practices and Requirements for Harmonic Control in Electrical Power Systems, IEEE Std 519-1992 pp. 1-112, 1993. doi: 10.1109/IEEESTD.1993.114370.
[104] N. Mennai, Y. Soufi, A. Medoued, and A. Faleh, "Grid synchronization techniques analysis of dg systems under grid fault conditions," in 2022 19th International Multi-Conference on Systems, Signals & Devices (SSD), 2022: IEEE, pp. 917-922.
[105] K. Fuad, "Grid-voltage Synchronization Algorithms Based on Phase-locked Loop and Frequency-locked Loop for Power Converters," 2014.

[106] N. Mennai, "Intelligent Control for Enhanced Phase-Locked Loop Performance in Grid-Connected Inverters," in 6th International Hybrid Conference On Informatics And Applied Mathematics, December 6-7, 2023 Guelma, Algeria, 2024.
[107] S. M. Tripathi, A. N. Tiwari, and D. Singh, "Optimum design of proportional-integral controllers in grid-integrated PMSG-based wind energy conversion system," International Transactions on Electrical Energy Systems, vol. 26, no. 5, pp. 1006-1031, 2016.
[108] A. Sayigh, Renewable energy in the service of mankind Vol I: Selected topics from the world renewable energy congress WREC 2014. springer, 2015.
[109] E. Kantar, "Design and control of PWM converter with LCL type filter for grid interface of renewable energy systems," phd thesis, 2014. doi: 10.13140/RG.2.2.29200.92165.
[110] T. D. Gupta, D. Kumar, and K. Chaudhary, "Modelling and analysis of grid-tied fuel cell system with synchronous reference frame control," in 2017 4th International Conference on Power, Control & Embedded Systems (ICPCES), 2017: IEEE, pp. 1-6.
[111] G. Elhassan, S. A. Zulkifli, E. Pathan, M. H. Khan, and R. Jackson, "A comprehensive review on time-delay compensation techniques for grid-connected inverters," IET Renewable Power Generation, vol. 15, no. 2, pp. 251-266, 2021.
[112] Q. Xiao, F. Tang, Z. Xin, J. Zhou, P. Chen, and P. C. Loh, "Large time-delay decoupling and correction in synchronous complex-vector frame," IET Power Electronics, vol. 12, no. 2, pp. 254-266, 2019.
[113] J. Shi, W. Huang, and X. Zheng, "Complete decoupling compensation of three-phase inverter with LCL filter in synchronous reference frame," IET Power Electronics, vol. 15, no. 5, pp. 381-394, 2022.
[114] H. Alrajhi, Y. Al-Harbi, A. Al-Zahrani, S. A. Raza, A. Daraz, and M. Al-Kaabi, "Comprehensive analysis of PI tuning techniques for VSC applications," Journal of Umm Al-Qura University for Engineering and Architecture, pp. 1-18, 2025.
[115] J. D. Glover, M. S. Sarma, T. J. Overbye, and N. Padhy, Power system analysis and design [Book]. Cengage Learning Stamford, CT, USA, 2012.

Appendices

Appendices

Appendix A

- **Datasheet of Yingli Solar YL250P-29b module**

YGE 60 CELL SERIES

ELECTRICAL PERFORMANCE

Electrical parameters at standard Test conditions (STC)

module type			yl 260P-29b	yl 255P-29b	yl 250P-29b	yl 245P-29b	yl 240P-29b
Power output	P_{max}	W	260	255	250	245	240
Power output tolerances	ΔP_{max}	%			-0 / +3		
Module eff ciency	η_m	%	15.9	15.6	15.3	15.0	14.7
Voltage at P_{max}	V_{mpp}	V	30.3	30.0	29.8	29.6	29.3
current at P_{max}	I_{mpp}	a	8.59	8.49	8.39	8.28	8.18
open-circuit voltage	V_{oc}	V	37.7	37.7	37.6	37.5	37.5
short-circuit current	I_{sc}	a	9.09	9.01	8.92	8.83	8.75

STC: 1000W/m² irradiance, 25°C cell temperature, AM 1.5g spectrum according to EN 60904-3
Average relative eff ciency reduction of 3.3% at 200W/m² according to EN 60904-1

Electrical parameters at nominal operating cell Temperature (NOCT)

Power output	P_{max}	W	189.7	186.0	182.4	178.7	175.1
Voltage at P_{max}	V_{mpp}	V	27.6	27.4	27.2	27.0	26.8
current at P_{max}	I_{mpp}	a	6.87	6.79	6.71	6.62	6.54
open-circuit voltage	V_{oc}	V	34.8	34.8	34.7	34.6	34.6
short-circuit current	I_{sc}	a	7.35	7.28	7.21	7.14	7.07

NOCT: open-circuit operating cell temperature at 800W/m² irradiance, 20°C ambient temperature, 1m/s wind speed

THERMAL CHARACTERISTICS

nominal operating cell temperature	NOCT	°C	46 +/- 2
Temperature coeff cient of P_{max}	γ	%/°C	-0.42
Temperature coeff cient of V_{oc}	β_{Voc}	%/°C	-0.32
Temperature coeff cient of I_{sc}	α_{Isc}	%/°C	0.05
Temperature coeff cient of V_{mpp}	β_{Vmpp}	%/°C	-0.42

Simulink model of the PV array: The PV array Simulink model consists of three (03) sections:

- **Model of the saturation current I_0**

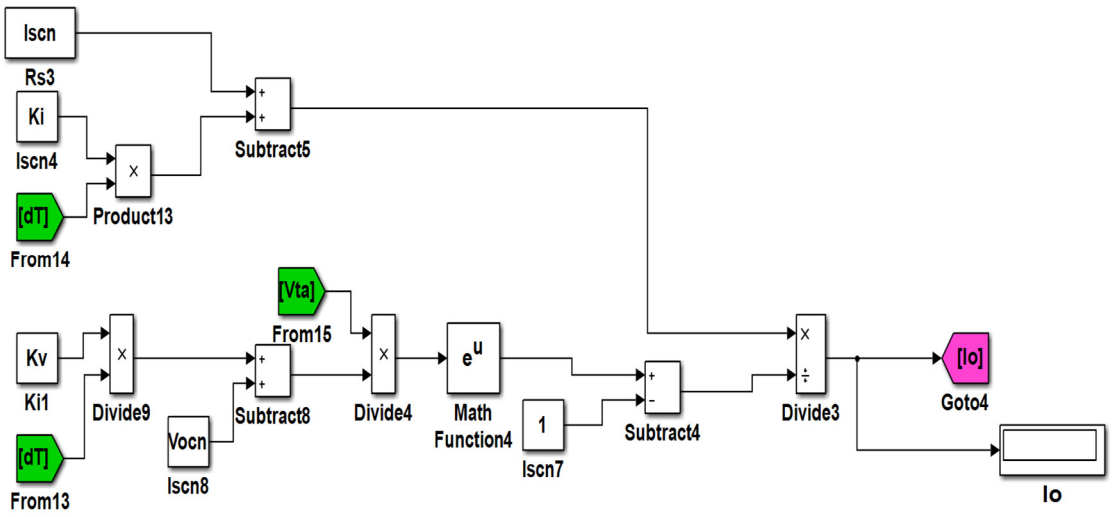

➢ **Model of the light-generated current I_{PV}**

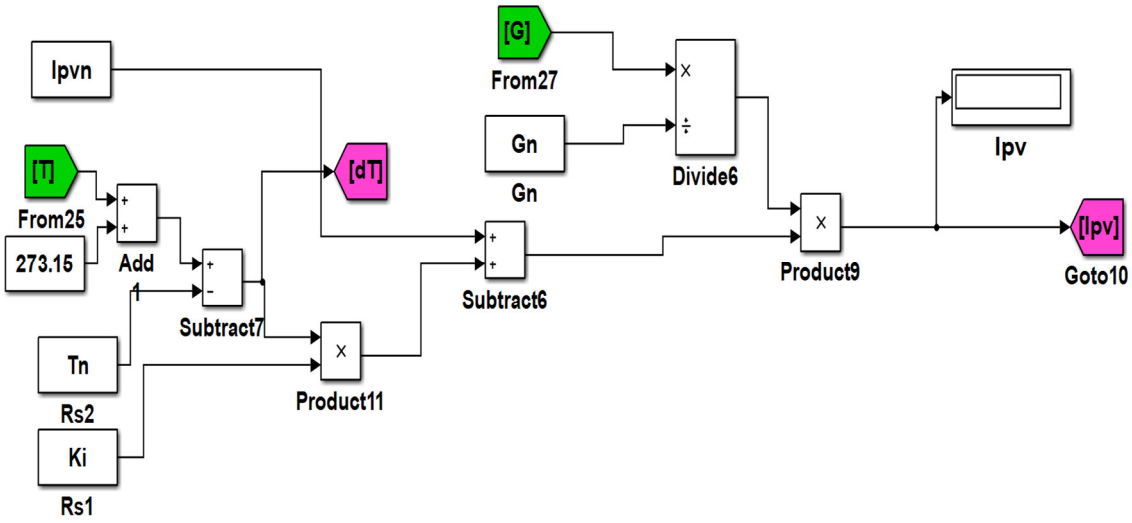

➢ **Model of the input supply current I_m**

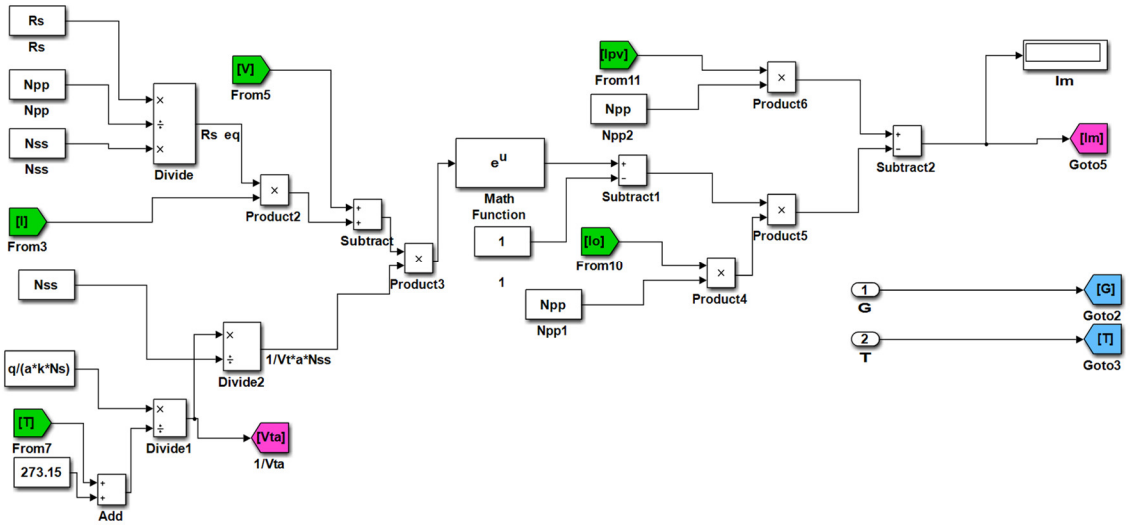

➢ **The one-diode model of PV array**

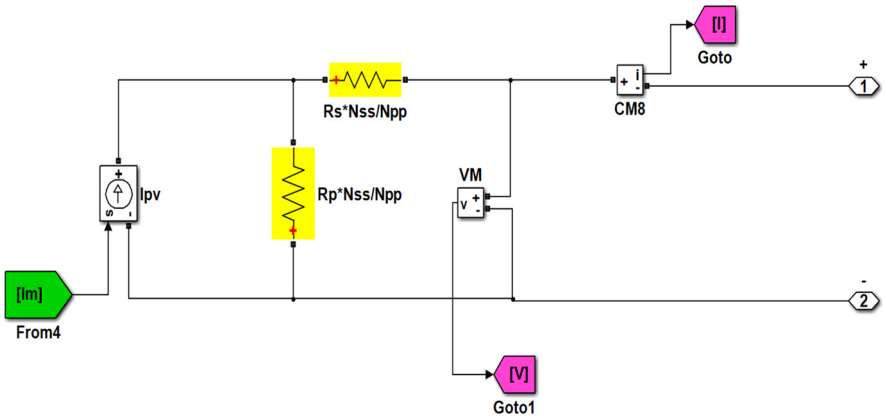

Appendix B

- **Simulink model of the Hill Climbing (HC) MPPT algorithm**

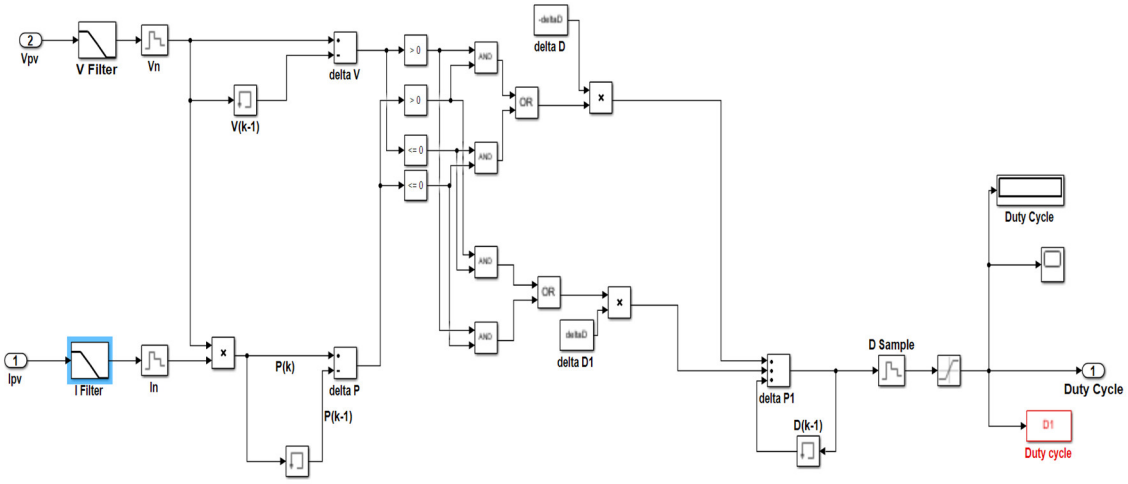

- **Simulink model of the Incremental Conductance (INC) MPPT algorithm**

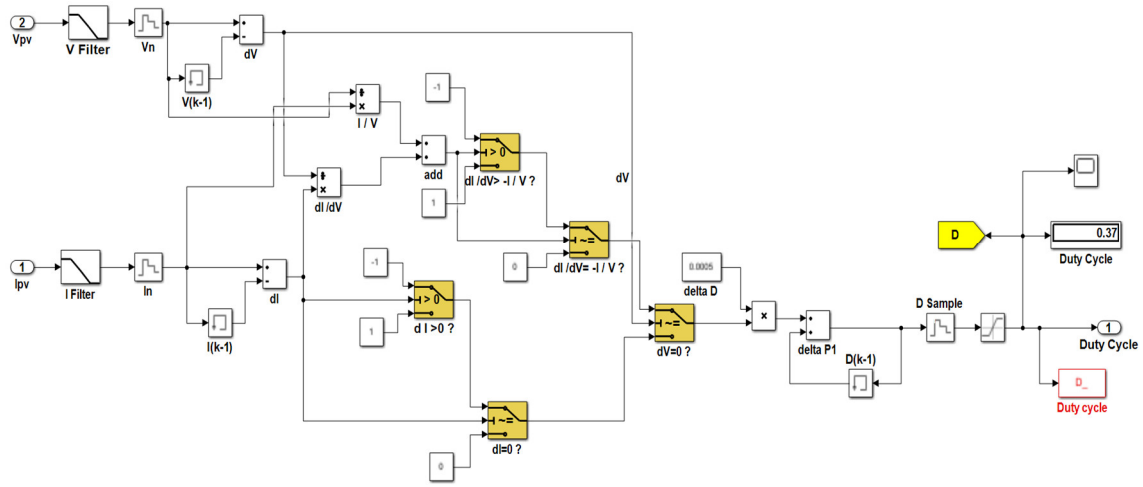

- **Simulink model of the Pulse width modulation (PWM)**

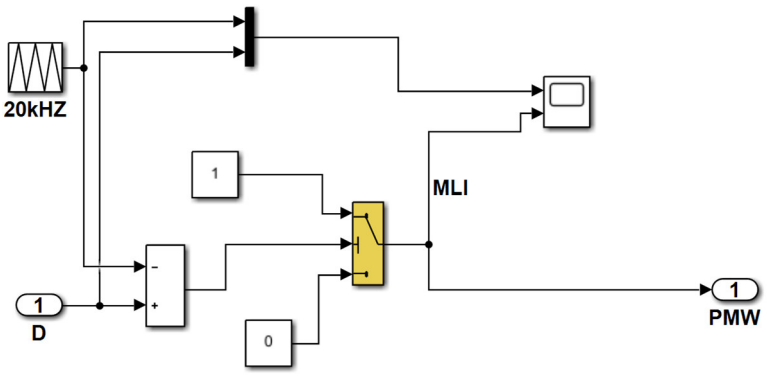

Appendix C

- **Datasheet of the 1 MW central inverter TBEA TC1000KS**

TECHNICAL SPECIFICATIONS – OUTDOOR SOLUTION – (IP-54)

	TC1000KS	TC1250KS
Input (DC)		
Max. DC Input Power	1236KW*	1417 KW
Max. DC Input Voltage	1000 V	
MPPT Voltage Range	500 – 820 V	520 – 820 V
Max. DC Current	2472 A	2725A
Number of DC Inputs	14 – 20	20
Max. PV Current per Input	200 A	
Earthing Fault Detection	Yes	
DCOvervoltageSurgeProtection	Yes	
External Power Supply	380 V /3P4L	
Output (AC)		
RatedAC Output Power	1000 kW	1250 kW
Number of AC Outputs	2	
RatedAC Voltage	315V	340V
Rated Output Current per AC output	916 A	1061 A
Max. AC Output Current	1099 A	1167 A
Grid Frequency Range	49.5 – 50.2 Hz	
Total Harmonic Distortion of Grid Current THDi	<3%	
Power Factor	0.9 lead - 0.9lag, adjustable	
ACOvervoltageSurgeProtection	Yes	
Efficiency		
Max. Efficiency	98.7 %	
European Efficiency	98.4 %	
Mechanical Data		
Dimension (W/H/D)	2438 × 2591 × 2991mm	
Weight	7t	
General Data		
Ambient Temperature Range	-30 to +60 °C (above 55°C, derating)	
Ambient Humidity Range	0 to 95 % (non condensing)	
Max. Operating Altitude	3,000 m (above 3000m, derating)	
Cooling Method	Forced air cooling , speed adjustable	
Protection Degree	IP54	
Data Collection and Communication		
RS485	Yes	
Fiber-optical communication interface	Yes	
Protocol Converter	Yes	

TC1000KS
&
TC1250KS

TBEA 特变电工

Appendix D

- **Step-up transformer used in OKP plant : SUNTEN 0.315/31.5 kV**

Appendix E

- **Real-time operational data collected on May 2, 2024, from the OKP PV plant at 7:00 AM, 8:00 AM, 9:00 AM, and 10:00 AM.**

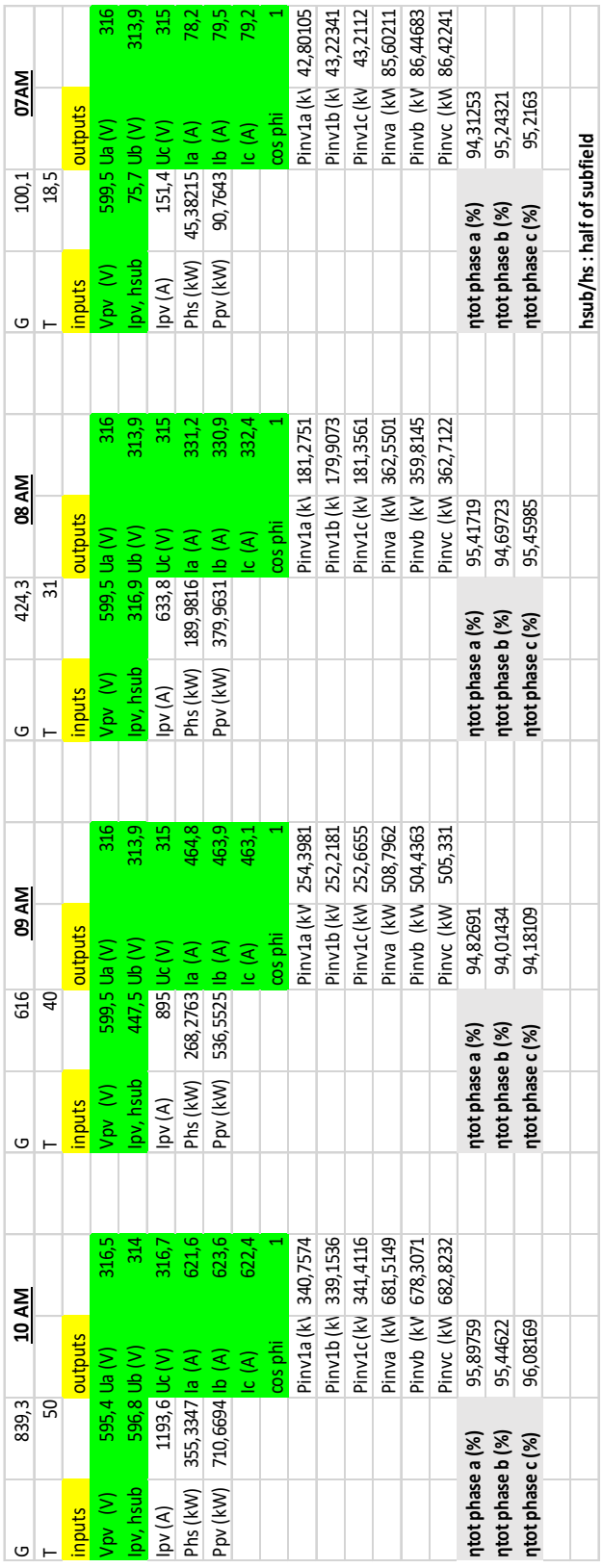

G	839,3	10 AM		G	616	09 AM		G	424,3	08 AM		G	100,1	07AM	
T	50			T	40			T	31			T	18,5		
inputs		outputs		inputs		outputs		inputs		outputs		inputs		outputs	
Vpv (V)	595,4	Ua (V)	316,5	Vpv (V)	599,5	Ua (V)	316	Vpv (V)	599,5	Ua (V)	316	Vpv (V)	599,5	Ua (V)	316
Ipv, hsub	596,8	Ub (V)	314	Ipv, hsub	447,5	Ub (V)	313,9	Ipv, hsub	316,9	Ub (V)	313,9	Ipv, hsub	75,7	Ub (V)	313,9
Ipv (A)	1193,6	Uc (V)	316,7	Ipv (A)	895	Uc (V)	315	Ipv (A)	633,8	Uc (V)	315	Ipv (A)	151,4	Uc (V)	315
Phs (kW)	355,3347	Ia (A)	621,6	Phs (kW)	268,2763	Ia (A)	464,8	Phs (kW)	189,9816	Ia (A)	331,2	Phs (kW)	45,38215	Ia (A)	78,2
Ppv (kW)	710,6694	Ib (A)	623,6	Ppv (kW)	536,5525	Ib (A)	463,9	Ppv (kW)	379,9631	Ib (A)	330,9	Ppv (kW)	90,7643	Ib (A)	79,5
		Ic (A)	622,4			Ic (A)	463,1			Ic (A)	332,4			Ic (A)	79,2
		cos phi	1			cos phi	1			cos phi	1			cos phi	1
		Pinv1a (kV	340,7574			Pinv1a (kV	254,3981			Pinv1a (kV	181,2751			Pinv1a (kV	42,80105
		Pinv1b (kV	339,1536			Pinv1b (kV	252,2181			Pinv1b (kV	179,9073			Pinv1b (kV	43,22341
		Pinv1c (kV	341,4116			Pinv1c (kW	252,6655			Pinv1c (kV	181,3561			Pinv1c (kV	43,2112
		Pinva (kW	681,5149			Pinva (kW	508,7962			Pinva (kW	362,5501			Pinva (kW	85,60211
		Pinvb (kV	678,3071			Pinvb (kW	504,4363			Pinvb (kV	359,8145			Pinvb (kV	86,44683
		Pinvc (kW	682,8232			Pinvc (kW	505,331			Pinvc (kW	362,7122			Pinvc (kW	86,42241
ηtot phase a (%)		95,89759		**ηtot phase a (%)**		94,82691		**ηtot phase a (%)**		95,41719		**ηtot phase a (%)**		94,31253	
ηtot phase b (%)		95,44622		**ηtot phase b (%)**		94,01434		**ηtot phase b (%)**		94,69723		**ηtot phase b (%)**		95,24321	
ηtot phase c (%)		96,08169		**ηtot phase c (%)**		94,18109		**ηtot phase c (%)**		95,45985		**ηtot phase c (%)**		95,2163	
												hsub/hs : half of subfield			

- **Real-time operational data collected on May 2, 2024 at 10 AM using the NC2000 monitoring and control system software**